

SPECTROSCOPIC CHARACTERIZATION OF SEMICONDUCTOR  
NANOCRYSTALS

A THESIS SUBMITTED TO  
THE GRADUATE SCHOOL OF NATURAL AND APPLIED SCIENCES  
OF  
MIDDLE EAST TECHNICAL UNIVERSITY

BY

SELÇUK YERÇİ

IN PARTIAL FULFILLMENT OF THE REQUIREMENTS  
FOR  
THE DEGREE OF MASTER OF SCIENCE  
IN  
PHYSICS

JANUARY 2007

Approval of the Graduate School of Natural and Applied Sciences

---

Prof. Dr. Canan Özgen  
Director

I certify that this thesis satisfies all the requirements as a thesis for the degree of Master of Science.

---

Prof. Dr. Sinan Bilikmen  
Head of Department

This is to certify that we have read this thesis and that in our opinion it is fully adequate, in scope and quality, as a thesis for the degree of Master of Science.

---

Prof. Dr. Raşit Turan  
Supervisor

**Examining Committee Members**

Prof. Dr. Atilla Aydınli (Bilkent University, PHYS)\_\_\_\_\_

Prof. Dr. Raşit TURAN (METU, PHYS)\_\_\_\_\_

Prof. Dr. Çiğdem Erçelebi (METU, PHYS)\_\_\_\_\_

Prof. Dr. Macit Özenbaş (METU, METE)\_\_\_\_\_

Prof. Dr. Nizami Gasanly (METU, PHYS)\_\_\_\_\_

**I hereby declare that all information in this document has been obtained and presented in accordance with academic rules and ethical conduct. I also declare that, as required by these rules and conduct, I have fully cited and referenced all material and results that are not original to this work.**

Name, Last name : Selçuk Yerci

Signature :

## **ABSTRACT**

### **CHARACTERIZATION OF SEMICONDUCTOR NANOCRYSTALS USING SPECTROSCOPIC TECHNIQUES**

Yerci, Selçuk

M. Sc., Department of Physics

Supervisor: Prof. Dr. Raşit Turan

January 2007, 98 pages

Semiconductor nanocrystals are expected to play an important role in the development of new generation of microelectronic and photonic devices such as light emitting diodes and memory elements. Optimization of these devices requires detailed investigations. Various spectroscopic techniques have been developed for material and devices characterization. This study covers the applications of the following techniques for the analysis of nanocrystalline materials: Fourier Transform Infrared Spectroscopy (FTIR), Raman Spectroscopy, X-Ray Diffraction (XRD) and X-Ray Photoelectron (XPS). Transmission Electron Microscopy (TEM) and Secondary Ion Mass Spectrometry (SIMS) are also used as complementary methods. Crystallinity ratio, size, physical and chemical environment of the nanostructures were probed with these methods. Si and Ge nanocrystals were formed into the oxides  $\text{Al}_2\text{O}_3$  and  $\text{SiO}_2$  by ion implantation, magnetron sputtering and laser ablation methods. FTIR and XPS are two methods used to extract information on the surface of the nanocrystals. Raman and XRD are non destructive

and easy-to-operate methods used widely to estimate the crystallinity to amorphous ratio and the sizes of the nanocrystals.

In this study, the structural variations of SiO<sub>2</sub> matrix during the formation of Si nanocrystals were characterized by FTIR. The shift in position and changes in intensity of the Si-O-Si asymmetric stretching band of SiO<sub>x</sub> was monitored. An indirect metrology method based on FTIR was developed to show the nanocrystal formation. Ge nanocrystals formed in SiO<sub>2</sub> matrix were investigated using FTIR, Raman and XRD methods. FTIR spectroscopy showed that Ge atoms segregate completely from the matrix at relatively low temperatures 900 °C. The stress between the Ge nanocrystals and the matrix can vary in samples produced by magnetron sputtering if the production conditions are slightly different. Si and Ge nanocrystals were formed into Al<sub>2</sub>O<sub>3</sub> matrix by ion implantation of Si and Ge ions into sapphire matrix. Raman, XRD, XPS and TEM methods were employed to characterize the formed nanocrystals. XRD is used to estimate the nanocrystal sizes which are in agreement with TEM observations. The stress on nanocrystals was observed by Raman and XRD methods, and a quantitative calculation was employed to the Si nanocrystals using the Raman results. XPS and SIMS depth profiles of the sample implanted with Si, and annealed at 1000 °C were measured. Precipitation of Si atoms with the heat treatment to form the nanocrystals was observed using XPS. The volume fraction of the SiO<sub>x</sub> shell to the Si core in Si nanocrystals was found to be 7.9 % at projection range of implantation.

Keywords : XRD, Raman, XPS, FTIR, spectroscopy, nanocrystals, semiconductor.

## ÖZ

### YARIİLETKEN NANOKRİSTALLERİN SPEKTROSKOPİK YÖNTEMLERLE KARAKTERİZASYONU

Yerci, Selçuk

Yüksek Lisans, Fizik Bölümü

Tez Yöneticisi: Prof. Dr. Raşit Turan

Ocak 2007, 98 sayfa

Nanokristal tabanlı ışık yayan diyot ve bellek elemanlarının yeni nesil entegre devrelerinde önemli bir yer tutması beklenmektedir. Bu aygıtların kullanıma uygun hale getirilebilmesi için aygıtların yapıldığı malzemelerin detaylı bir şekilde incelenmesi gerekmektedir. Bu amaçla, çeşitli spektroskopik (tayfsal) teknik geliştirilmiştir. Bu çalışmada, nanokristal tabanlı malzemeler dört farklı analitik yöntem ile çalışılmıştır. Bu yöntemler Fourier Dönüşümlü Kızılötesi (FTIR), Raman Spektroskopisi, X-Işın Kırınımı (XRD) ve X-Işın Fotoelektron Spektroskopisidir (XPS). Geçişli Elektron Mikroskopisi (TEM) ve İkincil İyon Kütle Spektrometriside (SIMS) tamamlayıcı yöntemler olarak kullanılmıştır. Bu yöntemler, nanoyapıların kristallenme yüzdeleri, büyüklükleri, fiziksel ve kimyasal çevrelerini çözümlenmek (analiz) için kullanılmıştır. Si ve Ge nanokristaller  $Al_2O_3$  ve  $SiO_2$  oksitleri içerisinde iyon ekme, manyetron saçırma ve laser ablation yöntemleriyle oluşturulmuştur. FTIR ve XPS, nanokristallerin yüzeyleri hakkında bilgi edinmek için kullanılmıştır. Raman ve XRD (örneklere zarar vermeyen) hasarsız ve işletimi kolay yöntemler

olup, nanokristallerin kristallenme yüzdelерinin ve büyüklüklerinin tahmininde sıkça kullanılır.

Bu çalışmada, nanokristallerin oluşumu sırasında SiO<sub>2</sub> matrisindeki meydana gelen değişimler, FTIR spektroskopisi kullanılarak incelenmiştir. SiO<sub>x</sub> matrisine ait Si-O-Si antisimetrik gerilme bandındaki kaymalar ve bandın şiddetindeki değişimler gözlemlenmiştir. Nanokristal oluşunu anlamak için dolaylı bir metroloji yöntemi geliştirilmiştir. SiO<sub>2</sub> matrisi içerisinde oluşturulmuş olan Ge nanokristalleri FTIR, Raman ve XRD kullanılarak incelenmiştir. Ge atomlarının göreceli olarak daha düşük sıcaklıklarda SiO<sub>2</sub> matrisinden ayrıştığı FTIR kullanılarak anlaşılmıştır. Ge nanokristalleri ve SiO<sub>2</sub> matrisi arasındaki stress manyetron saçırma sistemindeki üretim koşullarına çok hassas bir biçimde bağlıdır. Si ve Ge iyonlarının Al<sub>2</sub>O<sub>3</sub> matrisinin içerisine ekilmesi ve sonrasında tavllanmasıyla Si ve Ge nanokristalleri oluşturulmuştur. Oluşan nanokristaller Raman, XRD, XPS ve TEM kullanılarak çözümlenmiştir. Nanokristal büyüklükleri XRD kullanılarak tahmin edilmiş olup, TEM'den bulunan değerlerle uyduğu bulunmuştur. Nanokristallerin üzerindeki gerilim (stress) Raman ve XRD kullanılarak gözlemlenmiş olup, niceliği Raman sonuçlarından hesaplanmıştır. Si ekilmiş ve tavllanmış örneğin XPS ve SIMS derinlik çizgeleri (profile) çıkarılmıştır. Sıcaklıkla beraber Si atomlarının nanokristalleri oluşturmak üzere çökelmeleri XPS ile gözlenmiştir. Si nanokristallerinin SiO<sub>x</sub> kabuğunun hacminin Si göbeğinin (core) hacmine olan oranı Si yoğunluğunun örnek içerisinde en fazla olduğu bölgede %7,9 olarak bulunmuştur.

Anahtar kelimeler : XRD, Raman, FTIR, XPS, spektroskopi, yarıiletken, nanokristal.

*To my lovely family,*

## ACKNOWLEDGMENTS

I would like to thank to my supervisor Prof. Dr. Raşit Turan who first gave me the opportunity to work with him. I am very grateful to him for his support and advice. I have tried to gain as much knowledge as possible from his vast experience. I believed I have succeeded in learning about writing scientific papers and reports, working systematically, loving laboratory instruments and imagining my samples in micro- and nano-scale. Finally, I am very grateful to him for giving me chance to cooperate with various people from various countries.

Among our diverse collaborations, I specially would like to thank to Prof. Dr. Atilla Aydınlı for his patient corrections in some of my papers and his friendly group, Prof. Dr. Terje Finstad for his helpful discussions, Prof. Dr. Mürvet Volkan and her group members for their support and sharing their Raman Spectrometer and knowledge, Prof. Dr. Macit Özenbaş for his helps in SEM measurements, Prof. Dr. Çiğdem Erçelebi and METU Central Laboratory staff for bearing my endless curiosity on various instruments. I would also thank to Prof. Dr. Yuval Golan and his student Michael Shandalov for TEM analysis, Prof. Dr. Jerry Wolowski and his student Marcin Rosinski for samples grown by laser ablation technique and Prof. Dr. Maria Gomes and Petra Candelas for samples grown by sputtering technique. It was a great chance for me to participate to MAMe group; Dr. Damiano Guibertoni, Dr. Mario Barozzi, Dr. Erica Iacob, and Dr. Vanetti Vanzetti, in Trento and to work under Dr. Massimo Bersani.

I appreciated meeting with Dr. Ali Alaçakır and Assoc. Prof. Dr. Akif Esendemir who supported my curiosity and enthusiasm towards laboratory equipments in the Laser Laboratory. Moreover, Assoc. Prof. Dr. Enver Blulur, Prof. Dr. Mehmet

Parlak, Dr. Uğur Serincan and off course my supervisor carried this flag later on during my studies on new subjects.

I am very happy to have enrolled in the Prof. Dr. Raşit Turan's group, Semiconductor Materials and Devices (SMD). I am most obliged towards Dr. Bülent Aslan, Dr. Giray Kartopu and Dr. Ercan Yılmaz for sharing their great knowledge with me. I would like to thank to my friends in the SMD group; Arife Gencer, İlker Yıldız, İlker Doğan, Seçkin Öztürk, Ayşe Seyhan, Mustafa Genişel, Sinan Alagöz, Nader Asgar, Savaş Ulucan, Umut Bostancı, Seda Bilgi, Sedat Canlı, Ayşe Arat, Eren Gülşen, Yücel Eke and especially Mustafa Kulakci for his sharing his insights relentlessly with me and his few high quality jokes.

Finally, I would like to thank to my friends who studied with me up to late evenings; Özgür Taskin, Nadir Ghazanfari, Çiçek Boztuğ, Yücel Özer, Esen Salçın, İlker Kılıç and Beste Korutlu, to my friends, İnanç Ortaç and Mehmet Uygur, with whom I love to discuss everything and to Çiğdem Özkan for correcting my English in this text.

Words are not enough to express my gratitude towards my mother Fatma Yerci, my father Sabri Yerci, my sister Selda Yerci. They have been exceptionally supportive and loving throughout my career.

## TABLE OF CONTENTS

ABSTRACT .....	iv
ÖZ .....	vi
DEDICATION .....	viii
ACKNOWLEDGMENTS .....	ix
TABLE OF CONTENTS .....	xi
LIST OF TABLES.....	xiii
LIST OF FIGURES .....	xiv
LIST OF ABBREVIATIONS.....	xviii
LIST OF SYMBOLS .....	xx
CHAPTER	
1. INTRODUCTION .....	1
1.1 Motivation .....	1
1.2 Nanomaterial Preparation and Characterization .....	5
1.3 Outline of the Thesis.....	10
1.4 References.....	11
2. CHARACTERIZATION OF NANOCRYSTALS USING FOURIER TRANSFORM INFRARED SPECTROSCOPY (FTIR).....	13
2.1 Introduction .....	13
2.2 Instrumentation.....	16
2.3 Probing Nanostructures with FTIR.....	17
2.3.1 Si and Ge nanocrystals in SiO <sub>2</sub> Formed by Ion Implantation .....	17
2.4 Conclusions.....	25
2.5 References.....	26

3.	CHARACTERIZATION OF NANOCRYSTALS USING RAMAN SPECTROSCOPY .....	28
3.1	Introduction.....	28
3.2	Instrumentation .....	35
3.3	Probing Nanostructures using Raman Spectroscopy .....	37
3.3.1	Si Nanocrystals in SiO <sub>2</sub> Formed by Ion Implantation .....	37
3.3.2	Ge Nanocrystals in SiO <sub>2</sub> Formed by Ion Implantation .....	39
3.3.3	Si Nanocrystals in Al <sub>2</sub> O <sub>3</sub> Formed by Ion Implantation .....	40
3.3.4	Ge Nanocrystals in Al <sub>2</sub> O <sub>3</sub> Formed by Ion Implantation.....	47
3.3.5	Ge Nanocrystals in SiO <sub>2</sub> Formed by Sputtering .....	52
3.3.6	Ge Nanocrystals in SiO <sub>2</sub> Formed by Laser Ablation.....	54
3.4	Conclusions .....	56
3.4	References .....	57
4.	CHARACTERIZATION OF NANOCRYSTALS USING X-RAY DIFFRACTION .....	59
4.1	Introduction .....	59
4.2	Instrumentation.....	61
4.3	Probing Nanostructures using XRD .....	63
4.3.1	Si Nanocrystals in Al <sub>2</sub> O <sub>3</sub> Formed by Ion Implantation .....	63
4.3.2	Ge Nanocrystals in Al <sub>2</sub> O <sub>3</sub> Formed by Ion Implantation.....	67
4.3.3	Ge Nanocrystals in SiO <sub>2</sub> Formed by Laser Ablation.....	71
4.4	Conclusions.....	73
4.5	References.....	74
5.	CHARACTERIZATION OF NANOCRYSTALS USING X-RAY PHOTOELECTRON SPECTROSCOPY .....	75
5.1	Introduction.....	75
5.2	Instrumentation .....	82
5.3	Probing Nanostructures with XPS .....	85
5.3.1	Si Nanocrystals in Al <sub>2</sub> O <sub>3</sub> Formed by Ion Implantation .....	85
5.4	Conclusions.....	94
5.5	References.....	95
6.	CONCLUSIONS AND FUTURE STUDIES .....	97
	Curriculum Vitea.....	99

## LIST OF TABLES

### TABLES

1.1	Some of the material characterization methods covered in this dissertation and their physical principles.....	7
1.2	Sets of samples, investigated in the thesis, their annealing conditions and their characterization methods.....	9
1.3	The details of the production methods performed in the thesis .....	9
3.1	The calculated crystalline ratio and the stress values of nanocrystals produced by different doses and annealing temperatures.....	45
3.2	Details of the production parameter of samples formed by sputtering.....	52
4.1	The calculated nanocrystal sizes at various crystals directions for samples formed by laser ablation.....	72
5.1	The doses and the respective projected ranges of the samples produced by ion implantation into $\text{Al}_2\text{O}_3$ .....	87

## LIST OF FIGURES

### FIGURES

1.1	Simplified energy diagram of light emission in a) direct and b) indirect band gap semiconductors (e.g. Si) .....	3
1.2	Schematics of MOS capacitors a) with floating gate b) with nanocrystals.....	4
1.3	Unit cells of a) SiO <sub>2</sub> and b) α-Al <sub>2</sub> O <sub>3</sub> . Oxygen atoms are shown as gray spheres and black spheres represented Si or Al .....	8
2.1	Types of the molecular vibrations.....	14
2.2	Schematics of a FTIR setup .....	17
2.3	The deconvolution of Si-O-Si asymmetric stretching vibrational mode around 1080 cm <sup>-1</sup> of thermally grown SiO <sub>2</sub> .....	19
2.4	The deconvolution of the Si-O-Si asymmetric stretching vibrational mode for <sup>74</sup> Ge implanted SiO <sub>2</sub> at a dose of 1×10 <sup>17</sup> <sup>74</sup> Ge/cm <sup>2</sup> .....	20
2.5	The deconvolution of the Si-O-Si asymmetric stretching vibrational mode for <sup>74</sup> Ge implanted SiO <sub>2</sub> at a dose of 1×10 <sup>17</sup> <sup>74</sup> Ge /cm <sup>2</sup> and annealed at 900 °C .....	21
2.6	TEM microimage of the Ge nanocrystals formed by ion implantation in SiO <sub>2</sub> matrix after an annealing of 900 °C .....	22
2.7	The change in a) the integrated area and b) the peak position of Si-O-Si bond stretching for SiO <sub>x</sub> and SiO <sub>2</sub> with the annealing temperature for samples implanted 1×10 <sup>17</sup> Si ions/cm <sup>2</sup> .....	24
2.8	TEM micro-image of sample implanted with 1×10 <sup>17</sup> Si/cm <sup>2</sup> and annealed at 1050 °C .....	25

3.1	Energy level diagram for Raman scattering a) Stokes b) Anti-Stokes..	29
3.2	First order Raman scattering of crystalline Si and nanocrystalline Si with various sizes .....	34
3.3	A representative confocal micro-Raman spectrometer setup.....	37
3.4	Raman spectra for samples implanted with $2 \times 10^{17}$ Si/cm <sup>2</sup> and annealed at 1100 °C .....	39
3.5	Raman spectra of samples implanted with $1 \times 10^{17}$ Ge/cm <sup>2</sup> and annealed at temperatures at 800, 900 and 1100 °C .....	40
3.6	Raman spectra of $\alpha$ -Al <sub>2</sub> O <sub>3</sub> implanted with the doses of $2 \times 10^{16}$ , $1 \times 10^{17}$ and $2 \times 10^{17}$ Si/cm <sup>2</sup> .....	42
3.7	The evolution of Raman signal for the doses of $1 \times 10^{17}$ and $2 \times 10^{17}$ Si/cm <sup>2</sup> implanted samples with annealing temperature .....	44
3.8	The difference between Stokes and anti-Stokes shifts of a Raman spectrum at room temperature (“*” shows the Silicon peak and “#” indicates the Al <sub>2</sub> O <sub>3</sub> peak) .....	46
3.9	Raman spectra of the samples implanted with doses of $5 \times 10^{16}$ Ge ions/cm <sup>2</sup> and $1 \times 10^{17}$ Ge ions/cm <sup>2</sup> and annealed samples at 600 °C .....	48
3.10	TEM micrograph for a sample implanted with a dose of $1 \times 10^{17}$ Ge ions/cm <sup>2</sup> subsequently annealed at and c) 800 °C. The arrows show the separate areas which includes Ge nanocrystals having different size distributions.....	50
3.11	Raman spectra of the samples implanted with doses of $5 \times 10^{16}$ Ge ions/cm <sup>2</sup> and $1 \times 10^{17}$ Ge ions/cm <sup>2</sup> after annealing at temperatures of 600, 700 and 800 °C. The dotted line shows the Raman position of 300 cm <sup>-1</sup> to guide the eye .....	51
3.12	Raman spectra of the samples produced by sputtering .....	53
3.13	AFM images of the samples produced by sputtering.....	54
3.14	Raman spectra of the samples produced by laser ablation.....	55
4.1	Schematic of a XRD spectrometer with its components.....	62
4.2	XRD spectrum of a standard poly-Si which may be used to find the instrumental broadening.....	63

4.3	The evolution of XRD signal of Si implanted $\alpha$ -Al <sub>2</sub> O <sub>3</sub> matrix as a function of implantation dose and annealing temperature. (*) indicates the Si (111) peaks. Inset shows details of Si (111) peaks.....	65
4.4	Si (111) XRD peak at 28.6°. Solid line is a fit to data using a pseudo-Voigt function .....	66
4.5	XRD spectra of the samples implanted with doses of a) $5 \times 10^{16}$ Ge ions/cm <sup>2</sup> and b) $1 \times 10^{17}$ Ge ions/cm <sup>2</sup> and subsequently annealed at temperatures of 700 and 800 °C. Ge (111) signal is marked with (#) .....	69
4.6	HRTEM micrograph of the sample implanted with $1 \times 10^{17}$ Ge/cm <sup>2</sup> and subsequently annealed at 800 °C .....	70
4.7	XRD spectra of the samples produced by laser ablation.....	71
5.1	A representative energy diagram of the photoemission process in XPS (adapted from ref. 1).....	76
5.2	Background correction for Ge 2p peak by using Tougaard and Shirley methods .....	77
5.3	Deconvolution of O 1s peak with a Gaussian, a Lorentzian and a combined (Gaussian + Lorentzian) fit .....	78
5.4	Representative diagram for XPS measurement setup .....	83
5.5	SIMS depth profile of the samples prepared by ion implantation with different doses.....	86
5.6	XPS depth profile of the O 1s signals of sapphire samples implanted with a dose of $2 \times 10^{17}$ Si/cm <sup>2</sup> .....	89
5.7	XPS depth profile of the Si 2p signals of sapphire samples implanted with a dose of $2 \times 10^{17}$ Si/cm <sup>2</sup> .....	90
5.8	XPS depth profile of the O 1s signals of sapphire samples implanted with a dose of $2 \times 10^{17}$ Si/cm <sup>2</sup> and annealed at 1000 °C for 1 h under N <sub>2</sub> environment .....	91
5.9	XPS depth profile of the Si 2p signals of sapphire samples implanted with a dose of $2 \times 10^{17}$ Si/cm <sup>2</sup> and annealed at 1000 °C for 1 h under N <sub>2</sub> environment .....	92

5.10 Si 2p XPS signals for various Si<sup>n+</sup> states of sample a) implanted with a dose of 2x10<sup>17</sup> Si ions/cm<sup>2</sup> and b) subsequently annealed at 1000 °C under N<sub>2</sub> ambient ..... 93

## LIST OF ABBREVIATIONS

AFM	Atomic Force Microscopy
AS	Asymmetric Stretching
CCD	Charge Coupled Device
CMOS	Complementary Metal Oxide Semiconductor
DTGS	Deuterium Tryglycine Sulphate
EDS	Energy Dispersive Spectroscopy
EPR	Electron Paramagnetic Resonance
ESCA	Electron Spectroscopy for Chemical Analysis
FTIR:	Fourier Transform Infrared Spectroscopy
FWHM	Full Width Half Maximum
HRTEM	High Resolution Transmission Electron Microscopy
LED	Light Emitting Diodes
LO	Longitudinal Acoustic
MCT	Mercury Cadmium Telluride
PL	Photoluminescence
PLQE	Photoluminescence Quantum Efficiency
QED	Quantum Electronic Devices
PMT	Photomultiplier Tube
RERS	Resonance-Enhanced Raman Scattering
RS	Raman Spectroscopy
SEM	Scanning Electron Microscopy
SERS	Surface-Enhanced Raman Scattering
SET	Single Electron Transistor
SIMS	Secondary Ion Mass Spectrometry

STM	Scanning Tunneling Microscopy
XPS	X-Ray Photoelectron Spectroscopy
XRD	X-Ray Diffraction
XRF	X-Ray Fluorescence
TA	Transverse Acoustic
TO	Transverse Optical
TEM	Transmission Electron Microscopy
UHV	Ultra High Vacuum

## LIST OF SYMBOLS

A	absorbance
A	area of the sample from which photoelectrons are detected
A	calibration constant of the band
a	lattice constant
$\alpha$	absorption coefficient
$\alpha$	polarizability
$\beta$	X-Ray diffraction broadening
$C(0,q)$	Fourier coefficient of phonon confinement function
c	concentration
D	coherence length
d	thickness
d	interplanar spacing
E	electric field strength
$E_B$	Binding Energy
$E_{kin}$	kinetic energy of the photoelectrons
f	X-Ray flux
$\phi$	work function
$\Gamma$	angular efficiency of the atomic orbital in XPS
$\gamma$	ratio of the concentrations of oxygen and silicon
I	integrated area of the XPS peak
$\Gamma_0$	natural Raman linewidth of the bulk material
$I(w)$	Intensity of the Raman peak
$I_a$	Raman intensity of the amorphous peak

$I_c$	Raman intensity of the crystalline peak
$I_S$	Raman intensity of the stokes shift
$I_{AS}$	Raman intensity of the anti-stokes shift
$\kappa$	Scherrer's constant
$L$	nanocrystals size
$\lambda$	mean free path for photoelectrons
$\lambda_{incident}$	wavelength of the incident photons
$\lambda_{scattered}$	wavelength of the scattered photons
$\mu$	dipole moment
$\mu$	ratio of the densities of Si and SiO <sub>2</sub>
$n$	refractive index
$\nu_0$	frequency of the laser
$\nu_{peak}$	peak position
$q$	nuclear displacement
$q_0$	vibrational amplitude
$R_p$	projection range of implantation
$\Theta$	half of the deviation of diffracted beam in XRD
$\rho$	ratio of the Raman efficiencies for crystalline to amorphous Si
$S$	atomic sensitivity factor
$\sigma$	photoelectric cross section
$T$	transition probability
$T$	detection efficiency of the electron detector in XPS
$w(q)$	phonon dispersion of the bulk material
$\Delta w_s$	stress induced wavenumber shift
$y$	efficiency of the photoelectric process

## CHAPTER 1

### INTRODUCTION

#### 1.1 Motivation

After the invention of transistor, by Bardeen, Brattain and Shockley in 1947, a never ending revolution called microelectronic industry started [1]. The evolution of this industry fitted to an empirical theory, Moore's law that ruled up to now. Moore's law is an empirical observation that component density and performance of integrated circuits doubles every two years [2, 3]. This observation has enabled by two factors; continuous reduction of the feature sizes and major changes during the evolution. The feature sizes have shrunk with the developments in the lithography and the industry has moved from Si bipolar to p-channel metal oxide semiconductor (MOS), then to n-channel MOS, and finally to Complementary MOS (CMOS) planar transistors. Transistor feature size has scaled from 10  $\mu\text{m}$  to  $\sim 30$  nm during the past 40 years. However, a big challenge looking forward is that the end of planar CMOS transistor scaling is near as the transistor size approaches tens of nanometers. The scales of lithography and transistors are the main limiting factors. Optical lithography can further be enhanced so that an exposure can be patterned at the 22 nm node [4]. However, another limit arises from the leakage current at small gate length. It is thought that the practical consideration on leakage limit the physical gate length to  $\sim 20$  nm. Parasitic resistance and capacitance, increase in contact resistance and contact-to-gate capacitance over channel resistance and capacitance, are another limit resulted from the decreasing late length [5].

The future of opto-electronics industry lay on either replacing the Si with another material (Ge, III-V, Carbon nanotubes, Quantum Electronic Devices (QED), Single Electron Transistor (SET), or spintronics) or engineering Si so that it manages the challenges. Among the possible solutions; Ge and II-V materials are very expensive, (~1000 times more expensive than Si), Carbon nanotubes have very low-density-of-states making it difficult to achieve high drive currents [5]. As a final motivation, one can say that Si CMOS will be dominant for the foreseeable future. This thesis is adapted to engineer the silicon as a form of nanocrystal to manage the some of the challenges

Optical data transmission process integrated within a chip is required to increase the communication speeds. This demand can be realized by the integration of microelectronics and optoelectronics [6]. A new technology, Si based optoelectronics (or Si photonics), has been receiving more and more attention recently. Si based active optical components such as lasers or Light Emitting Diodes (LEDs) [7-11], modulators [12], amplifiers [13] and waveguides [14] are under intensive investigations. Unfortunately, bulk Si with its indirect band gap (Fig. 1.1) needs assistance of a phonon to emit light and therefore has a long radiative lifetime (in the order of milliseconds). Long lifetime is not a physical limit for an active light emitter [6, 15]. Real limit comes from the competition of lifetimes of radiative and non-radiative processes. Lifetimes for typical non-radiative processes such as free carrier absorption, Auger recombination or other recombinations through defects, traps and dopants are in the order of nanoseconds. Therefore bulk Si is a poor light emitter (internal Photoluminescence Quantum Efficiency (PLQE) of the electronic grade Si is  $\sim 10^{-4}\%$ ) [15]. It has been known for more than two decades that sufficiently small Si nanocrystals can emit light more efficiently compared to bulk Si due to the decrease in the number of non-radiative centers [16, 17]. Recently, the internal PLQE of Si nanocrystals was measured around 60 % [18]. On the other hand, the external PLQE of Si nanocrystals was measured around 4.5% [19]. These attractive results are due to the well passivation of Si nanocrystals rather than a change in band gap from indirect to direct behavior.

These developments in PL efficiency have been followed by the production of efficient Si nanocrystal based Light Emitting Diodes (Si-nc LED) [7-9]. Recently, efficiencies reaching 1% has been reported [7, 8].

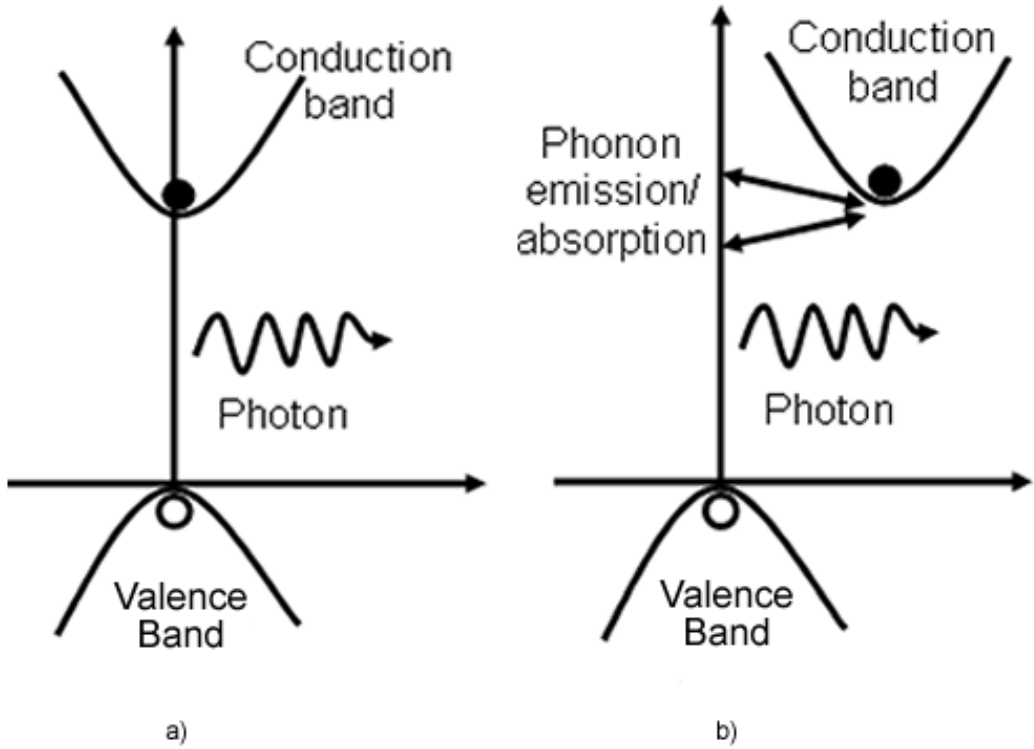


Fig. 1.1. Simplified energy diagram of light emission in a) direct and b) indirect band gap semiconductors (e.g. Si).

Non-volatile memory devices such as flash memories are another application area where semiconductor nanocrystals are expected to play an important role. Traditional memory devices are metal-oxide capacitors (MOS) with a floating gate

embedded in oxide layer. The layer that isolates the channel and the floating gate is usually  $\text{SiO}_2$  (or recently  $\text{SiON}$ ) with a thickness of 7-10 nm [20]. Charge can be injected to or extracted from the floating gate through this layer. This layer is called as tunnel oxide due to the injection mechanism is dominated by Fowler-Nordheim tunneling [20]. However, this structure has a disadvantage that all information can be lost in the existence of a leakage current. On the contrary, in the nanocrystal based memory devices, losing charge stored in only one dot or several dots does not affect the overall work of the device [20-22]. Moreover, nanocrystal based memory devices are expected to work with high speeds for write and erase operations and low-power consumptions. Schematic cross section of MOS capacitors with floating gate and nanocrystals are shown in Fig.1.2.

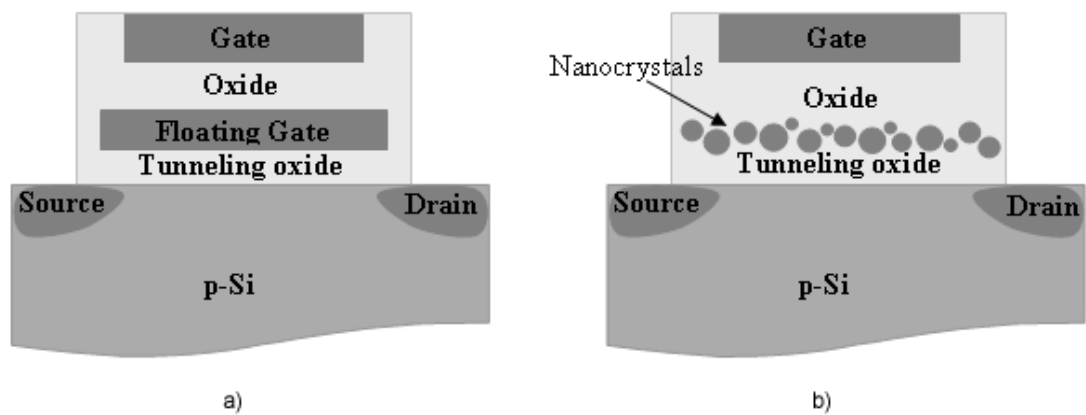


Fig. 1.2. Schematics of MOS capacitors a) with floating gate b) with nanocrystals.

While LED and MOS structures are two most popular applications for semiconductor nanocrystals much effort have been reported to develop semiconductor nanocrystal based solar cells [23].

## 1.2 Nanomaterial Preparation and Characterization

Recently, many effective techniques (i.e. magnetron sputtering, ion implantation, chemical vapor deposition, thermal evaporation, chemical synthesis, and laser ablation) have been employed to form CMOS compatible nanostructures in large quantities. The nanocrystals formation process can be explained as 1) the production of Si or Ge rich oxides, 2) coalescence of excess atoms and clusters in the matrix to form nanocrystals with annealing. Therefore, one can say that formation of nanostructures using these methods is a thermodynamically driven self-assembly process. Characterization of the formed structure is extremely important to develop new devices using these materials. Various diagnostic techniques are employed to monitor the formation of the nanocrystals, to observe the electrical, optical or structural properties of the nanocrystals or to detect the environment surrounding the nanocrystals. Many physical principles; diffraction, scattering and absorption of electron and light are used in characterization. Some of the methods frequently used in material characterization and their physical principle are given in Table 1. Among them, the methods marked with dark background color are extensively studied in this dissertation while those with light background color are used as supporting methods to confirm the results obtained using the first group.

Fourier transform infrared (FTIR) spectroscopy and Raman spectroscopy are two methods used widely to extract information using vibrational states. While absorption of infrared light having an energy equals to the energy difference of two vibrational states is recorded in FTIR, an inelastic scattering of visible (it can also be IR or UV) light with an energy shift which is equal to energy of a phonon is considered in Raman spectroscopy. Another scattering technique, X-Ray diffraction is based on elastic scattering of X-rays which are emitted at characteristic angles depending on the atoms organized in crystal structures. X-ray with its small wavelength is quite useful in characterization in atomic scales. Another method, X-ray photoelectron spectroscopy emerges from the analysis of the kinetic energies of electrons which are removed from the core levels of atoms by X-rays.

FTIR and XPS are two techniques that can be used complementarily. Both give information about the chemical environment which is very crucial to understand the luminescence properties of nanocrystals. XPS can also be used to find the chemical structure of the surface. On the other hand, XRD and Raman spectroscopy gives information about the crystallinity of the nanoclusters and the stress exerted on them.

Table 1.1: Some of the material characterization methods covered in this dissertation and their physical principles

Method	Physical Principle
Fourier Transform Infrared Spectroscopy (FTIR)	Absorption of polychromatic IR light in vibrational bands
Raman Spectroscopy (RS)	Scattering of monochromatic light in vibrational bands
X-Ray Diffraction (XRD)	Diffraction of X-Ray from crystals lattices
X-Ray Photoelectron Spectroscopy (XPS)	Extracted electrons, analyzed according to their kinetic energies
Secondary Ion Mass Spectrometry (SIMS)	Secondary ions, analyzed with mass spectrometry
Transmission or Scanning Electron Microscopy (TEM or SEM)	Transmission or scattering of electrons
Atomic Force Microscopy (AFM)	Electrostatic force or tunneling current between sample and tip
Energy Dispersive Spectroscopy (EDS)	Fluorescent X-Ray during SEM
Photoluminescence (PL)	Luminescence of material under optical excitation conditions

In this work, seven sets of sample were studied. Si and Ge nanocrystals were formed in  $\text{SiO}_2$ , and  $\text{Al}_2\text{O}_3$  matrices, ion implantation, magnetron sputtering, and laser ablation. The unit cells of  $\text{SiO}_2$  and  $\text{Al}_2\text{O}_3$  are given in Fig. 1.3. List of the samples, their annealing conditions and their characterization methods are given in Table 1.2. Annealing Moreover, the details of the production methods covered in this thesis are given in Table 1.3.

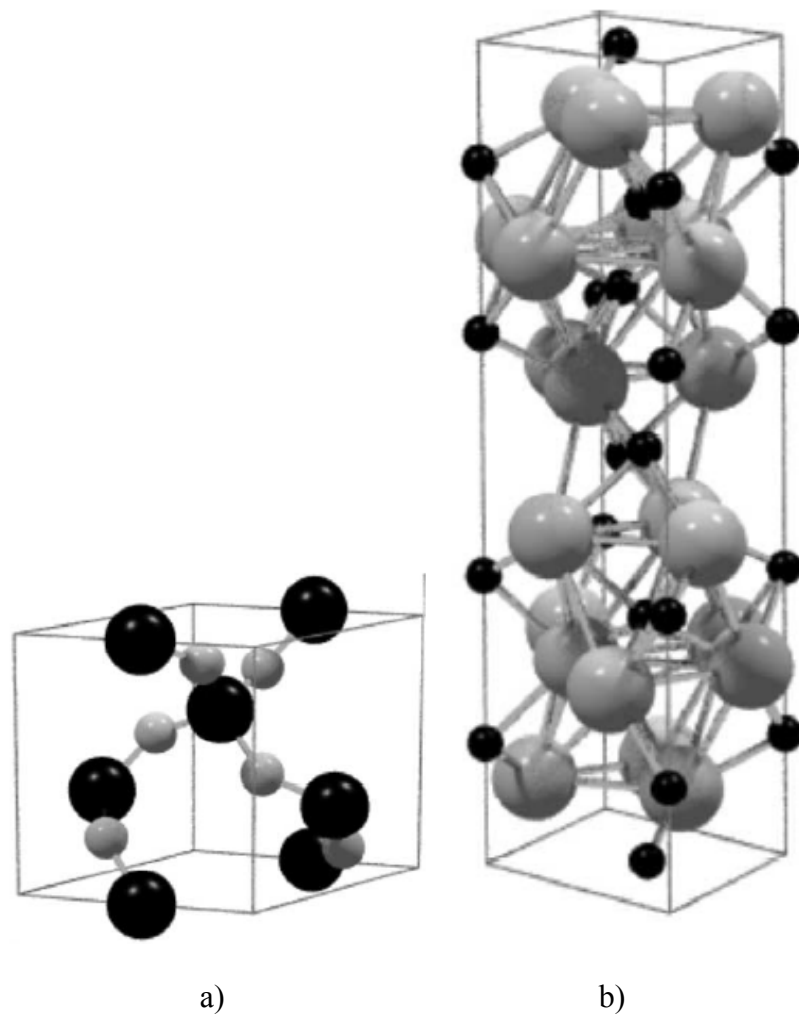


Fig. 1.3. Unit cells of a)  $\text{SiO}_2$  and b)  $\alpha\text{-Al}_2\text{O}_3$ . Oxygen atoms are shown as gray spheres and black spheres represented Si or Al [24]

Table 1.2. Sets of samples, investigated in the thesis, their annealing conditions and their characterization methods

Production Method	Nano-crystal	Oxide Matrix	Annealing Temp. (°C)	Annealing Time (h)	Investigation Method
Ion Implantation	Si	SiO <sub>2</sub>	800-1100	2	RS, FTIR, SIMS
	Ge	SiO <sub>2</sub>	800-1100	2	RS, FTIR, SIMS
	Si	Al <sub>2</sub> O <sub>3</sub>	600-1100	1	RS, XRD, SIMS, XPS, PL
	Ge	Al <sub>2</sub> O <sub>3</sub>	500-900	1	RS, XRD, XPS, PL, TEM, AFM, EDS, SEM
Sputtering	Ge	Al <sub>2</sub> O <sub>3</sub>	100, 500	-	RS, XPS, SIMS
Laser Ablation	Ge	SiO <sub>2</sub>	750	0.5	RS, SIMS

Table 1.3. The details of the production methods performed in the thesis

Ion Implantation		Sputtering		Laser Ablation	
Energy (keV)	100	RF Power (W)	40	Power (10 <sup>10</sup> W)	1.1
Dose (10 <sup>16</sup> / cm <sup>2</sup> )	5-20	Duration (min)	180	Spot Area (mm <sup>2</sup> )	12
		Distance* (mm)	60	Distance* (mm)	6
		Pressure (x10 <sup>-3</sup> mbar)	2-10		

\*: the distance between substrate and the target.

### **1.3 Outline of the Thesis**

In this thesis, the analytical methods used in the characterization of group IV nanocrystals formed in oxide matrices are discussed. Chapter 2 discusses the use of FTIR spectroscopy in characterization. A new method is proposed to observe the formation of Si nanocrystals in SiO<sub>2</sub> matrix. Chapter 3 and 4 deal with the Raman spectroscopy and XRD, respectively. Calculations of the nanocrystal dimension and the stress exerted on them by the matrix were presented. Moreover, the crystallinity behaviors of nanoclusters using these methods are discussed. In chapter 5, characterization of Si and Ge nanocrystals in Al<sub>2</sub>O<sub>3</sub> and SiO<sub>2</sub> matrices using XPS is concerned. Finally, in chapter 6, a summary was constructed to give the important conclusions of this thesis and possible future research direction that can be built up on this work is proposed.

## 1.4 References

1. J. Bardeen, and W. H. Brattain, *Phys. Rev.* 75, 1208, 1949.
2. G. E. Moore, *Electronics* 38, 114, 1965.
3. G. E. Moore, *Tech. Dig. IEDM* 21, 11, 1975.
4. B. Lin, *Tech. Dig. IEDM* 48, 2005.
5. S. E. Thompson and S. Parthasarathy, *Materials Today*, 9 (6), 20, 2006.
6. *Silicon Photonics*, *Topics in Applied Physics Series Vol. 94*, edited by L. Pavesi and D. J. Lockwood (Springer-Verlag, Berlin, 2004).
7. P. M. Fauchet, *IEEE Journal of Quantum Electronic*, Vol. 4, No. 6, 1020, 1998.
8. R. J. Walters, G. I. Bourianoff, H. A. Atwater, *Nature Materials* 4, 143, 2005.
9. M. Kulakci, U. Serincan, and R. Turan, *Semicond. Sci. Technol.* 21, 1527, 2006.
10. A. Fojtik, J. Valenta, I. Pelant, M. Kalal, and P. Fiala, *J. Mater. Proc. Tech.* 181, 88, 2007.
11. O. Boyraz and B. Jalali, *Optics Express* 12, 5269, 2004.
12. V. R. Almeida, C. A. Barrios, R. R. Panepucci, and M. Lipson, *Nature*, 431, 1081, 2004.
13. C. J. Oton, W. H. Itoh, and A. J. Kenyon, *Appl. Phys. Lett.*, 89, 031116, 2006.
14. P. Pellegrino, B. Garrido, C. Garcia, J. Arbiol, J. R. Morante, M. Melchiorri, N. Dalbosco, L. Pavesi, E. Scheid, and G. Sarraibayrouse, *J. Appl. Phys.* 97, 074312, 2005.
15. K. Luterova, K. Dohnalova, F. Trojanek, K. Neudert, P. Gilliot, B. Honerlage, P. Maly, and I. Pelant, *J. Non-cryst. Solids*, 352, 3041, 2006.
16. L. T. Canham, *Appl. Phys. Lett.* 57, 1046, 1990.
17. V. Lehmann and U. Gösele, *Appl. Phys. Lett.* 58, 856, 1991.
18. R. J. Walters, J. Kalkman, A. Polman, H. A. Atwater, and D. A. de Dood, *Phys. Rev. B*, 73, 132302, 2006.
19. L. Dal Negro, J. H. Yi, J. Michel, L. C. Kimerling, T. W. F. Chang, V. Sukhovatkin, and E. H. Sargent, *Appl. Phys. Lett.*, 88, 233109, 2006.

20. D. Tsoukalas, P. Dimitrikas, S. Kolliopoulou, and P. Normand, *Mater. Sci. Engr. B*, 124-125, 93, 2005.
21. S. Tawari, F. Rana, H. Hanafi, A. Harstein, E. F. Crabbe, and K. Chan, *Appl. Phys. Lett.*, 68, 1377, 1996.
22. J. Wahl, H. Silva, A. Gokirmak, A. Kumar, J. J. Welser and S. Tawari, *IEDM 1999 Technical Digest*. 375-378, 1999.
23. V. Svrcek, A. Slaoui, J. C. Muller, *Thin Solid Films* 451, 384, 2004.
24. H. A. Al-Abadleh and V. H. Grassian, *Sur. Sci. Rep.*, 52, 63, 2003.

## CHAPTER 2

### CHARACTERIZATION OF NANOCRYSTALS USING FOURIER TRANSFORM INFRARED SPECTROSCOPY

#### 2.1 Introduction

Infrared spectroscopy deals with the absorption of infrared light in vibrational states of molecules. The most powerful aspect of infrared spectroscopy is that it allows us to identify unknown chemical species. Once the wavenumber positions of the bands of a functional group are known, this information can be used to identify that functional group in samples of any type. Moreover, the peak intensities of an infrared spectrum can be used to measure the concentrations as well.

Absorption of infrared light in the vibrational states of a molecule depends on the transition probability,  $T$ , of the phonon between two states, is proportional to the square of the change in dipole moment  $\mu$  [1].

$$T \propto \left( \frac{\partial \mu}{\partial x} \right)^2 \quad (2.1)$$

Net change in dipole moment can be realized in several geometrical conditions as shown in Fig. 2.1. Among them, bending can be one of the four types according to direction of the bending. These are rocking, scissoring, wagging, and twisting.

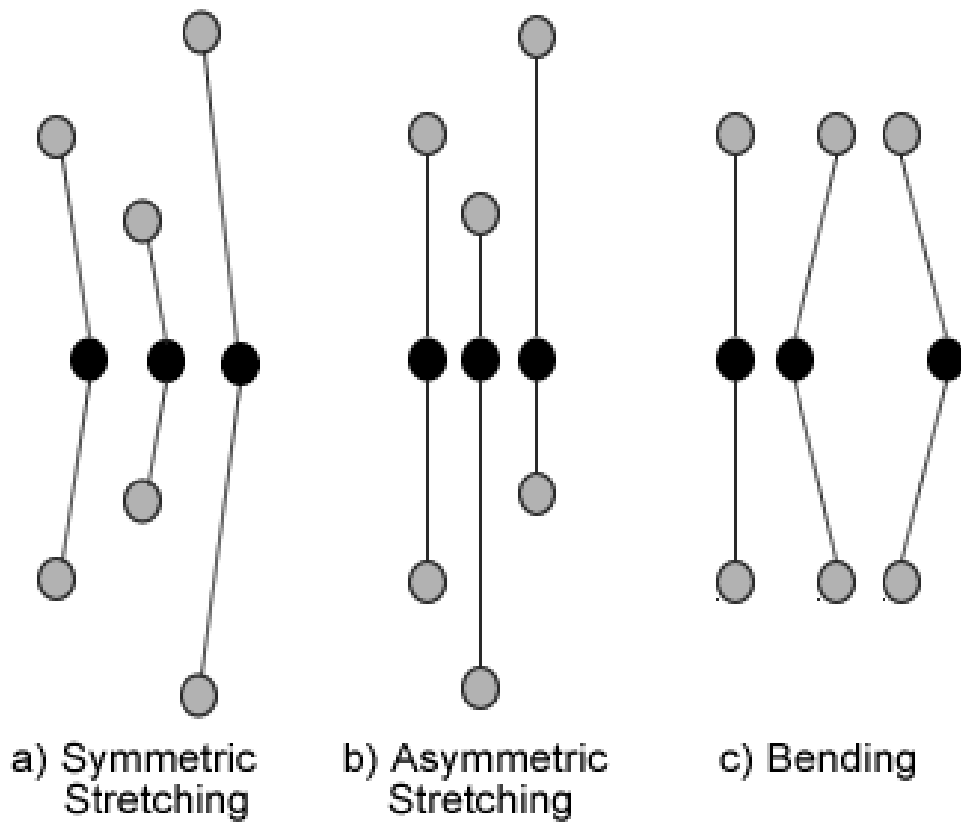


Fig. 2.1. Types of the molecular vibrations

Lambert found that the amount of light transmitted through a solid sample was dependent on the thickness of the sample in the eighteenth century. This was extended by the solutions by Beer, during the following century. The resulting Beer-Lambert Law can be derived theoretically and applied to all electromagnetic radiation [2]. According to Beer-Lambert theorem, absorbance,  $A$ , can be expressed as,

$$A = \log\left(\frac{I}{I_0}\right) = \alpha \otimes c \otimes d \quad (2.2)$$

where,  $\alpha$  is the absorption coefficient,  $c$  is the concentration, and  $d$  is the thickness of the film.

Production of homogenous  $\text{SiO}_x$  ( $0 \leq x \leq 2$ ) is crucial to form nanocrystals with narrow size distribution. Therefore, methods sensitive to chemical composition such as XPS and FTIR are extensively used to characterize  $\text{SiO}_x$ , where the value  $x$  indicates the amount of excess Si in  $\text{SiO}_2$  [3-12]. Moreover,  $x$  is proportional with the nanocrystal density which is a very significant parameter to intensify or quench the optical emission [13, 14]. In addition with  $x$ , the variation of the electrical properties of  $\text{SiO}_2$  matrix containing Si nanocrystals was investigated [15].

Tsu et. al. developed an empirical relation to find the  $x$  value for  $\text{SiO}_x$  produced by plasma enhanced chemical vapor deposition (PECVD) [3],

$$\nu_{\text{Si-O}} = 965 + 50x \quad (2.3)$$

which assumes that the peak position of Si-O-Si asymmetric stretching band for  $\text{SiO}$  molecule is at  $965 \text{ cm}^{-1}$  and when  $x$  is equal to 2, the band position becomes  $1080 \text{ cm}^{-1}$ .

Another empirical relation was suggested by Dehan et. al. between the refractive index,  $n$ , and the ratio of the concentrations of oxygen and silicon,  $\gamma$  [16]. They assume that the  $\text{SiO}_x$  media is a mixture of a-Si and  $\text{SiO}_2$ . This relation is given as follows,

$$n(\gamma) = 4 - 2.53\gamma + 0.63\gamma^2 \quad (2.4)$$

As the  $\text{SiO}_2$  matrix grown on Si-substrate is widely used in microelectronic industry especially in MOS capacitor the formation and characterization of  $\text{SiO}_2$ -Si interface attracts much attention [17]. In order to use the FTIR spectroscopy to find the concentration of Si-O bonds,  $C(\text{Si-O})$ , the following method was developed [18, 19],

$$C(\text{Si-O}) = AI(\text{Si-O}) = A \int \frac{\alpha(\nu)}{\nu_{\text{peak}}} d\nu \quad (2.5)$$

where  $\nu_{\text{peak}}$  is the peak position,  $\alpha$  is the absorption coefficient, and  $A$  is the calibration constant of the band.  $A$  can be taken as  $1.5 \times 10^{19} \text{ cm}^{-2}$  [19].

Although some of the possible quantitative calculations using FTIR spectroscopy was given above a qualitative study on the deconvolution of Si-O-Si asymmetric stretching band located around  $1080 \text{ cm}^{-1}$  will be discussed in section 2.3.1.

## 2.2 Instrumentation

Infrared light sources and detectors are less efficient than their visible counterparts. Therefore, dispersive systems have been replaced by systems based on Michelson Interferometer such as Fourier Transform Infrared (FTIR) spectrometer. The layout of such an instrument is given in Fig. 2.2. IR naturally cannot be seen with the naked eye and therefore a laser is used for alignment. A polychromatic light source, an electrically heated SiC wire, is used to produce a continuous mid infrared radiation, approximating a blackbody radiation. Furthermore, mercury arc and tungsten filament lamps are used in far infrared and in near infrared regions, respectively. The Michelson interferometer consists of two perpendicular mirrors, one of which is stationary while the other moves at a constant velocity. Between the mirrors, there is a beam splitter, by which the incoming beam is divided, and later recombined after a path difference has been introduced between the beams shown in Fig. 2.2. The path difference can later be transformed to the frequency using Fourier transform method. The IR beam incident to the detector is called an interferogram which is the light intensity as a function of time. Deuterium Tryglycine Sulphate (DTGS) and Mercury Cadmium Telluride (MCT) are two types of detectors used frequently in IR detection [2].

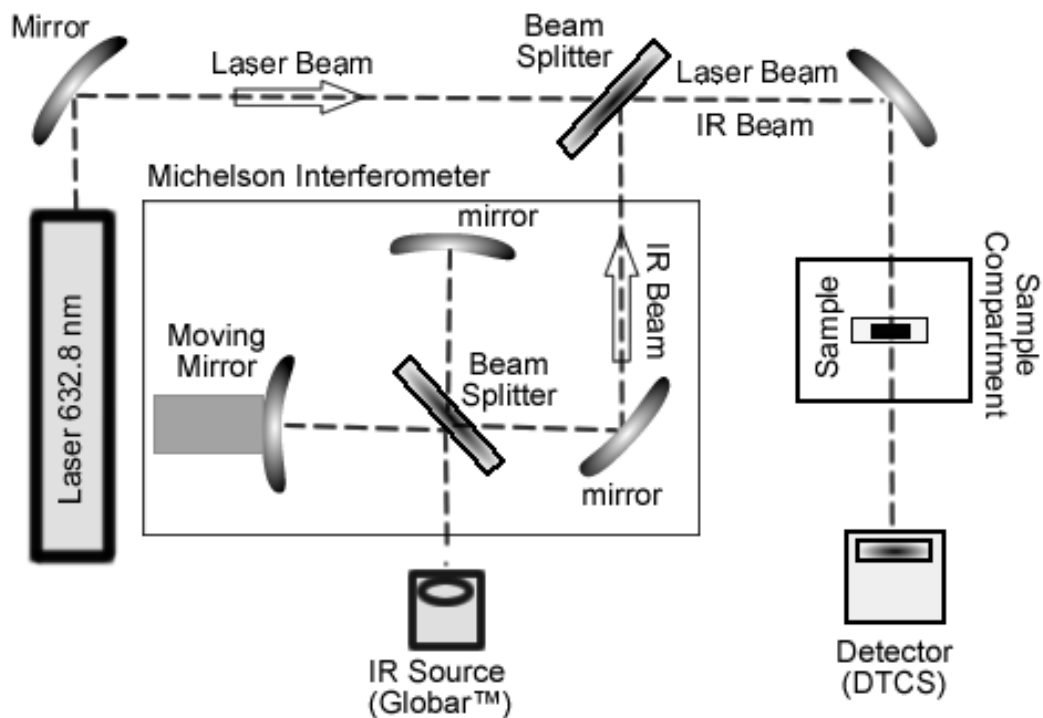


Fig. 2.2. Schematics of a typical FTIR setup

FTIR spectroscopy was measured using Equinox spectrometer (Bruker), located in the Department of Physics at METU, in the absorbance mode at wavenumbers between  $400\text{--}4000\text{ cm}^{-1}$  with a resolution of  $4\text{ cm}^{-1}$ .

## 2.3 Probing Nanostructures with FTIR

### 2.3.1 Si and Ge nanocrystals formed into SiO<sub>2</sub> by ion implantation

Thermally grown 250 nm thick SiO<sub>2</sub> films on (100) Si wafers were implanted with <sup>74</sup>Ge or <sup>28</sup>Si ions at an energy of 100 keV with a dose of  $1.0 \times 10^{17}$  ions/cm<sup>2</sup>. The projected range ( $R_p$ ) of the Ge and Si ions were calculated by using the TRIM [20] software as 70.0 and 140.0 nm, respectively. Samples were annealed at 800–1200 °C for 2 h under N<sub>2</sub> atmosphere.

The FTIR spectrum of bulk SiO<sub>2</sub>, <sup>28</sup>Si and <sup>74</sup>Ge implanted SiO<sub>2</sub> films were measured from 400 to 4000 cm<sup>-1</sup> at normal incidence with unpolarized light and the following peaks are observed: 459 cm<sup>-1</sup> (rocking), 806 cm<sup>-1</sup> (bending) and 1080 cm<sup>-1</sup> (stretching) [21]. The deconvolution procedure was applied to the highest frequency vibrational mode (i.e. Si-O-Si asymmetrical vibration) between 875 to 1300 cm<sup>-1</sup> due to its clear modification at the occurrence of SiO<sub>x</sub> (x<2) bonds (i.e. Si-(SiO<sub>3</sub>), Si-(Si<sub>2</sub>O<sub>2</sub>) and Si-(Si<sub>3</sub>O) [7] and it was performed as sums of Lorentz/Gauss asymmetric peaks. In Fig. 2.3, the deconvolution of thermally grown SiO<sub>2</sub> is given and was used as a reference to observe the recovery of the SiO<sub>x</sub> structure during the annealing process. On low frequency side the only peak is located at 1079 cm<sup>-1</sup> which belongs to well-known Si-O-Si asymmetric stretching vibration mode (AS<sub>1</sub>). The higher frequency peaks can be attributed to another Si-O-Si asymmetric stretching vibrational mode (AS<sub>2</sub>) (~1210), in which the oxygen atoms move out of phase and the disorder-induced LO<sub>2</sub> (~1160) vibrational mode [8]. Due to its low intensity, LO<sub>1</sub> at around 1250 cm<sup>-1</sup> is not included at the peak fitting procedure [8, 9].

The deconvolution procedure was applied to the same peak after <sup>74</sup>Ge implantation to SiO<sub>2</sub> with a dose of  $1.0 \times 10^{17}$  ions/cm<sup>2</sup> (Fig. 2.4). After ion implantation a new peak emerges at 1037 cm<sup>-1</sup>, which is related to presence of the Si-O bond stretching vibration in SiO<sub>x</sub> [10]. The presence of this peak is expected due to the ion implantation. The introduction of excess Ge and Si with high momentum into the

matrix breaks the Si-O bonds during slowing down of the implanted atoms and forms an inhomogeneous  $\text{SiO}_x$  matrix.

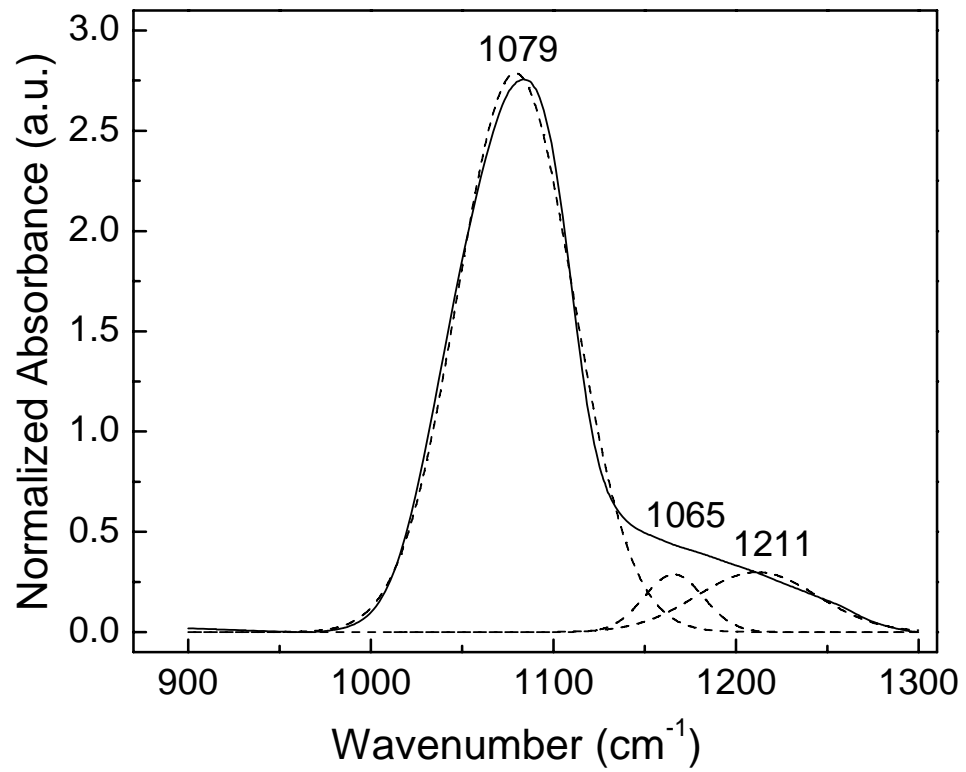


Fig. 2.3. The deconvolution of Si-O-Si asymmetric stretching vibrational mode around  $1080 \text{ cm}^{-1}$  of thermally grown  $\text{SiO}_2$

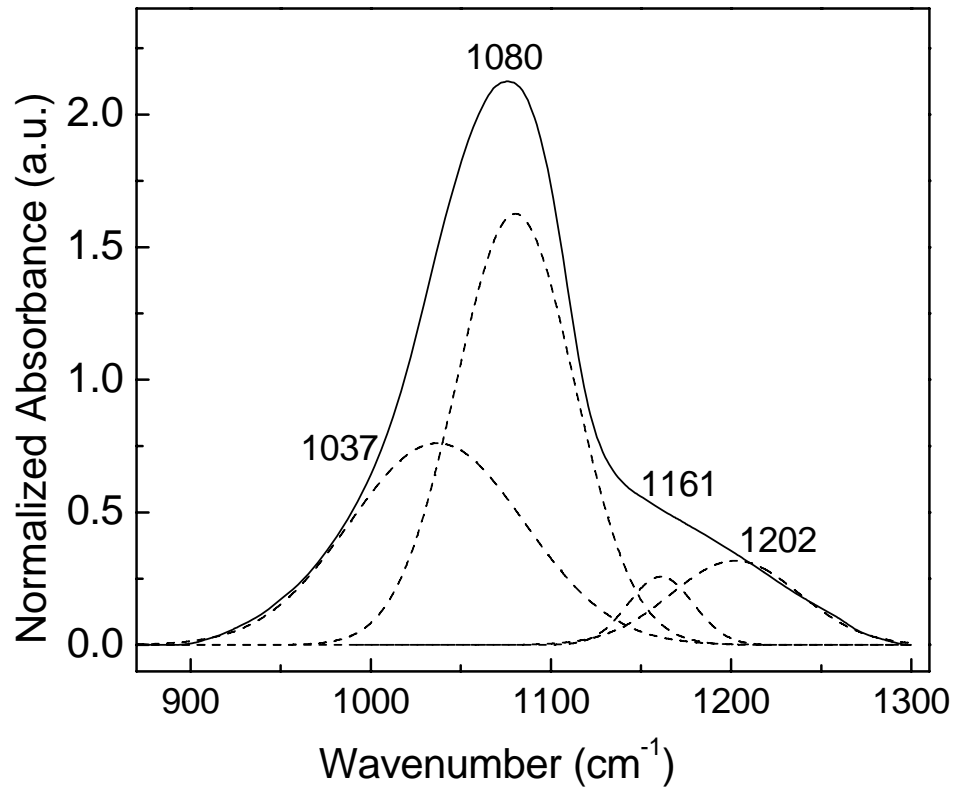


Fig. 2.4. The deconvolution of the Si-O-Si asymmetric stretching vibrational mode of SiO<sub>2</sub> implanted with a dose of  $1 \times 10^{17} \text{ } ^{74}\text{Ge} / \text{cm}^2$

Ge ions have the highest concentration at around 70 nm of SiO<sub>2</sub> film for 100 keV and at the peak position of the Ge ion concentration reaches about 10% of SiO<sub>2</sub> matrix. Thus, implantation creates a layer whose stoichiometry is partially altered. During the annealing process, the SiO<sub>2</sub> starts to recover and Ge nanocrystals form. The deconvolution of FTIR spectrum for the same <sup>74</sup>Ge dose implanted and annealed at 900 °C SiO<sub>2</sub> matrix can be seen in Fig. 2.5. It is clear that the formation of Ge nanocrystals has been completed at this temperature and SiO<sub>2</sub> matrix fully recovered. TEM microimage of Ge nanocrystals formed in this sample is shown in Fig. 2.6. A detailed discussion of this can be found in Ref. 11.

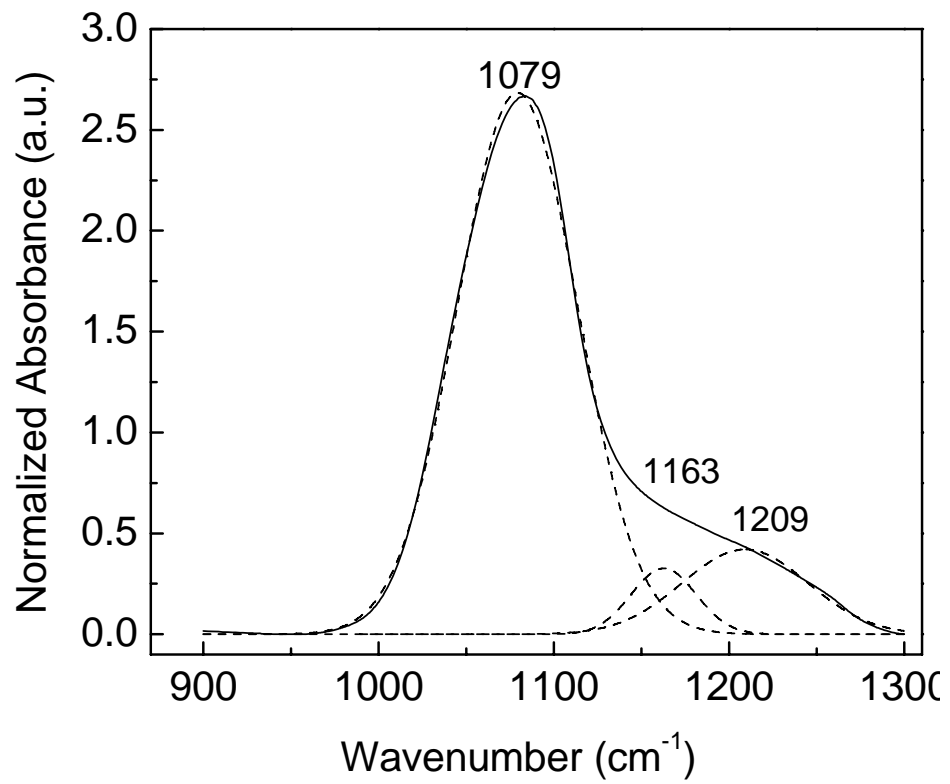


Fig. 2.5. The deconvolution of the Si-O-Si asymmetric stretching vibrational mode of SiO<sub>2</sub> implanted with a dose of  $1 \times 10^{17}$  <sup>74</sup>Ge /cm<sup>2</sup> and annealed at 900 °C

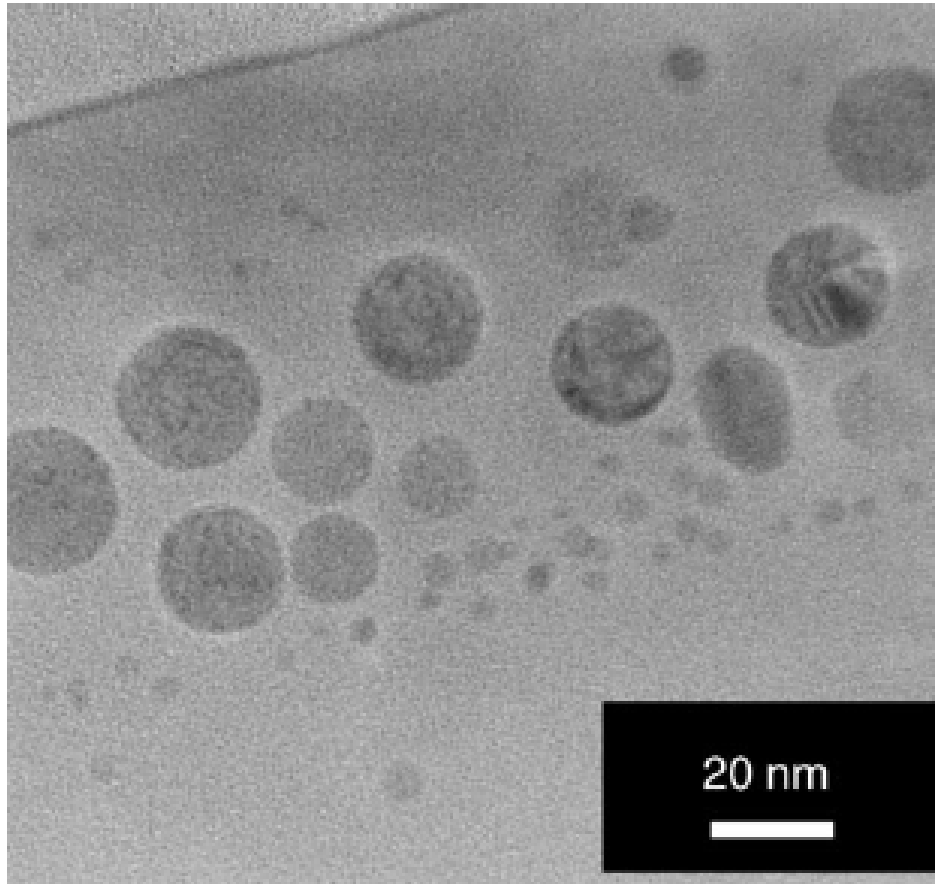


Fig. 2.6. TEM micro-image of the Ge nanocrystals formed by ion implantation in SiO<sub>2</sub> matrix after an annealing of 900 °C [22]

A detailed study has also been carried out for the deconvolution of <sup>28</sup>Si implanted SiO<sub>2</sub> matrix. Implanted samples were annealed for 800 °C, 900 °C, 1050 °C and 1200 °C and their FTIR spectra were deconvoluted between 875 and 1300 cm<sup>-1</sup>. The introduction of excess Si ions to the SiO<sub>2</sub> film during the implantation brings about an inhomogeneous SiO<sub>x</sub> film. The deconvolution of the above mentioned four peaks has been done, and the change in their integrated area and their peak positions with the annealing temperature are displayed in Fig. 2.7. While the integrated area of the Si-O-Si AS mode related to SiO<sub>2</sub> matrix increases, that of SiO<sub>x</sub> with x<2 related

mode decreases. This result clearly indicates the recovery of the matrix with increasing annealing temperature. However, the final value of the integrated absorbance band area for the sample annealed at 1200 °C is less than that of bulk SiO<sub>2</sub>, indicating the recovery of SiO<sub>2</sub> matrix has not been completed. In Fig. 2.7. it can be seen that while the peak position of the Si-O-Si AS mode related to SiO<sub>2</sub> matrix does not change, that of SiO<sub>x</sub> related mode moves to lower wavenumbers. It can be concluded that Si-O<sub>4</sub> and Si-Si<sub>3</sub>O structures are forming at the higher annealing temperature. This is in agreement with the result of Swart et. al where for SiO<sub>x</sub> structures Si rich areas become more Si rich and the oxygen rich areas become more oxygen rich during annealing [12]. This is expected for our samples, in which the SiO<sub>2</sub> matrix has been recovered and Si nanocrystals have been formed. TEM image of the sample implanted with  $1 \times 10^{17}$  Si/cm<sup>2</sup> and annealed at 1050 °C is shown in Fig. 2.8.

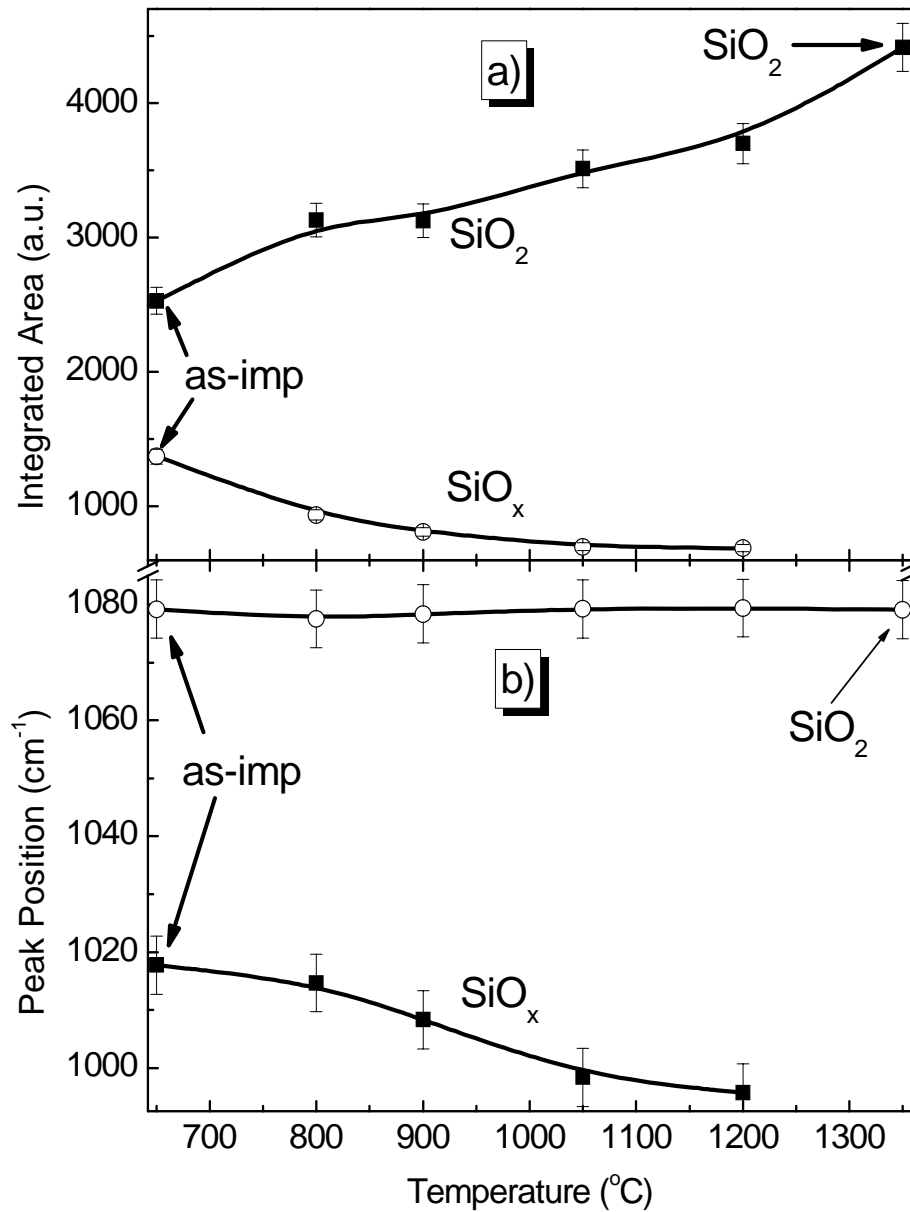


Fig. 2.7. The change in a) the integrated area and b) the peak position of Si-O-Si bond stretching for SiO<sub>x</sub> and SiO<sub>2</sub> with the annealing temperature for samples implanted with a dose of  $1 \times 10^{17}$  Si ions/cm<sup>2</sup>

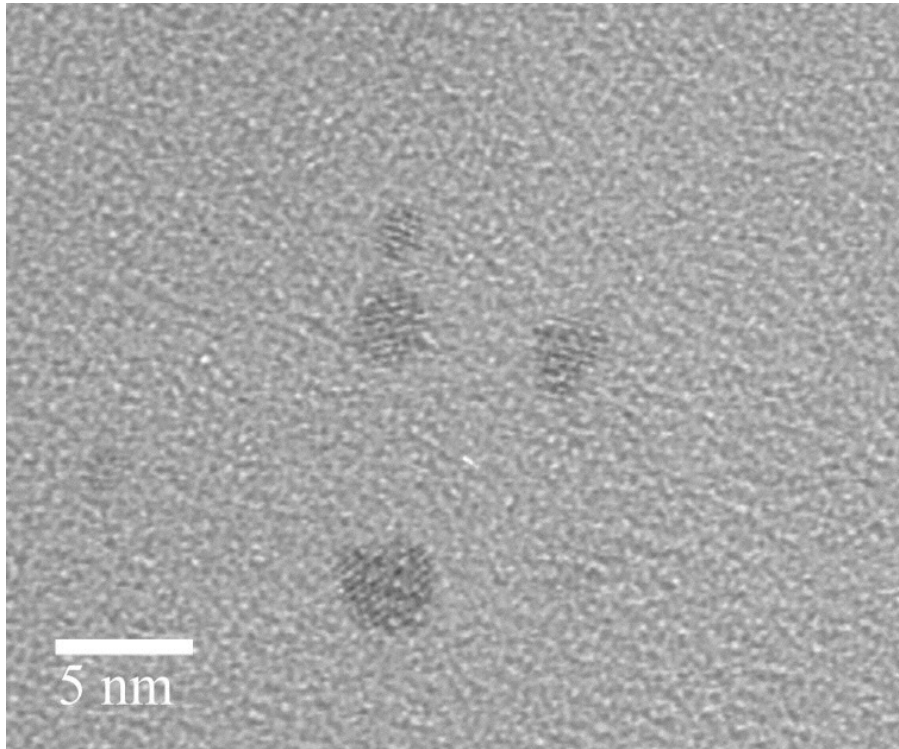


Fig. 2.8. TEM micro-image of sample implanted with  $1 \times 10^{17}$  Si/cm<sup>2</sup> and annealed at 1050 °C [23]

## 2.4 Conclusion

FTIR spectroscopy was employed to monitor the structural variations in SiO<sub>2</sub> matrix during the formation of Ge and Si nanocrystals prepared by ion implantation and annealing process. Ge implanted SiO<sub>2</sub> films complete the recovery at lower temperatures than that of Si implanted and the recovery of Si implanted films could not be completed even after 1200 °C, 2 h annealing. FTIR spectroscopy is used to show both the recovery process of the SiO<sub>2</sub> matrix and the formation of the Si rich SiO<sub>x</sub> bonds during the nanocrystal formation. The increase in the integrated area of Si-O-Si AS<sub>1</sub> mode is used as an evidence for the recovery of SiO<sub>2</sub> matrix and the shift at the peak position of Si-O-Si AS<sub>1</sub> mode for the SiO<sub>x</sub> matrix is an evidence for the increase in the Si-Si bonds.

## 2.5 References

1. James D. Ingle and Stanley R. Crouch, *Spectrochemical Analysis*, 1998, Prentice-Hall, Inc
2. Douglas A. Skoog and Donald M. West, *Principles of Instrumental Analysis*, 1971, Holt, Rinehart and Winston, Inc.
3. D. V. Tsu, G. Lucovsky, and B. N. Davidson, *Phys. Rev. B*, 40, 1795, 1989.
4. D. Nesheva, I. Bineva, Z. Levi, Z. Aneva, Ts. Merdzhanova, and J. C. Pivin, *Vacuum* 68, 1, 2003
5. N. Tomozeiu, J. J. van Hapert, E. E. van Faasen, W. Arnoldbik, A. M. Vredenberg, and F. H. P. M. Habraken, *J. Optoelec. Adv. Mater.*, 4, 513, 2002
6. Y. Liu, T. P. Chen, Y. Q. Fu, M. S. Tse, J. H. Hsieh, P. F. Ho, and Y. C. Liu, *J. Phys. D :Appl. Phys.*, 36, L97, 2003
7. V. Drinek, J. Pola, Z. Bastl, and J. Subrt, *J. Non-Cryst. Solids*, 288, 30, 2001.
8. I. Montero, L. Galan, O. Najmi, and J.M. Albella, *Phys. Rev. B*, 50, 4881, 1994.
9. P. Lange, *J. Appl. Phys.*, 66, 201, 1989.
10. M. Mondreanu, M. Gartner, E. Aperathitis, N. Tomozaiu, M. Androulidaki, D. Cristea, P. Hurley, *Physica E*, 16, 461, 2003.
11. U. Serincan, S. Yerci, M. Kulakci, and R. Turan, *Nucl. Instr. Methods B*,
12. H.C. Swart, E. D. van Hattum, W. M. Arnoldbik, and F. H. P. M. Habraken, *phys. Stat. Sol. (c)* 1, 2286, 2004.
13. L. X. Yi, J. Heitman, R. Scholz, and M. Zacharias, *Appl. Phys. Lett.*, 81, 4248, 2002.
14. U. Serincan, G. Aygun, and R. Turan, *J. Lumin*, 113, 229, 2005.
15. T. Z. Lu, M. Alexe, R. Scholz, V. Talalaev, R. J. Zhang, and M. Zacharias, *J. Appl. Phys.* 100, 014310, 2006.
16. E. Dehan, P. Temple-Bojer, R. Henda, J. J. Pedroviejo, and E. Scheid, *Thin Solid Films*, 266, 14, 1995.
17. K. T. Queeney, N. Herbots, J. M. Shaw, V. Atluri, and Y. J. Chabal, *Appl. Phys. Lett.*, 84, 493, 2004.
18. M. Trchova, J. Zemek, and K. Jurek, *J. Appl. Phys.*, 82, 3519, 1997.

19. M. Zacharias, T. Drusadau, A. Panckow, H. Freistedt, and B. Garke, *J. Non-cryst. Solids*, 169, 24, 1994.
20. M. J. F. Ziegler, J. P. Biersack, and U. Littmark, *the Stopping and Range of Ions in Solids* (Pergamon, New York, 1985).
21. S. Yerci, U. Serincan, M. Kulakci, F. Ay, A. Aydinli, and R. Turan, *Proc. of SEMINANO*, vol. 2, pp. 223, 2005.
22. U. Serincan, G. Kartopu, A. Guennes, T. G. Finstad, R. Turan, Y. Ekinici, and S. C. Bayliss, *Semicond. Sci. Technol.* 19, 247, 2004.
23. J. Mayandi, T.G. Finstad, S. Foss A. Thøgersen, U. Serincan and R. Turan, *Physica Scripta T126*, 77-80, 2006.

## CHAPTER 3

### CHARACTERIZATION OF NANOCRYSTALS USING RAMAN SPECTROSCOPY

#### 3.1 Introduction

When light is scattered from a molecule most photons are elastically scattered, called as Rayleigh scattering. However, a small fraction of photons (approximately 1 in  $10^7$  photons) is undergone an inelastic scattering due to a change in the elemental excitations of the probed material. The process leading to this inelastic scatter is the termed the Raman Effect after the discovery of the Indian physicist, C. V. Raman in 1928. Raman scattering can occur with a change in vibrational energy of a molecule. In other words, it can cause a creation (Stokes process) or annihilation (Anti-Stokes process) of a phonon [1].

The Raman event is simple and takes place in approximately  $10^{-14}$  seconds or less. However, the theory of Raman scattering is far from elementary. Both the group theory and high-order perturbation theory are required to explain the phenomenon properly. While, in classical physics, the interaction can be considered as a perturbation of the molecule's electric field, in quantum mechanics, the scattering is described as an excitation to a virtual state lower in energy than a real electronic transition with nearly coincident de-excitation and a change in vibrational energy. A representative energy band diagram of Raman scattering is given in Fig. 3.1 [2].

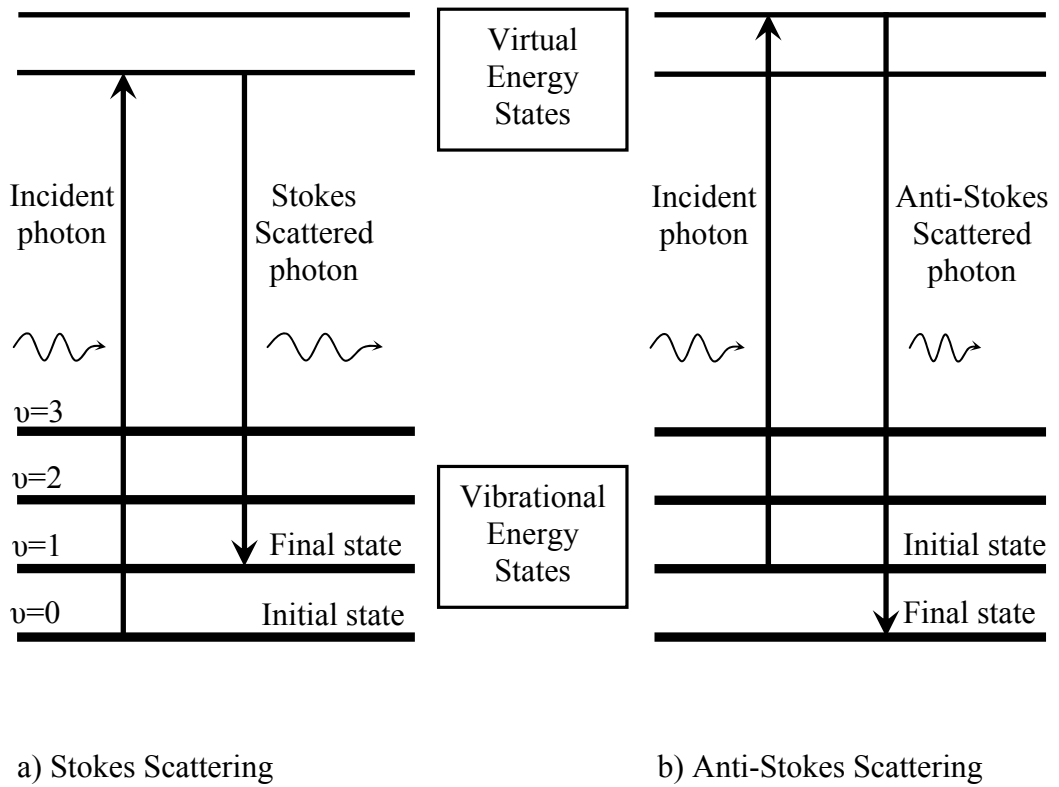


Fig. 3.1. Energy level diagram for Raman scattering a) Stokes b) Anti-Stokes

According to classical theory, Raman scattering can be formulized as follows [1];  
 In Raman experiment, an electric field of a laser beam is directed to a diatomic molecule. The fluctuating electric field with its strength of  $E$  can be represented as;

$$E = E_0 \cos 2\pi\nu_0 t, \quad (3.1)$$

where

$E_0$ : The electric field amplitude,

$\nu_0$ : The frequency of the laser.

The electric dipole moment of the molecule is;

$$P = \alpha E = \alpha E_0 \cos 2\pi\nu_0 t, \quad (3.2)$$

where

$\alpha$ : polarizability.

The nuclear displacement,  $q$ , for a molecule vibrating with a frequency of  $\nu_m$  is written as;

$$q = q_0 \cos 2\pi\nu_m t, \quad (3.3)$$

where

$q_0$ : the vibrational amplitude.

For small amplitude of vibration,  $\alpha$  is a linear function of  $q$ . Thus, it can be written as;

$$\alpha = \alpha_0 + \left(\frac{\partial\alpha}{\partial q}\right)_0 q_0 + \dots \quad (3.4)$$

$\alpha_0$ : the polarizability at equilibrium position.

Inserting the equation 3.4 and 3.3 into the equation 3.2, one can find the electric dipole moment as;

$$P = \alpha E_0 \cos 2\pi\nu_0 t \quad (3.5)$$

$$= \alpha_0 E_0 \cos 2\pi\nu_0 t + \left(\frac{\partial\alpha}{\partial q}\right)_0 q_0 E_0 \cos 2\pi\nu_0 t \quad (3.6)$$

$$= \alpha_0 E_0 \cos 2\pi\nu_0 t + \left(\frac{\partial\alpha}{\partial q}\right)_0 q_0 E_0 \cos 2\pi\nu_0 t \cos 2\pi\nu_m t \quad (3.7)$$

$$= \alpha_0 E_0 \cos 2\pi\nu_0 t + \frac{1}{2} \left(\frac{\partial\alpha}{\partial q}\right)_0 q_0 E_0 [\cos \{2\pi(\nu_0 + \nu_m)t\} + \cos \{2\pi(\nu_0 - \nu_m)t\}] \quad (3.8)$$

In the final expression, the first, second and third terms represent the Rayleigh, anti-stokes and stokes Raman scattering, respectively.

The difference in energy between the incident photon and the Raman scattered photon is equal to the energy of a vibration of the scattering molecule which is characteristic for various molecules. A plot of intensity of scattered light versus energy difference between incident and scattered photons is a Raman spectrum. Numerically, the Raman shift (in  $\text{cm}^{-1}$ ) can be calculated using Equation 1 [3].

$$\bar{\nu} = \frac{1}{\lambda_{incident}} - \frac{1}{\lambda_{scattered}} \quad (3.9)$$

where,

$\lambda_{\text{incident}}$  and  $\lambda_{\text{scattered}}$  are the wavelength (in cm) of incident and scattered photons, respectively.

The energy and the shift in a Raman spectrum are mainly defined by the molecular and environmental parameter such as atomic mass, bond order, molecular substituents, and molecular geometry. For example, the temperature of the area exposed by laser beam can be calculated using the ratio of the intensities of stokes to anti-stokes shifts [1, 4].

The relation can be described as follows,

$$\frac{I_S}{I_{AS}} = \frac{(\nu_0 - \nu_m)^4}{(\nu_0 + \nu_m)^4} \exp(hc \nu_m / kT) \quad (3.10)$$

The relation can be rewritten as follows to find the temperature directly,

$$T = \frac{-1.43879 \otimes \nu_m}{\ln\left(\frac{I_S}{I_{AS}}\right) + 4 \ln\left(\frac{\nu_0 - \nu_m}{\nu_0 + \nu_m}\right)^4} \quad (3.11)$$

where

$I_S$ : the intensity of stokes Raman shift

$I_{AS}$ : the intensity of anti-stokes Raman shift

Surface-enhanced Raman scattering (SERS) and resonance-enhanced Raman scattering (RERS) are two methods improved to intensify the Raman scattering at the surface and at a particular wavelength, respectively. SERS method based on the enhancement of the electromagnetic field produced at the surface of the metal. Silver or gold colloids are widely used for enhancement. The intensity of some Raman active vibrations increases by a factor of  $10^2$ - $10^6$  under SERS conditions. Moreover, RERS is observed when the wavelength of the exciting laser coincides with the electronic spectrum of a molecule.

Raman scattering provides a fast and nondestructive method to characterize nanostructures. From the shape and the peak position of the first order Raman scattering band following properties of nanocrystals can be investigated.

- i) the size variations (i.e. estimation of the size of the nanocrystals)
- ii) the phase changes (i.e. estimation of amorphous to crystalline ratio),
- iii) the evolution of the stress on nanocrystals (i.e. estimation of the stress on the nanocrystals).
- iv) the temperature variations on nanocrystals (i.e. calculation of temperature on nanocrystals)

i) estimation of the size of the nanocrystals: Conservation of phonon momentum  $q$  in crystalline structures results in a narrow Raman line in spectrum. However, conservation rule does not apply to amorphous structures due to lack of long range order. On the other hand, in nanocrystals, phonons are localized in small crystallites and momentum is no longer well defined according to the uncertainty principle enabling phonons with  $q \neq 0$  to contribute to the Raman spectra. Thus, an asymmetric broadening and a blueshift are observed in the first order Raman spectra. Furthermore, in classical sense, the broadening of the peak is due to the absence of long range order which destroys the full translation symmetry of the material. Raman scattering deals with the phonons only at the center of the Brillouin zone. However, in nanocrystals, the phonons near to interface of nanocrystals can participate in Raman scattering. These phonons have lower energies compared to the ones at the center of the Brillouin zone. Thus, the low-frequency tail of the Raman band is supposed to stretch much more significantly than the high frequency tail. The Raman lineshape of nanocrystals can be estimated using the phonon confinement model [5-12]

According to this model, the first-order Raman spectrum  $I(\omega)$  is given by

$$I(\omega) = \int_q \frac{|C(0, q)|^2}{[(\omega - \omega(q))^2 + (\Gamma_0/2)^2]} d^3 q \quad (3.12)$$

where,

$I(\omega)$ : the intensity of the Raman spectrum,

$\omega(q)$ : the phonon dispersion of the bulk material,

$\Gamma_0$ : the natural Raman line width of bulk material,

$C(0,q)$ : the Fourier-coefficient of the phonon confinement function.

Equation 3.12 can be rewritten for Si nanocrystals by assuming

$|C(0,q)|^2 = \exp(-q^2 L^2 / 16\pi^2)$  and  $\omega^2(q) = 1.714 \times 10^5 + 1 \times 10^5 \cos(\pi q/2)$  as

$$I(\omega) = \int_0^1 \frac{\exp(-q^2 L^2 / 4a^2)}{[(\omega - \omega(q))^2 + (\Gamma_0/2)^2]} d^3 q \quad (3.13)$$

Here,  $q$  is expressed in units of  $2\pi/a$ ,  $a$  is the lattice constant (0.357 nm) of Si,  $\Gamma_0$  is approximately  $4 \text{ cm}^{-1}$  for our system configuration. Fig. 3.2 represents the calculated Raman spectra for various sizes of Si nanocrystals using a similar expression given in equation 3.13 [12].

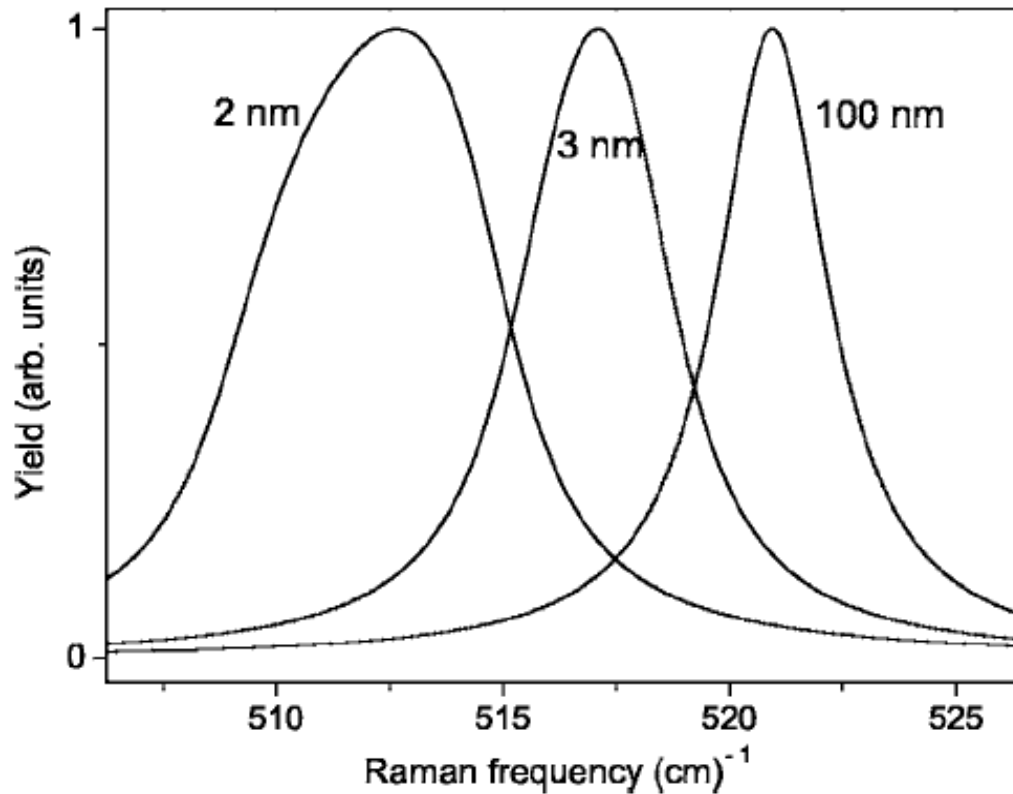


Fig. 3.2. First order Raman scattering of crystalline Si and nanocrystalline Si with various sizes (taken from ref. 12)

ii) *estimation of amorphous to crystalline ratio*: During the formation of the nanocrystals by annealing Si or Ge rich oxides, amorphous nanoclusters forms initially. These clusters crystallize into nanocrystals gradually. It is observed that the optical and electrical properties these two phases are quite different [13, 14]. Therefore, quantification of crystalline volume fraction is significant in some application. The fraction can be calculated from the integrated intensities of the amorphous to crystalline peaks,  $I_a$  and  $I_c$ , respectively [15].

$$X_c = \frac{I_c}{I_c + \rho I_a} \quad (3.14)$$

where  $\rho$  is the ratio of the Raman efficiencies for crystalline to amorphous Si, and it can be described as

$$\rho(L) = 0.1 + \exp(-L/250) \quad (3.15)$$

where  $L$  (in Å) is the nanocrystal size. However, this relation is only valid when  $L > 3$  nm [16].

iii) *estimation of the stress on the nanocrystals*: The phonon confinement model predicts a blueshift and a broadening in the first order Raman signal. However, in order to describe Raman process in nanocrystals fully, the effects of stress on nanocrystals should be taken into account. The tensile and compressive stresses cause a redshift (or up-shift) and blueshift (down-shift), respectively. The amount stress can be estimated from the stress induced wavenumber shift,  $\Delta w_s$  [17, 18]:

$$\sigma \text{ (MPa)} \approx \Delta w_s \text{ (cm}^{-1}\text{)} \quad (3.16)$$

iv) *calculation of absolute temperature on/around nanocrystals*: As it is discussed before the calculation of temperature at target area can be calculated for both bulk and nanocrystalline samples. It is known that the melting temperatures for nanocrystals are lower than their bulk values. Therefore the calculation of temperature at projected area is especially significant for applications such as laser induced crystallization [4]. On the other hand, during the Raman measurement, nanoclusters can be transformed to crystalline form if the laser power is high which is generally not desired. One can calculate the temperature at projected range using equation 3.10 or 3.11.

### 3.2 Instrumentation

Sir C. V. Raman used filtered sunlight as a monochromatic source, a colored filter as a monochromator, and a human eye as detector [19]. Since the intensity of Raman scattered light is very low, a high power monochromatic source is required. Therefore, the technique became widely used and commercialized after the invention of laser. In Fig. 3.3, a representative setup, similar to the one used in this

work, for Raman spectroscopy measurement is shown. While, He-Ne (633 nm), Ar<sup>+</sup> (488 nm and 514 nm) and Nd:YAG (532 nm) lasers are widely chosen as monochromatic source, other sources operating in ultra violet (UV), visible (VIS) and near infrared (NIR) ranges are available. Charge coupled devices (CCD), photomultiplier tubes (PMT) or semiconductor detector are widely used for light detection. Among these, CCD performs in multichannel image acquisition mode, which shorten the time required to readout the spectrum, therefore of particular interest. Raman spectrometer can be either dispersive or nondispersive. While dispersive systems consist of grating or prism to separate the colors, nondispersive systems include Michelson interferometer for this purpose and called as Fourier transform Raman (FT-Raman) spectrometer. Raman spectrometer can be improved with various optical compounds such as notch filter, confocal hole, microscope, and polarizer. Notch filter is a narrow band filter used to block the Rayleigh scattering to protect the detector, mainly. Confocal hole is useful to investigate the Raman response of the layers or deep of the samples at normal incidence. The lateral resolution of the method can be increased by attaching suitable microscope lenses. These systems are called as micro-Raman spectrometers. As the Raman scattering is a polarization dependent phenomenon, some signals can be blocked while some others highlighted using a polarizer

Raman measurements, performed in this dissertation, were employed in backscattering geometry at room temperature using 632.8 nm as the light source of a confocal micro-Raman (HR800, Jobin Yvon) system, located in the Department of Chemistry at METU, attached with Olympus microanalysis unit and a liquid-nitrogen-cooled CDD camera providing a resolution of  $\sim 1 \text{ cm}^{-1}$ .

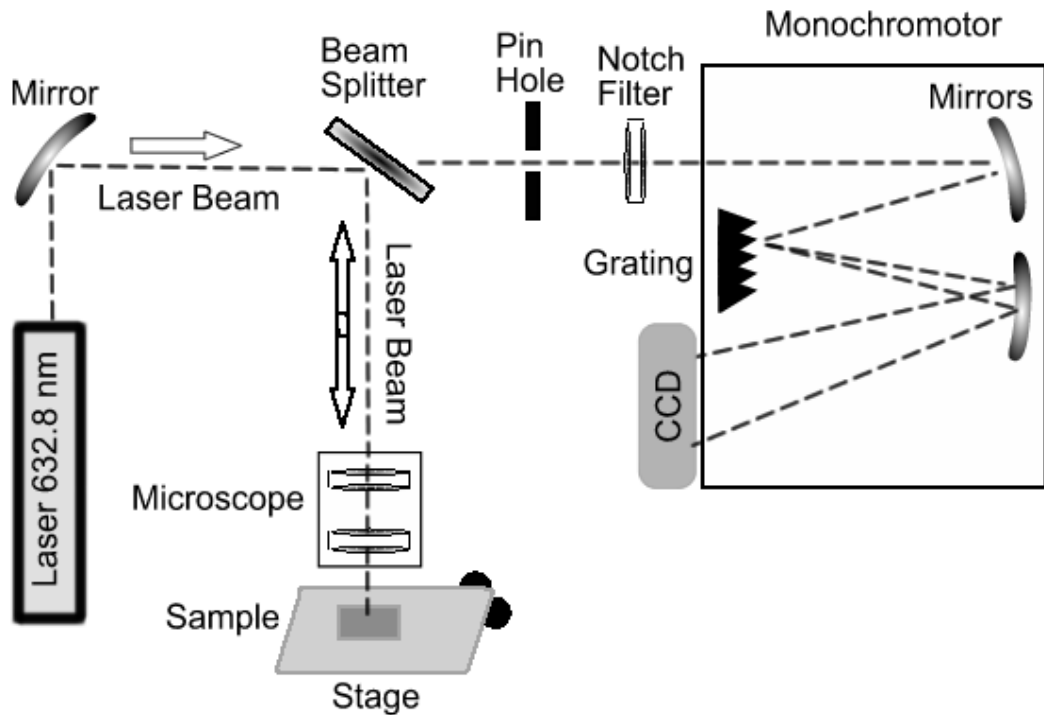


Fig. 3.3. A representative confocal micro-Raman spectrometer setup

### 3.3 Probing Nanostructures with Raman Spectroscopy

#### 3.3.1 Si Nanocrystals in SiO<sub>2</sub> Matrix Formed by Ion Implantation

Observation of Si nanocrystals embedded in SiO<sub>2</sub> grown on Si substrate using Raman spectroscopy is a challenging issue. The TO Raman signals due to nanocrystals intermix in that of Si substrate. Although Welner et. al. observed the Raman signals of Si nanocrystals with the existence of Si substrate under 10 nm of oxide [20], samples containing high density of Si and annealed at lower temperatures can only be observed using universal Raman systems [21]. Raman spectra of thermally grown 250 nm thick SiO<sub>2</sub> samples grown on Si substrate samples implanted with  $2 \times 10^{17}$  Si/cm<sup>2</sup> and annealed at 1100 °C are given in Fig 3.4.

As-implanted sample shows transverse acoustic (TA), longitudinal optical (LO) and transverse optical TO peaks around 150, 301, and 488  $\text{cm}^{-1}$ , respectively. The LO peak and TO peak seen in Fig. 3.4 at 301 and 521  $\text{cm}^{-1}$  are generated by the crystalline substrate. Upon crystallization, the peaks around 150 and 488  $\text{cm}^{-1}$  disappear and the intensity of the peak at 301  $\text{cm}^{-1}$  increases. Lower absorption cross section of Si nanocrystals compared to the amorphous Si enables more light to reach to the substrate which is responsible for the observed Si Raman band seen at 301  $\text{cm}^{-1}$ . The red shift in the peak around 488  $\text{cm}^{-1}$  makes it to disappear within the signal coming from the substrate. It should be noted that no peak either TA or TO were detected for samples implanted with  $1 \times 10^{17}$   $\text{Si}/\text{cm}^2$ .

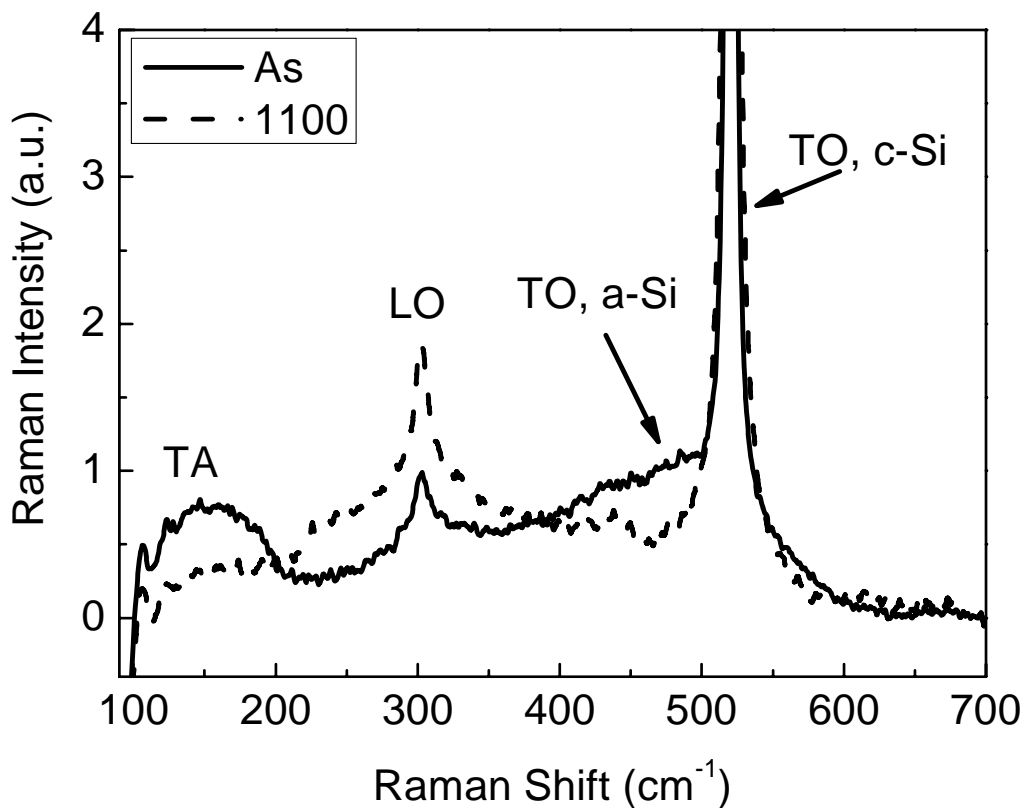


Fig. 3.4. Raman spectra for samples implanted with  $2 \times 10^{17}$   $\text{Si}/\text{cm}^2$  and annealed at 1100  $^{\circ}\text{C}$

### 3.3.2 Ge Nanocrystals in SiO<sub>2</sub> Matrix Formed by Ion Implantation

In the previous section, the challenges in characterization of Si nanocrystals formed in SiO<sub>2</sub> grown on Si substrate with Raman spectroscopy were discussed. Similar difficulties are present for the Ge nanocrystals. The TO peak for Ge and LO peak for Si located circa 300 cm<sup>-1</sup>. Therefore, these two peaks can easily coincide for especially small Ge nanocrystals when they are under compressive stress. In Fig. 3.5, Raman spectra of thermally grown 250 nm thick SiO<sub>2</sub> samples implanted with 1x10<sup>17</sup> Ge/cm<sup>2</sup> and annealed at temperatures at 800, 900 and 1100 °C are given. The sample underwent no heat treatment exhibits amorphous Ge TO signal around 290 and Si LO signal at 300 cm<sup>-1</sup>. While the latter peak does not shift the former one shifts to 293 cm<sup>-1</sup> with an annealing at 800 °C. As discussed previously, the Si LO peak is suppressed with increasing annealing temperatures. The intensity of Ge TO peak increases and its position shifts to 296 and 295 cm<sup>-1</sup> after annealing at 900 and 1100 °C, respectively. According to the phonon confinement model, one can expect to observe higher wavenumber shift for the sample annealed at lower temperatures; however, this rule does not apply in the existence of stress. Here, it can be mentioned that the compressive stress on Ge nanocrystals formed at 900 °C is higher than that of Ge nanocrystals formed at 1100 °C.

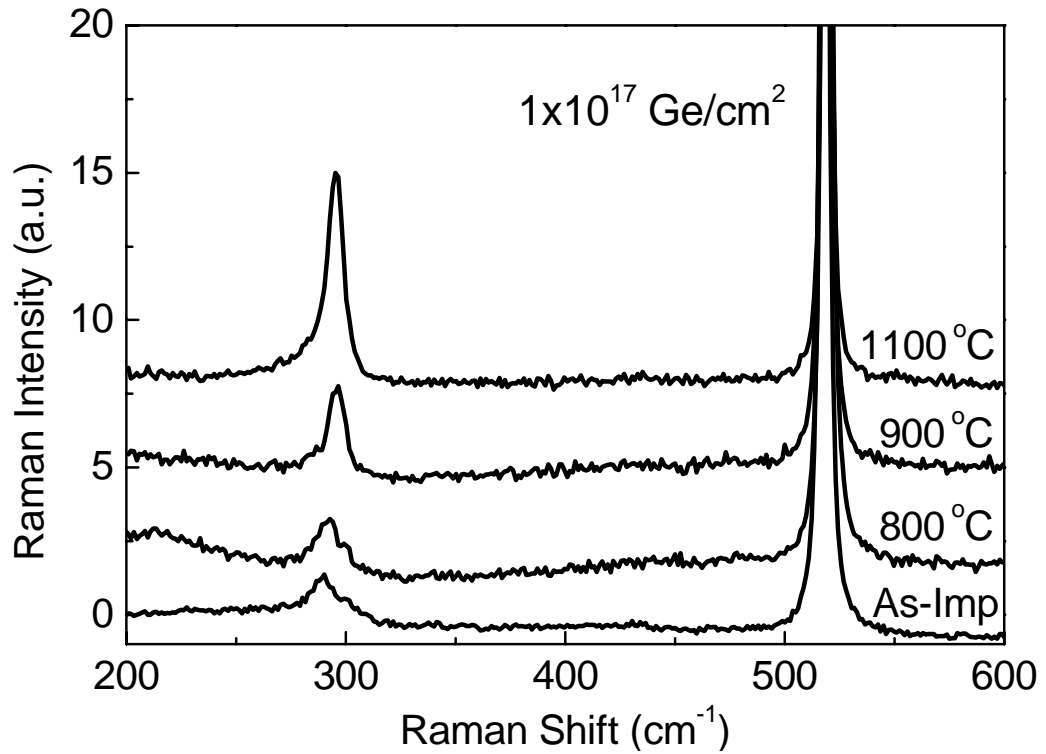


Fig. 3.5. Raman spectra of samples implanted with  $1 \times 10^{17}$  Ge/cm<sup>2</sup> and annealed at temperatures at 800, 900 and 1100 °C

### 3.3.3 Si nanocrystals in Al<sub>2</sub>O<sub>3</sub> Matrix Formed by Ion Implantation

C-plane oriented  $\alpha$ -Al<sub>2</sub>O<sub>3</sub> substrates were implanted with 100-keV <sup>28</sup>Si<sup>+</sup> ions at a dose of  $1 \times 10^{16}$ ,  $1 \times 10^{17}$  and  $2 \times 10^{17}$  Si/cm<sup>2</sup>, and annealed at 600, 700, 800, 900 and 1100°C in N<sub>2</sub> ambient for 2 h to induce Si nanocrystal formation. The projected range (Rp) of the Si ions was calculated as 81 nm using TRIM software.

Raman spectra of as-implanted samples are given in Figure 3.6. The peaks at around 418, 577 and 750 cm<sup>-1</sup> are from the crystalline host matrix. The intensity of these peaks decreases with increasing doses because of partial amorphization of the matrix. While no Raman signals for Si-Si bonds were observed from the sample

with the dose of  $2 \times 10^{16}$  Si/cm<sup>2</sup>, Raman signals typical for amorphous Si was detected in the sample with the doses of  $1 \times 10^{17}$  and  $2 \times 10^{17}$  Si/cm<sup>2</sup> [22]. The bands recorded from higher dose implanted samples are described as transverse acoustic (TA) band around 150 cm<sup>-1</sup>, transverse optical (TO) band around 480 cm<sup>-1</sup> and mixed acoustic-optical band around 310 cm<sup>-1</sup>. One could safely conclude that implantation with the dose of  $2 \times 10^{16}$  Si/cm<sup>2</sup> is not sufficient to generate amorphous Si clusters detectable with Raman spectroscopy (Fig. 3.6) and XRD. Annealing at 1100°C did not yield any Si nanocrystal formation in this sample either. The atomic percentage Si concentration for this fluence at peak position of the Si distribution is estimated to be 2.6% with TRIM codes.

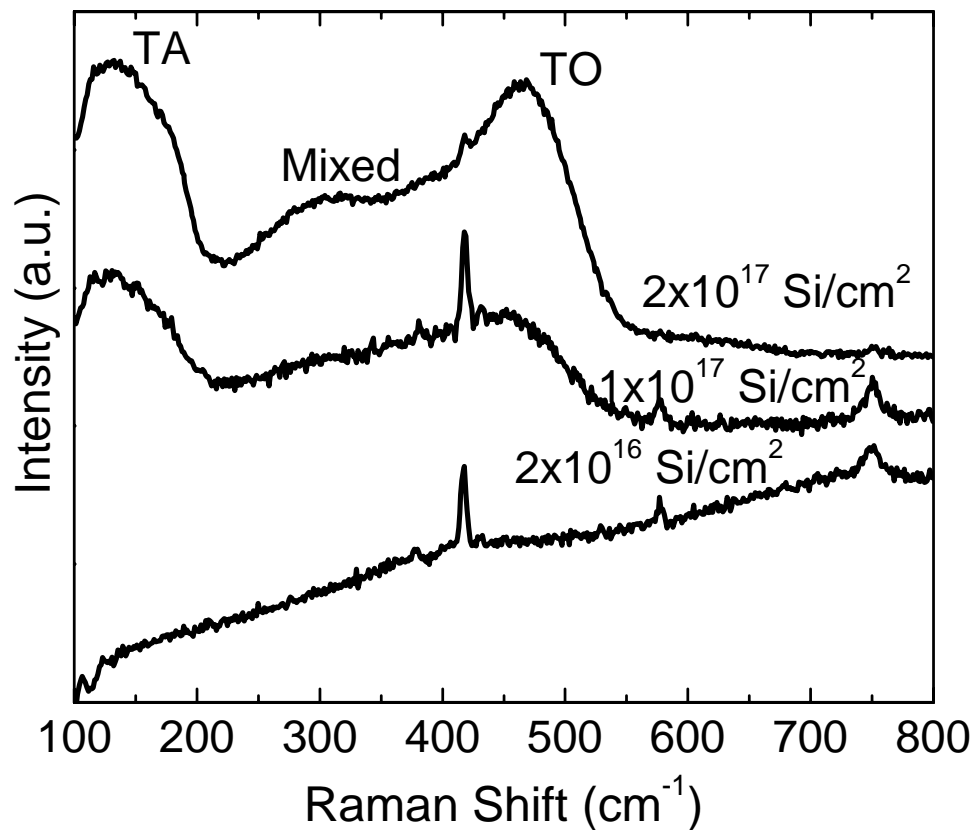


Fig. 3.6. Raman spectra of  $\alpha$ -Al<sub>2</sub>O<sub>3</sub> implanted with the doses of  $2 \times 10^{16}$ ,  $1 \times 10^{17}$  and  $2 \times 10^{17}$  Si/cm<sup>2</sup>

Raman spectroscopy clearly demonstrates the formation and the evolution of Si nanocrystals in the Al<sub>2</sub>O<sub>3</sub> matrix as a function of annealing temperature as shown in Fig. 3.7. The evolution of the Si-Si bonds, which shows the transformation from the amorphous phase to crystalline phase, can be observed from the variation of the Raman peaks seen at 150 and 310 cm<sup>-1</sup> and 480 cm<sup>-1</sup> with the annealing temperature (Fig. 3.7). The bands measured at 150, 310 cm<sup>-1</sup> from the samples with high dose implantation diminish with increasing annealing temperatures and disappear almost completely after 1100 °C 2 h annealing. We see that amorphous Si clusters formed in the as-implanted samples transforms into crystalline Si structures with a more intense and narrow Raman signal as the annealing temperature increases. As is also observed by XRD, both the size and the number of Si nanocrystals increase with the increasing annealing temperature and the dose. The evolution of the TO band of Si nanocrystals is commonly considered as an indicator of crystallinity in Si structures. While amorphous Si has a broad TO band around 480 cm<sup>-1</sup>, bulk Si has a sharp TO band with a natural linewidth of approximately 3 cm<sup>-1</sup> around 521 cm<sup>-1</sup> at room temperature. Moreover, it is known that this band for nanocrystalline Si shows a broadening and a shift to lower wavenumbers due to the phonon confinement effect [5-12, 23]. A qualitative comparison of the Raman signals measured for different doses and annealing temperatures indicates that while the nanocrystal formation starts at 800°C for the sample with a dose of 2x10<sup>17</sup> Si/cm<sup>2</sup>, it begins at around 900°C for the sample with a dose of 1x10<sup>17</sup> Si/cm<sup>2</sup>.

It was reported that the compressive stress can cause a shift to higher wavenumbers, acting in the opposite direction to the phonon confinement effect [5-12, 23]. The competition between the two mechanisms determines the position of the peak. Therefore, the methods, developed for the size estimation of the Si nanocrystals by using the shift and the broadening of Si TO Raman signals, is questionable in the case of large stress as in the present case [6, 18, 24]. Calculation of the size and the stress requires a separation between both parts from the Raman shift. The magnitude of the stress can be estimated from equation 3.16. In this calculation, the Raman shift due to the phonon confinement effect was first considered using results

established by Campbell and Fauchet [6], who calculated the relationship between the Raman shift and the size of the unstressed spherical nanocrystals using Gaussian a weighting function. Following to this calculation, the stress induced wavenumber shifts were found by subtracting these values from the corresponding experimental wavenumber values. The calculated approximate magnitudes of the stress were given in Table 3.1. It seems that the amount of stress is larger on the smaller nanocrystals formed at lower temperatures and it reaches almost a constant value when the nanocrystal formation process is completed.

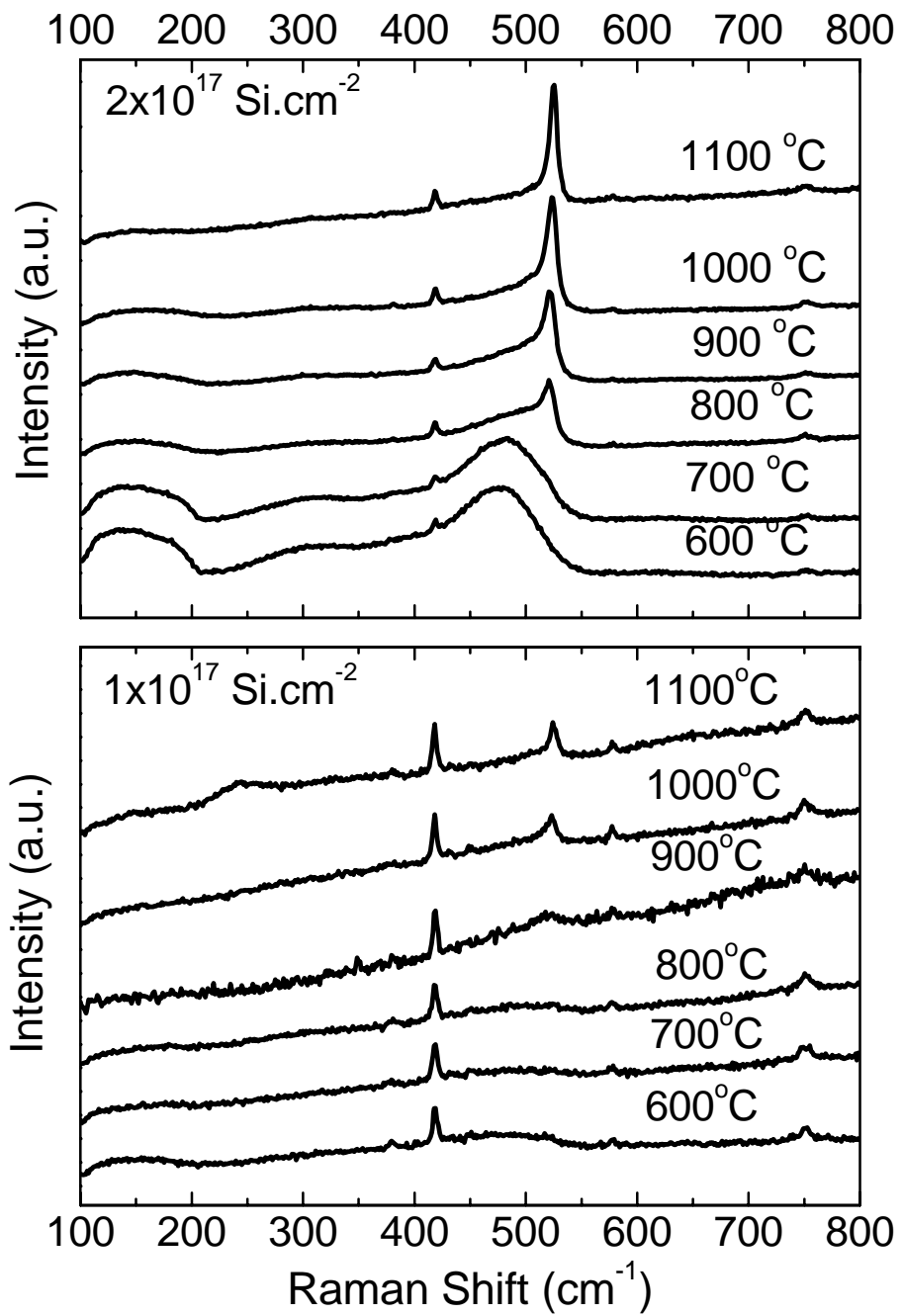


Fig. 3.7. The evolution of Raman signal for the doses of  $1 \times 10^{17}$  and  $2 \times 10^{17}$  Si/cm<sup>2</sup> implanted samples with annealing temperature

Formation of nanocrystals is a self assembly process. During the annealing process, first amorphous nanoclusters then nanocrystals form. The transition between amorphous to crystalline is not discrete. Therefore, a nanocrystal should be considered with its volume fraction of amorphous to crystalline phases. This fraction can be estimated using equations 3.14 and 3.15. The calculated volume fractions for various annealing temperatures of samples implanted with  $2 \times 10^{17}$  Si/cm<sup>2</sup> are given in Table 3.1. It is clear that the crystalline ratio increases with annealing temperature.

Table 3.1. The calculated crystalline ratio and the stress values of nanocrystals produced by different doses and annealing temperatures

dose	annealing temperature (°C)	Stress (MPa)	% crystalline to amorphous
$1 \times 10^{17}$	800	-	-
	900	-	-
	1000	2.20	-
	1100	1.66	-
$2 \times 10^{17}$	800	-	40.2
	900	2.57	48.3
	1000	1.73	75.0
	1100	1.71	89.1

One can consider that the Raman upshift can be related with the coalescence of Si nanocrystals under laser illumination applied during the measurement. However, it is calculated using the ratio of stokes and anti-stokes Raman line intensities that the

temperature during experiment within the samples was around 315.5 K (Fig. 3.8) which is far below the melting temperature of Si nanocrystals [4]. This result is expected when the low laser power and the transparency of sapphire samples are considered.

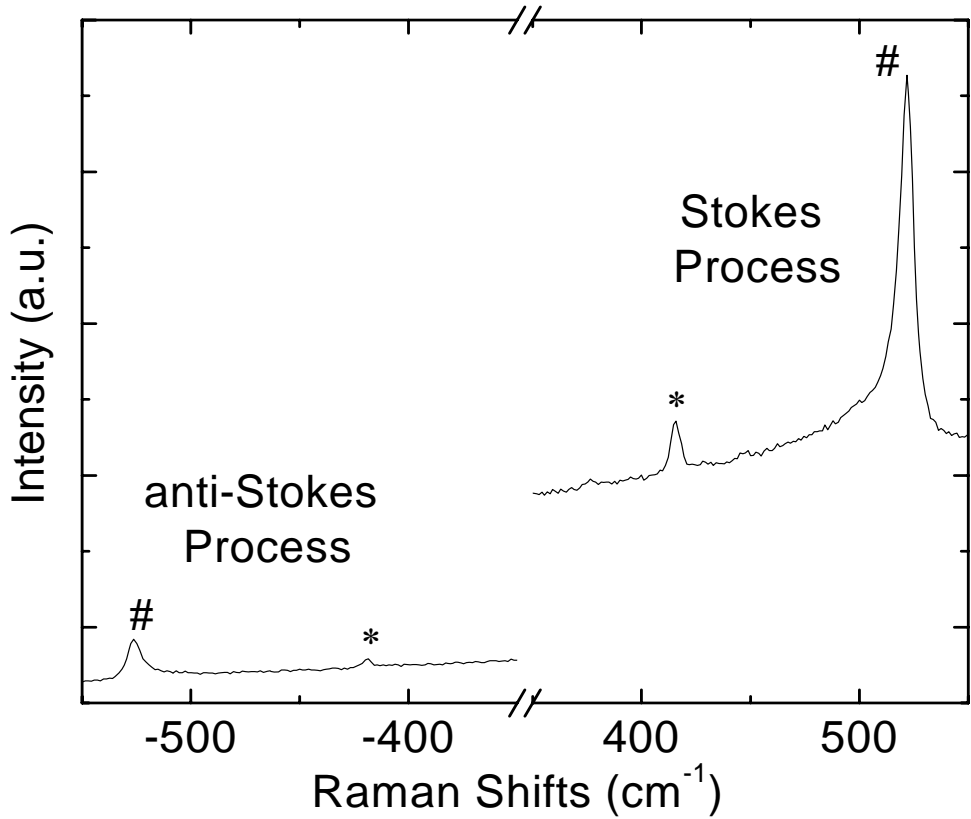


Fig. 3.8. The difference between Stokes and anti-Stokes shifts of a Raman spectrum at room temperature (“\*” shows the Silicon peak and “#” indicates the Al<sub>2</sub>O<sub>3</sub> peak)

### 3.3.4 Ge nanocrystals in Al<sub>2</sub>O<sub>3</sub> Matrix Formed by Ion Implantation

C-plane oriented  $\alpha$ -Al<sub>2</sub>O<sub>3</sub> substrates were implanted using 100-keV <sup>74</sup>Ge ions at doses of  $5 \times 10^{16}$  and  $1 \times 10^{17}$  Ge ions/cm<sup>2</sup>. The samples were subsequently annealed at temperatures ranging between 500 and 800 °C in vacuum for 1 h to induce Ge nanocrystal formation.

Raman spectra of samples implanted with doses of  $5 \times 10^{16}$  Ge ions/cm<sup>2</sup> and  $1 \times 10^{17}$  Ge ions/cm<sup>2</sup> and those of the samples annealed at 600 °C are shown in Fig. 3.9. The observed features of the as-implanted samples correspond to typical amorphous Ge peaks around 170 cm<sup>-1</sup> and 260 cm<sup>-1</sup> originating from the LA and TO bands, respectively [25]. The peaks at around 418, 577 and 750 cm<sup>-1</sup> are due to the crystalline host matrix. Their intensities are higher for the sample implanted with lower dose, indicating the heavier amorphization for the sample implanted with higher dose. Upon annealing at 600 °C, the LA band disappeared almost completely from the spectra and the TO band was shifted towards 300 cm<sup>-1</sup> (Fig. 3.9) which is typically attributed to the Raman peak position of bulk-Ge at room temperature. The intensity of the TO peak is higher for the samples annealed at same temperatures and implanted with  $1 \times 10^{17}$  Ge ions/cm<sup>2</sup> than those of the samples implanted with  $5 \times 10^{16}$  Ge ions/cm<sup>2</sup>. The intensity of the band increases with annealing temperature as shown in Fig. 3.10. From these results, we conclude that the size of the nanocrystals increase in samples with higher implantation dose and annealing temperatures as expected. On the other hand, as discussed in part 3.2, Raman signals for the sample implanted with a dose of  $5 \times 10^{16}$  Ge ions/cm<sup>2</sup> and subsequently annealed at 800 °C are enhanced significantly compared to those annealed at 700 °C. This result is in further agreement with XRD and TEM analysis of the sample annealed at 800 °C, where the size of the nanocrystals is found to increase abruptly.

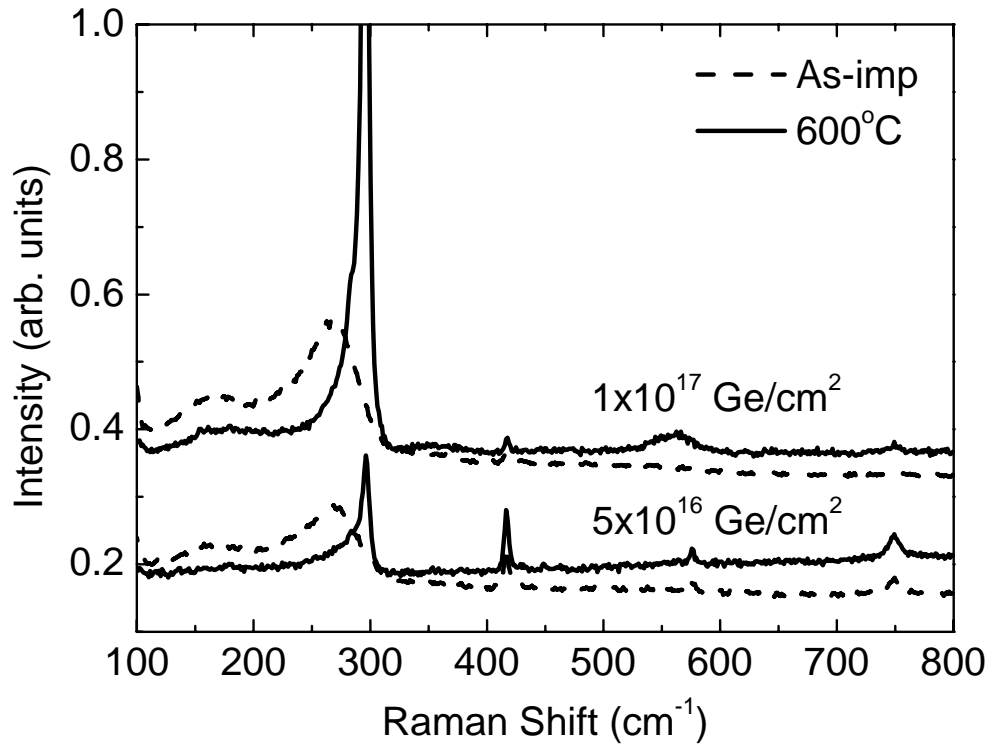


Fig. 3.9. Raman spectra of the samples implanted with doses of  $5 \times 10^{16}$  Ge ions/cm<sup>2</sup> and  $1 \times 10^{17}$  Ge ions/cm<sup>2</sup> and annealed samples at 600 °C

The shift in the Raman position of Ge nanocrystals with respect to bulk Ge ( $\sim 300$  cm<sup>-1</sup>) is dominated by three mechanisms; isotopic composition, phonon confinement and stress. The natural Ge has 5 different isotopes which generate the Raman signal commonly observed for bulk Ge. In the case of ion implantation, one of the Ge isotopes, which is the one with largest proportion (<sup>74</sup>Ge) is used for the implantation. This leads to isotopic composition of the Ge within the matrix. A red shift, approximately 3 cm<sup>-1</sup> is estimated in the peak position of the Raman signal of the isotopic <sup>74</sup>Ge with respect to natural bulk Ge [26]. Moreover, it is well-known that the TO band for nanocrystalline Ge shows a broadening in FWHM and a shift

to lower wavenumbers due to the phonon confinement effect [5-12, 18, 23]. According to the standard phonon confinement model using Gaussian weighting function, which is commonly accepted, nanocrystals with diameters of 15 nm and 5 nm undergo down shifts of approximately 1 and 4  $\text{cm}^{-1}$ , respectively [6, 26]. When the effects of isotropic composition and phonon confinement on Raman shift are considered, one might expect the Raman position of large and small nanocrystals as to be  $\sim 296 \text{ cm}^{-1}$  and  $\leq 293 \text{ cm}^{-1}$ , respectively. On the other hand, it is known that the stress on nanocrystals can create either down-shift due to tensile stress or up-shift due to compressive stress in Raman spectrum [17, 18, 23]. Extensive stress can cause lattice relaxation with high density of defects in and around Ge nanocrystals. Note that the encapsulated Ge nanocrystals have a lattice constant around 5.65 Å while the surrounding matrix has either lattice constants of 4.758 Å and 12.991 Å for  $\alpha\text{-Al}_2\text{O}_3$  or 7.90 Å for  $\gamma\text{-Al}_2\text{O}_3$ . Therefore, it is reasonable to assign the main peak at  $297 \text{ cm}^{-1}$  to scattering from large nanocrystals and the bump (highlighted with arrows) at around  $284 \text{ cm}^{-1}$  to scattering from small nanocrystals. In addition, it is likely that while small nanocrystals are under tensile stress large nanocrystals are under compressive stress. On the other hand, the lack of shift in Raman signal with annealing temperature can be due to the relaxation of large Ge nanocrystals as they can not accommodate the large amount of stress accumulated with increased nanocrystal size.

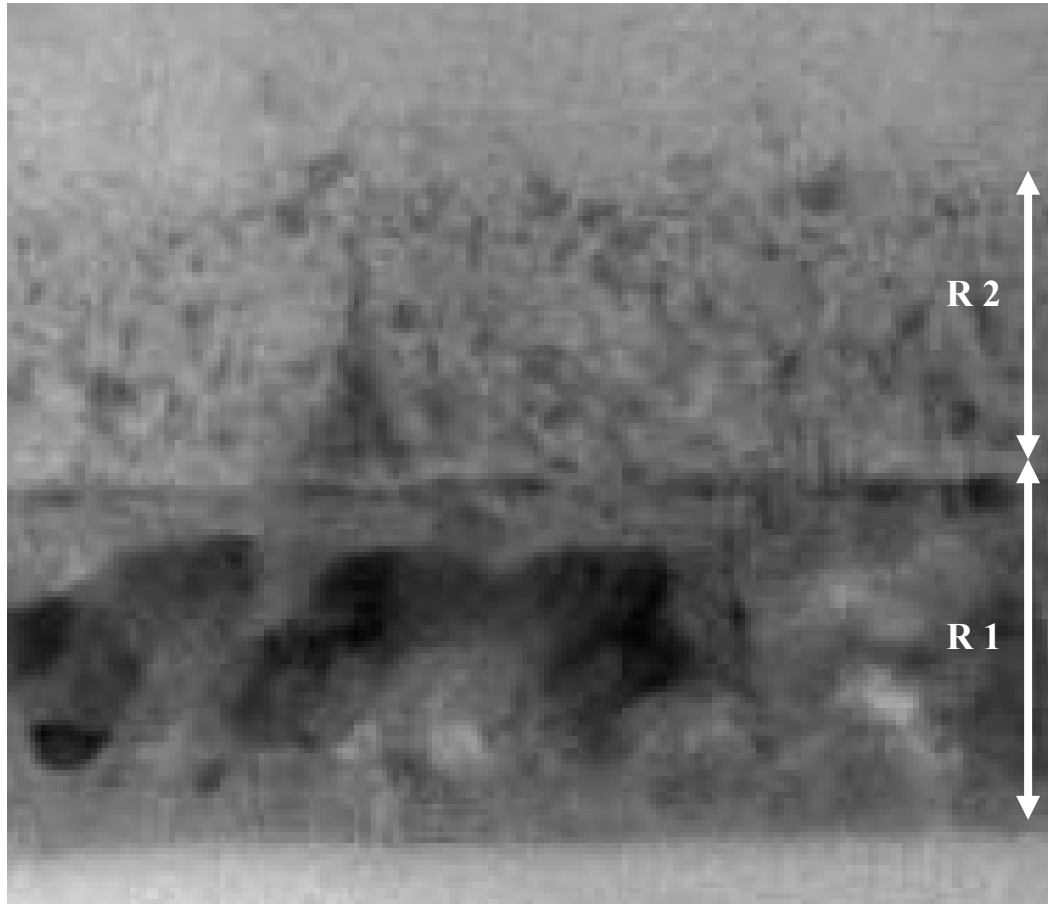


Fig. 3.10. TEM micrograph for a sample implanted with a dose of  $1 \times 10^{17}$  Ge ions/cm<sup>2</sup> subsequently annealed at and c) 800 °C. The arrows show the separate areas which includes Ge nanocrystals having different size distributions

Bi-modal shape in size distribution of Ge nanocrystals in Al<sub>2</sub>O<sub>3</sub> was observed using HRTEM [27, 28]. In Fig 3.11 shows the TEM micrograph of sapphire sample implanted with  $1 \times 10^{17}$  Ge/cm<sup>2</sup> and subsequently annealed at 800 °C. Nanocrystals with mean diameter of 15 and 4 nm were observed in region R1 and R2, respectively.

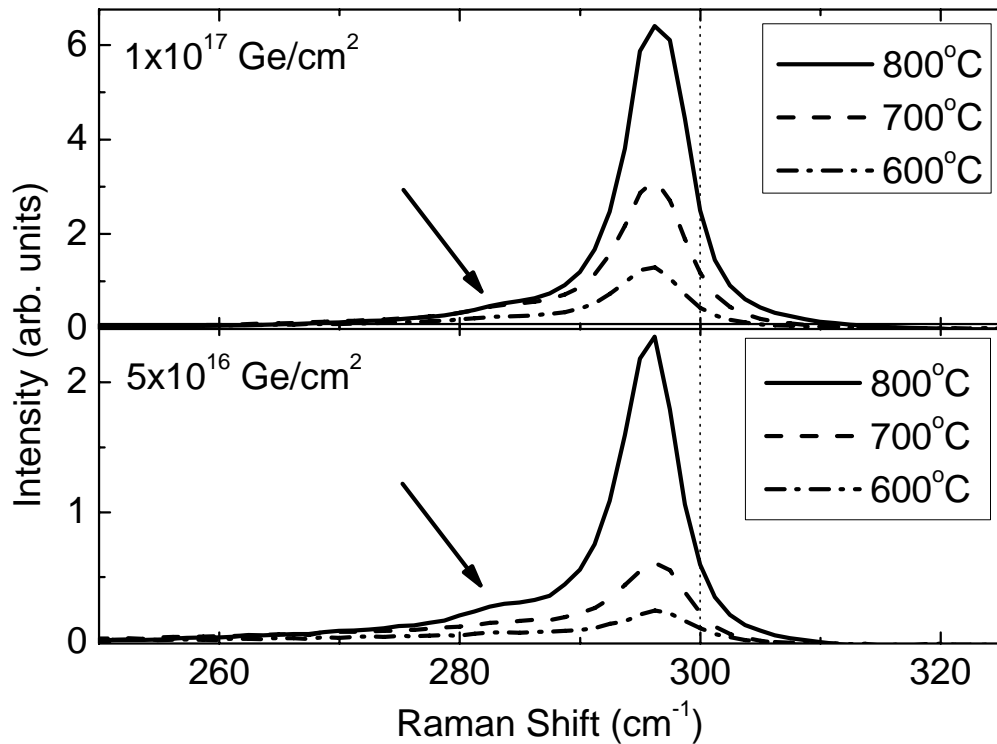


Fig. 3.11. Raman spectra of the samples implanted with doses of  $5 \times 10^{16}$  Ge ions/cm<sup>2</sup> and  $1 \times 10^{17}$  Ge ions/cm<sup>2</sup> after annealing at temperatures of 600, 700 and 800 °C. The dotted line shows the Raman position of 300 cm<sup>-1</sup> to guide the eye

Recently, several studies have focused on the determination of the stress on Ge nanocrystals formed in SiO<sub>2</sub> matrix using Raman spectroscopy [20, 25, 26, 29]. The calculation is more complicated in the case of sapphire matrix due to coexistence of several phases. However, a qualitative analysis can be conducted. The Raman signal of Ge TO band for measured samples does not exhibit a clear shift with the annealing temperature. The lack of shift in the Raman signal can be due both the cancellation of the shifts due to the stress and phonon confinement effect and/or the

effect of the relaxation. The defects, produced during the relaxation, can act as a nonradiative transition centers quenching the light emission from nanocrystals.

### 3.3.5 Ge Nanocrystals in Al<sub>2</sub>O<sub>3</sub> Matrix Formed by Sputtering

Raman spectra of the samples produced using magnetron sputtering under various annealing conditions are shown in Fig. 3.12. The production parameters are given in Table 3.2. While the Raman spectrum of the sample produced at 100 °C demonstrates a characteristic band of amorphous Ge around 280 cm<sup>-1</sup> that of others produced at 500 °C display the crystalline band indicating formation of Ge nanocrystals. Although the sample, labeled as U, is produced using higher power and longer deposition times than the sample, labeled as O, its intensity is lower. The Raman peaks of the both samples are red shifted with respect to bulk Ge. The shift is larger in the latter sample and therefore it may contain larger nanocrystals, or/and nanocrystals are under compressive stress in this sample. The concentration of sample F is higher than sample O. However the peak intensity of sample O is higher. This may be due to the lower deposition time and/or lower Ar pressure of sample F. An AFM image of the sample O is shown in Fig .3.13.

Table 3.2. Details of the production parameter of samples formed by sputtering

Sample Name	Power (W)	Deposition Time (min)	Argon Pressure (x10 <sup>-3</sup> mbar)	Annealing Temperature
K	80	270	5.8	100
F	50	230	5.8	500
U	80	270	4.0	500
O	50	255	4.0	500

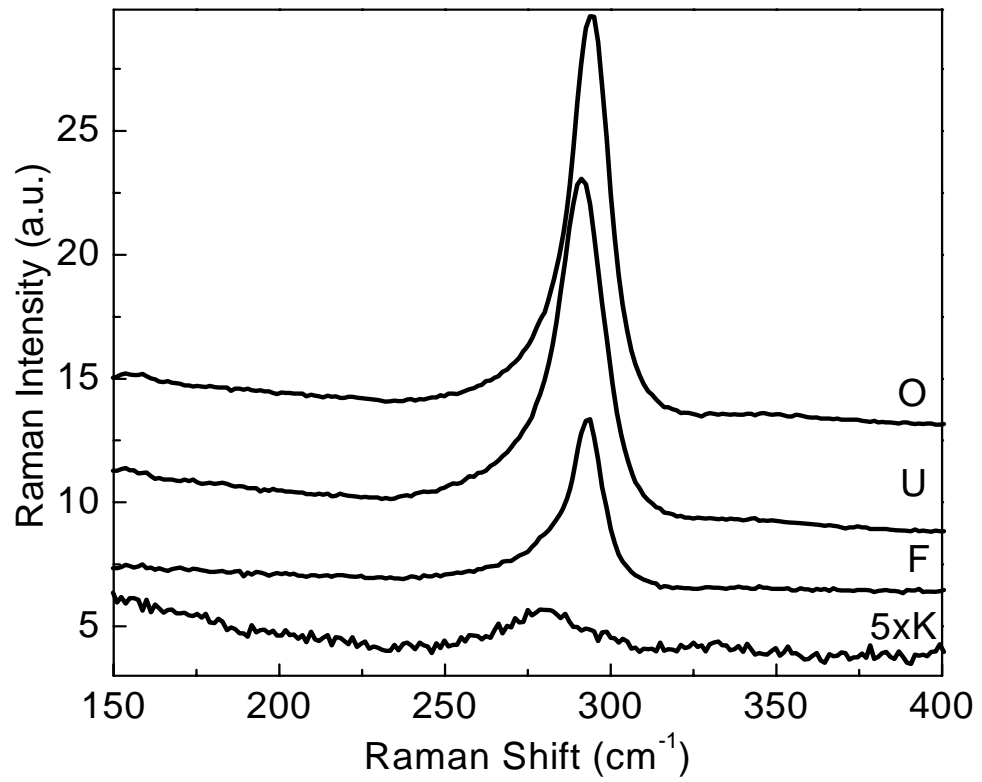


Fig. 3. 12. Raman spectra of the samples produced by sputtering

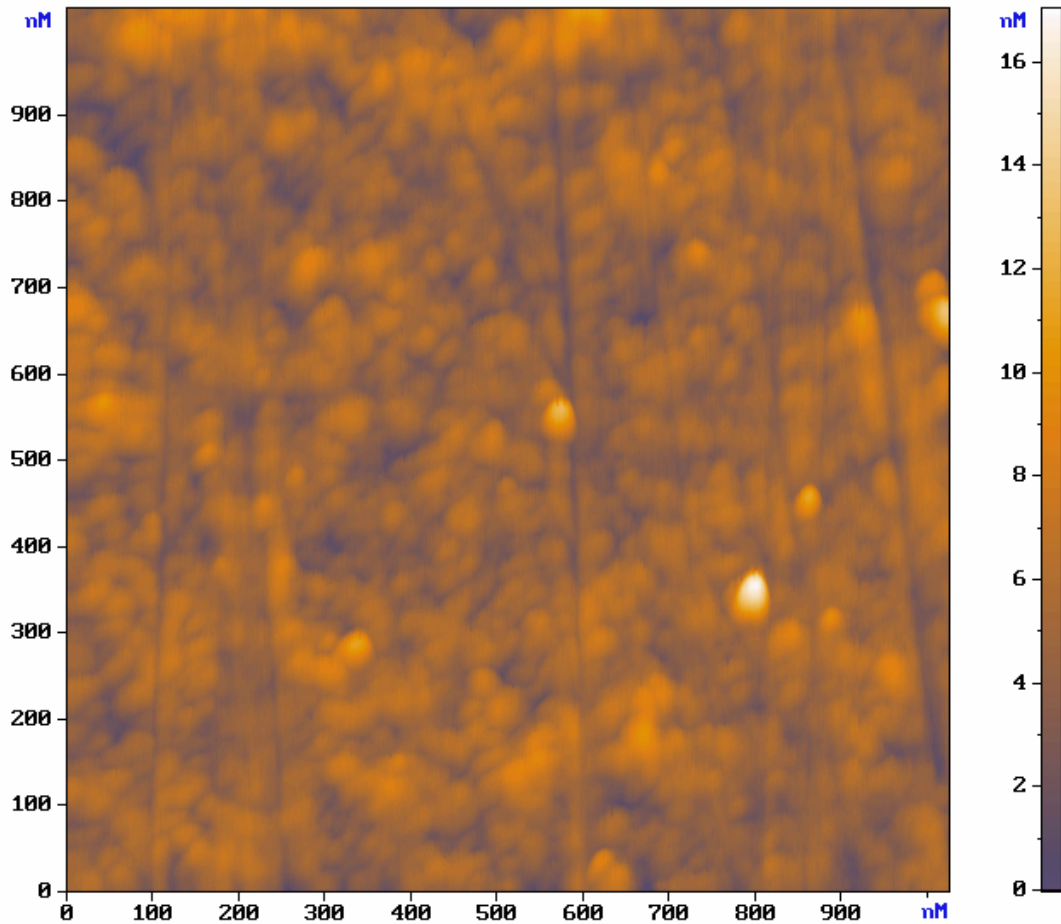


Fig. 3.13. AFM images of the samples produced by sputtering

### 3.3.6 Ge Nanocrystals in SiO<sub>2</sub> Matrix Formed by Laser Ablation

Si substrates with 22 nm thick thermally grown SiO<sub>2</sub> were deposited with Ge by laser ablation using a repetitive (3.5 ns) Nd:YAG laser with an energy of 550 mJ and wavelength of 1.06 μm. The laser light with an intensity of  $1.1 \times 10^{10}$  W/cm<sup>2</sup> was impinged onto Ge target with different number of shots. After deposition, samples were annealed at 750 °C for 30 min under N<sub>2</sub> environment to induce the nanocrystal formation [30]. Fig. 3.14 displays the Raman spectra of the samples produced with

numbers of laser shots of 1058 and 300. The Raman peak positions are measured at 295.3 and 296.5.  $\text{cm}^{-1}$  for the samples with higher and lower number of shots, respectively. Although the peak positions are quite similar, the peak shapes are different for two samples. The Raman band of the sample produced with higher numbers of laser shots can be expressed with a well defined Lorentzian whose FWHM is 5.5  $\text{cm}^{-1}$  while that of the sample produced using lower numbers of laser shots is an asymmetric Lorentzian with a FWHM of 10.8.  $\text{cm}^{-1}$ . As it is discussed in part 3.1, the broadening and asymmetry at the lower wavenumber side is characteristic for the nanocrystal formation.

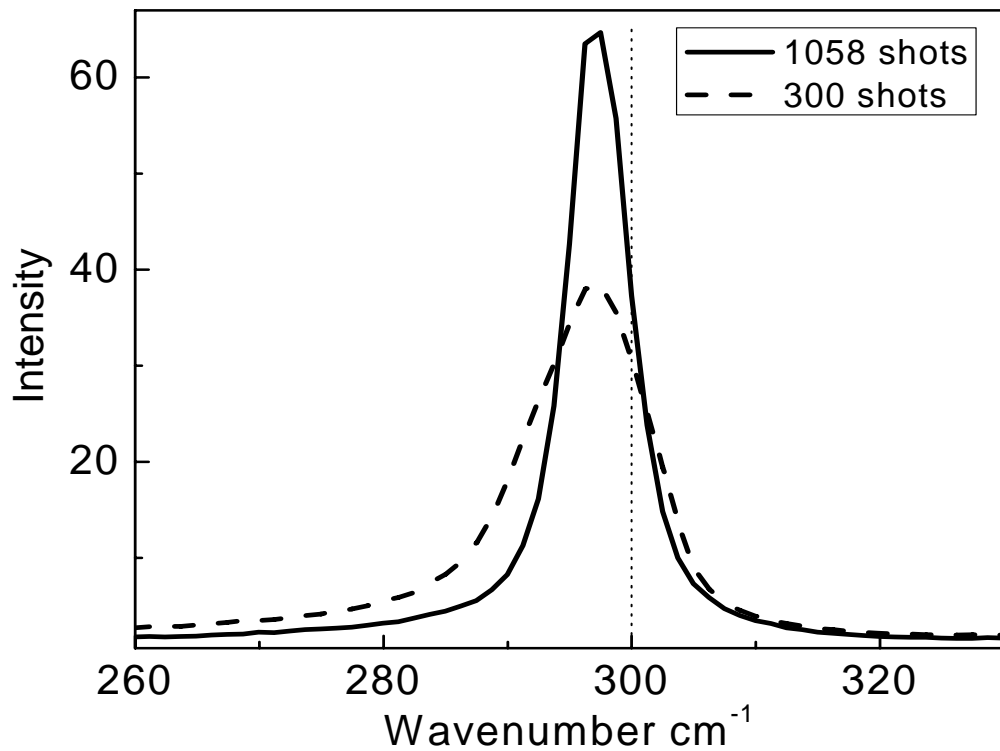


Fig. 3.14. Raman spectra of the samples produced by laser ablation

### 3. 4 CONCLUSIONS

Raman spectroscopy can be successfully employed to show the formation of Si and Ge nanocrystals in SiO<sub>2</sub> and Al<sub>2</sub>O<sub>3</sub> matrices formed by ion implantation, sputtering and laser ablation. It can be used to calculate the size and the ratio of crystalline to amorphous phases of the nanocrystals, the stress on nanocrystals and the temperature around the nanocrystals. The observation of Si nanocrystals formed in SiO<sub>2</sub> matrix on Si substrate using Raman spectroscopy is a tough issue due to the overlap of the signals coming from Si nanocrystals and Si substrate. However, nanocrystals can be detected in samples produced with high concentration of excess Si and annealed at low temperatures. Similar difficulties are seen for samples produced by Ge implantation into SiO<sub>2</sub> matrix on Si substrate where Si LO signal and Ge TO signal coincides.

In agreement with the expectations from the lattice mismatch between Si nanocrystals and the Al<sub>2</sub>O<sub>3</sub> host matrix, large amount of compressive stress is estimated from the analysis of the Raman signal. The amount of the stress was calculated using Raman spectroscopy.

Bimodal distribution of Ge nanocrystals formed in Al<sub>2</sub>O<sub>3</sub> matrix by ion implantation is estimated using Raman spectroscopy which is later proved using TEM. While compressive stress on large nanocrystals was predicted using Raman spectroscopy a tensile one was foreseen on small nanocrystals.

### 3.5 References

1. J. R. Ferraro, K. Nakamoto and C. W. Brown, *Introductory Raman Spectroscopy*, Elsevier Science, USA, 2003.
2. M. Pemble, J. C. Vicerma, *Surface Analysis*, John Wiley & Sons, England, 2003.
3. Nanometrology Report, Retrieved from [www.nanoforum.org](http://www.nanoforum.org) (30/01/2007).
4. L. Khriachtchev, M. Rasanen and S. Novikov, *Appl. Phys. Lett.* 88, 013102, 2006.
5. H. Richter, Z. P. Wang, and L. Ley, *Solid State Commun*, 39, 625, 1981.
6. I. H. Campbell and P. M. Fauchet, *Solid State Commun.* 58, 739, 1986.
7. H. Munder, C. Andrzejak, M. G. Berger, U. Klemradt, H. Luth, R. Herino, and M. Ligeon, *Thin Solid Films*, 221, 27, 1992.
8. J. Zi, H. Buscher, C. Falter, W. Lugwig, K. Zhang, and X. Xie, *Appl. Phys. Lett.* 69, 200, 1996.
9. P. Mishra and K. P. Jain, *Mater. Sci. and Engr. B* 95, 202, 2002.
10. U. Serincan, G. Kartopu, A. Guennes, T. G. Finstad, R. Turan, Y. Ekinici, and S. C. Bayliss, *Semicond. Sci. Technol.* 19, 247, 2004.
11. N. Islam, A. Pradhan, S. Kumar, *J. Appl. Phys.* 98, 024309, 2005.
12. G. Faraci, S. Gibilisco, P. Russo, and A. Penniisi, *Phys. Rev. B* 73, 033307, 2006.
13. F. Iacona, G. Franzò, E. Ceretta Moreira, F. Priolo, *J. Appl. Phys.* 89, 8354, 2001.
14. G. Franzò, A. Irrera, E. Ceretta Moreira, M. Miritello, F. Iacona, D. Sanfilippo, G. Di Stefano, P.G. Fallica, and F. Priolo, *Appl. Phys. A* 74, 1, 2002.
15. G. Viera, S. Huet, and L. Boufendi, *J. Appl. Phys.* 90, 4175, 2001.
16. E. Bustarret, M. A. Hachicha, and M. Brunel, *Appl. Phys. Lett.* 52, 1675, 1988.
17. J. Marcia, E. Martin, A. Perez-Rodriquez, J. Jimenez, J. M. Morante, B. Aspar, and J. Margial, *J. Appl. Phys.* 82, 3730, 1997.

18. S. Yerci, I. Dogan, M. Genisel, S. Tokay, U. Serincan, A. Aydinli, and R. Turan, *J. Appl. Phys.* 100, 074301, 2006.
19. C. V. Raman, *The molecular scattering of light*, Nobel Lecture, 1930.
20. A. Welner, V. Pillard, H. Coffin, N. Cherkashin, and C. Bonafos, *J. Appl. Phys.* 96, 2403, 2004.
21. Y. Kanzawa, S. Hayashi, and K. Yamamoto, *J. Phys.: Condens. Matter.* 8, 4823, 1996.
22. T. Zheng and Z. Li, *Superlatt. Microstruct.* 37, 227, 2005.
23. D. Nesheva, C. Raptis, A. Peraklis, I. Bineva, Z. Aneva, Z. Levi, S. Alexandrova, and H. Hofmeister, *J. Appl. Phys.* 92, 8, 4678, 2002.
24. Ch. Ossadnik, S. Veprek, and I. Gregora, *Thin Solid Films* 337, 148, 1999.
25. I. D. Desnica-Frankovic, K. Furic, U. V. Desnica, M. C. Ridgway, and C. J. Glover, *Nucl. Instr. and Meth. In Phys. Res. B*, 178, 192, 2001.
26. A. Welner, V. Pillard, C. Bonafos, H. Coffin, A. Claverie, B. Schmidt, K. H. Heinig, *J. Appl. Phys. Vol. 94, No. 9*, 5639, 2003.
27. Q. Xu, I. D. Sharp, C. Y. Liao, D. O. Yi, J. W. Ager III, J. W. Beeman, K. M. Yu, D. C. Chrzan, E. E. Haller, *Mater. Res. Soc. Symp. Proc.* 880E, BB5.22.1, 2004.
28. S. Yerci, I. Yildiz, A. Seyhan, M. Kulakci, U. Serincan, M. Shandalov, Y. Golan, and R. Turan, *Mater. Res. Soc. Symp.* 958, L7, 2006.
29. I. E. Tyschenko, A. B. Talochkin, A. G. Cherkov, K.S. Zhuravlev, and R.A. Yankov, *Solid State Commun.* 129, 63, 2004.
30. M. Rosinski, J. Badziak, A. Czarnecka, P. Gasior, P. Parys, M. Pisarek, R. Turan, J. Wolowski, S. Yerci, *Mater. Sci. in Semicond. Proc.* 9, 655, 2006.

## CHAPTER 4

### CHARACTERIZATION OF NANOCRYSTALS NANOSTRUCTURES USING X-RAY DIFFRACTION

#### 4.1 Introduction

X-ray diffraction in classical sense can be defined as an elastic scattering of X-rays by the electrons of atoms. In other words, an electron in the path of incoming electromagnetic wave (or X-ray) excited to periodic vibrations by the changing field. Therefore it behaves as a source of electromagnetic waves of the same frequency and wavelength. In crystals, the scattered X-ray can be considered as centers for series of spherically spreading waves which forms zero-, first-, second-, or higher order diffracted beams in certain directions. The theory and mathematical representation of X-Ray diffraction by a simple lattice was studied in detail by M. v. Laue [1]. Later, W. L. Bragg [2] developed the theory and found that the diffracting plane is a lattice plane, and stated the formula (Eqn. 4.1) which is known with his name [3].

$$n\lambda = 2d \sin \Theta \quad (4.1)$$

where  $n$  is an integer, and representing the orders of the diffraction,  $\lambda$  is the wavelength of the X-ray beam,  $\Theta$  is the half of the deviation of the diffracted beam and  $d$  is the interplanar spacing for a plane, and equal to

$$d = \frac{a_0}{\sqrt{h^2 + k^2 + l^2}} \quad (4.2)$$

where  $a_0$  is the constant spacing between the atoms, and  $h$ ,  $k$  and  $l$  are the corresponding Miller indices.

It has been more than a century, Scherrer first showed that the coherence length,  $D$  which is representing the mean size of the crystallites forming a powder is related to the pure X-Ray diffraction broadening,  $\beta$ , by the equation [3, 4],

$$D = \frac{\kappa\lambda}{\beta \cos \Theta} \quad (4.3)$$

where  $\kappa$  is Scherrer constant and approximately equal to unity.

This formula has become more and more popular with the advances in micro and nanotechnology. Recently, many studies have focused on the calculation of the mean dimension of nanocrystals using Scherrer's formula [5-9]. Although size calculation using Scherrer's formula has advantages of being simple in instrumentation, non-destructive, and easy in data analysis, it has some physical and mathematical limitations.

In the Scherrer's formula,  $\lambda$  and  $\Theta$  are two constants that can be measured precisely. However, the determination of  $\kappa$  and the measurement of  $\beta$  values are not simple. The  $\kappa$  value, which depends on several factors (e.g. nanocrystal shape and size), differs in several publications. The widely accepted value of  $\kappa$  for cubic crystals are 0.89 [3] or 0.94 [10]. The  $\kappa$  value is strongly size dependent for nanocrystals with dimensions less than 3 nm. Therefore, the validity of the formula is questionable under this dimension. Moreover, the formula become more questionable when complicated nanocrystal shapes, bimodal and/or size distributions are present due to the dependent of the  $\kappa$  value on nanocrystal size [3].

It is known that the XRD lines of the stressed materials shifts or exhibit asymmetric and broadened line profiles depending on the magnitude of the stress [3, 6-9]. Therefore, misinterpretation may arise from the fact that both stress and the decrease in dimension of coherence length can cause broadening. Moreover, another physical limitation arises from the XRD instrument itself. A measured FWHM of a diffraction line is a combination of the lattice scatterings and instrumental broadening. The instrumental broadening, as determined using an ideal single crystal, should be deconvoluted from the measured FWHM to find the natural  $\beta$  value [3, 7-10].

It should also be noted that the calculation of the mean sizes of the nanocrystals from Scherrer's formula requires a numerical fitting procedure which has its own limitations when the peaks overlap and there are two or more phases. Finally, due to the approximations used by Scherrer, the calculated size values are slightly lower than effective crystal size (i.e. the formula itself is a lower size approximation) [3, 10].

## **4.2 Instrumentation**

XRD measurements, given in this dissertation, were conducted with Rigaku Miniflex X-Ray powder diffractometer, located in the Department of Physics at METU, using Conventional Bragg-Brentano  $\Theta$ - $2\Theta$  scans. The schematic of the measurement system is shown in Fig.4.1. Cu  $K_{\alpha}$  (0.154 nm) radiation was used as X-Ray source, and measurements were conducted with scans between  $5^{\circ}$  and  $80^{\circ}$  at  $0.02^{\circ}$  steps. Acquisition time per angular steps of 6 or 24 s was used to enhance the signal to noise ratio. The data used was the average of three scans. The FWHM of the diffraction peak ( $0.122^{\circ}$ ) of a standard sample of microcrystalline powder Si was recorded to eliminate the instrumental line broadening. Among the peaks of the standard sample shown in Fig. 4.2, Si (111) peak at  $28.4^{\circ}$  was used for both the correction of the instrumental broadening and the calculation of the nanocrystal sizes.

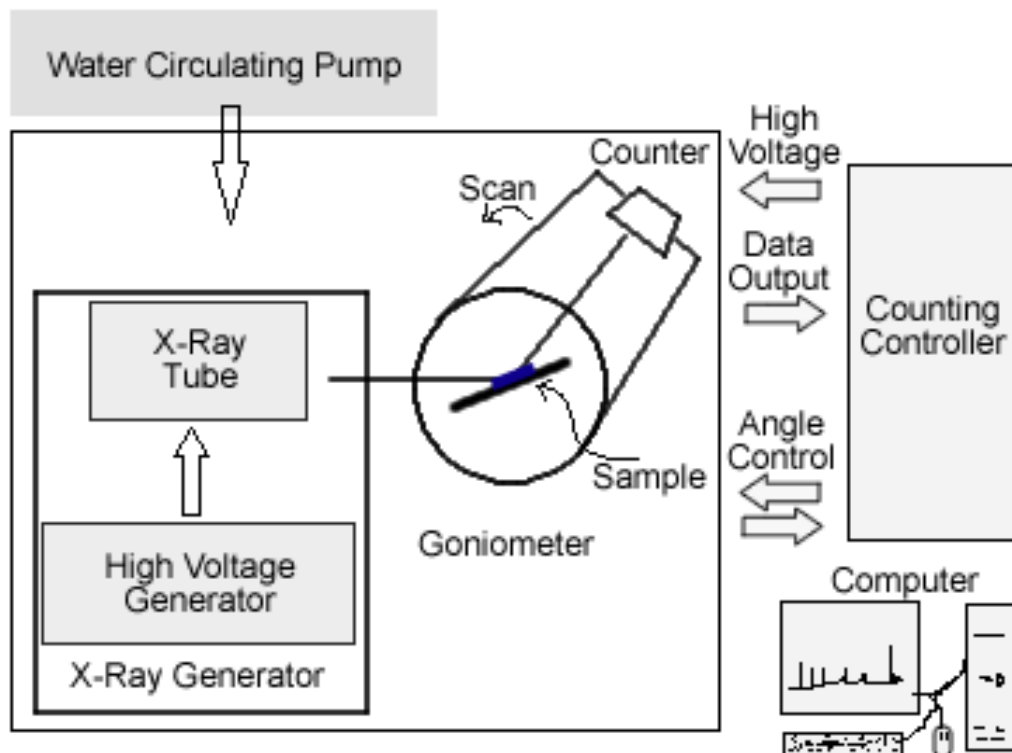


Fig. 4.1. Schematic of a X-Ray Diffractometer with its components

The Scherrer's constant,  $\kappa$ , was assumed to be 0.89 in the mean nanocrystals size calculations. The residual Cu  $K_{\alpha 2}$  was corrected by using the Rachinger correction method which assumes the intensity of the  $K_{\alpha 2}$  to be half that of  $K_{\alpha 1}^2$  [3, 11]. The background correction was performed assuming quadratic polynomial background which gives the best fit. Peak profiles were assumed to be pseudo-Voigt, which is a combination of Gaussian and Cauchy line shapes.

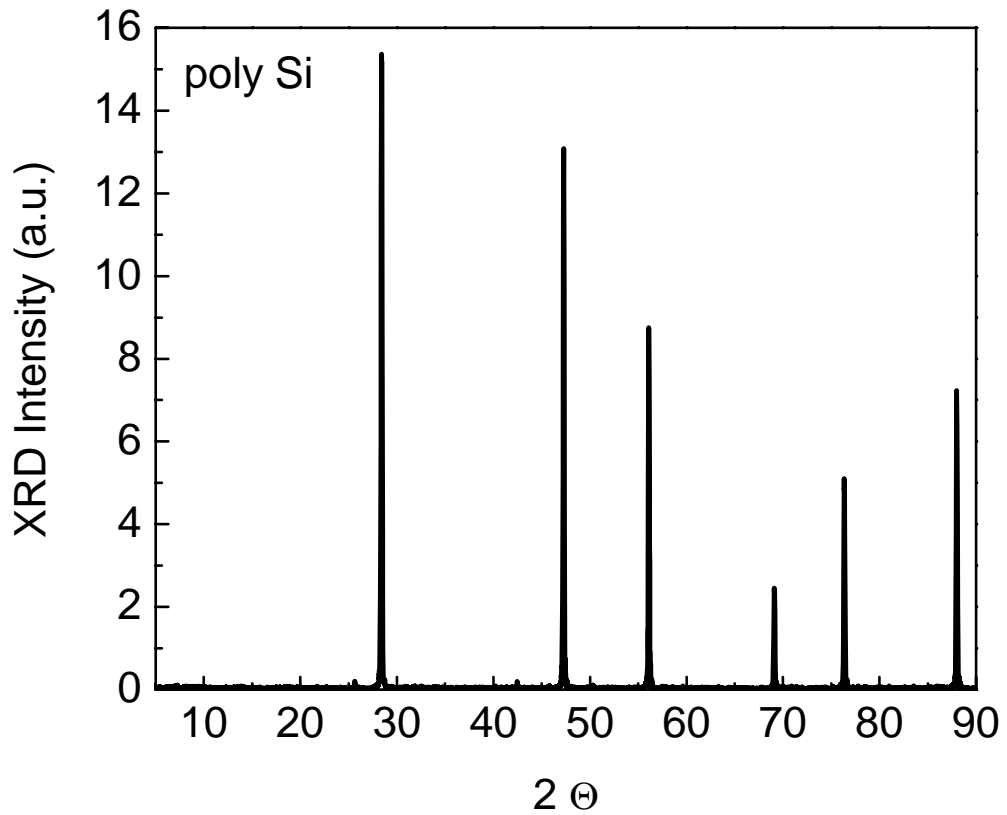


Fig. 4.2. XRD spectrum of a standard poly-Si which may be used to find the instrumental broadening

### 4.3 Probing Nanostructures with XRD

#### 4.3.1 Si Nanocrystals Formed into Al<sub>2</sub>O<sub>3</sub> by Ion Implantation

C-plane oriented  $\alpha$ -Al<sub>2</sub>O<sub>3</sub> substrates were implanted with 100-keV <sup>28</sup>Si<sup>+</sup> ions at a dose of  $1 \times 10^{16}$ ,  $1 \times 10^{17}$  and  $2 \times 10^{17}$  Si/cm<sup>2</sup>, and annealed at 600, 700, 800, 900 and 1100 °C in N<sub>2</sub> ambient for 2 h to induce Si nanocrystal formation. The projected range (Rp) of the Si ions was calculated as 81 nm using TRIM software.

In Fig. 4.3, while the broad band around  $24^\circ$  is due to amorphous  $\text{SiO}_2$  or  $\text{Al}_2\text{O}_3$ , the sharp peaks located at  $37.5$ ,  $41.8$  and  $53.2^\circ$  are due to the crystalline substrate. The XRD signals corresponding to Si (111), with  $2\Theta$  value around  $28.6^\circ$ , became evident at annealing temperatures of  $900^\circ\text{C}$  and  $1000^\circ\text{C}$  for the samples implanted with doses of  $2 \times 10^{17} \text{ Si/cm}^2$  and  $1 \times 10^{17} \text{ Si/cm}^2$ , respectively. Measured spectra from samples annealed at  $900$ ,  $1000$  and  $1100^\circ\text{C}$  with the dose of  $2 \times 10^{17} \text{ Si/cm}^2$  as well as those annealed at  $1000$  and  $1100^\circ\text{C}$  with the dose of  $1 \times 10^{17} \text{ Si/cm}^2$  are displayed in Fig. 4.3. The formation of Si-nanocrystals having (111) direction has been extensively studied in other matrices such as  $\text{SiO}_2$  using XRD [6-8]. Moreover, the same structure was studied in sapphire matrix with electron diffraction [12-14]. As shown in the inset of Figure 4.3, Si (111) XRD signal broadens with decreasing annealing temperatures enabling us to calculate the average grain sizes of nanocrystals and their evolution with the annealing temperature. Fig. 4.4 displays the Si (111) XRD line of the sample implanted with a dose of  $2 \times 10^{17} \text{ Si/cm}^2$  and annealed at  $1100^\circ\text{C}$ , and a successive fit applied to find the FWHM of the peak.

Following Scherrer's formula, average nanocrystal sizes are estimated to be  $7.2 \pm 0.2$ ,  $5.1 \pm 0.2$  nm in samples implanted with the dose of  $2 \times 10^{17} \text{ Si/cm}^2$  and subsequently annealed at  $1100$  and  $1000^\circ\text{C}$ , respectively. Similarly, in samples implanted with the dose of  $1 \times 10^{17} \text{ Si/cm}^2$ , average Si nanocrystal sizes are found to be  $7.0 \pm 0.2$  nm and  $3.9 \pm 0.2$  nm for annealing temperatures of  $1100$  and  $1000^\circ\text{C}$ , respectively. These values of nanocrystal sizes are in good agreement with the reported values as determined from HRTEM analysis [14]. The uncertainties given in D values are statistical errors associated with the determination of the FWHM of Si (111) Bragg peak only. While stress may induce additional broadening, it is difficult to deconvolute the effect of finite size and stress from the FWHM of the diffraction peak. Tensile or compressive stress will also cause a shift in the Bragg diffraction peak position from its bulk counterpart which can be used to evaluate the magnitude and direction of stress. We, therefore, used the position of the diffraction peak position to evaluate stress from the XRD data.

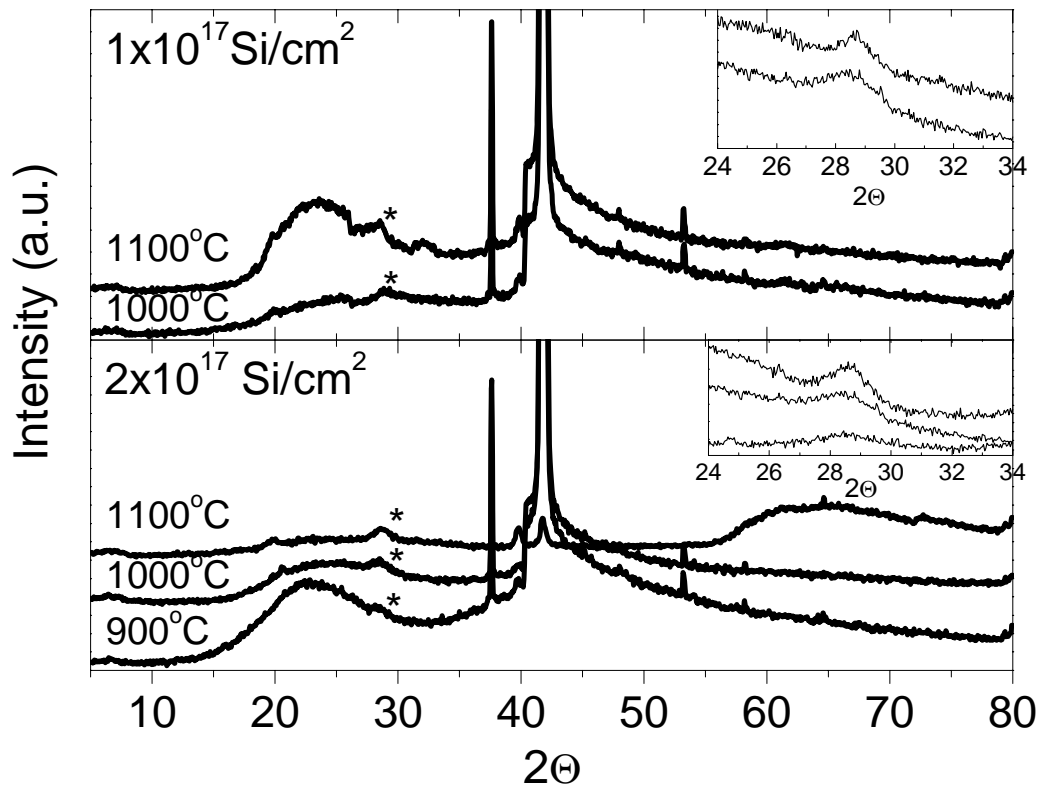


Fig. 4.3. The evolution of XRD signal of Si implanted  $\alpha$ - $\text{Al}_2\text{O}_3$  matrix as a function of implantation dose and annealing temperature. (\*) indicates the Si (111) peaks. Inset shows details of Si (111) peaks.

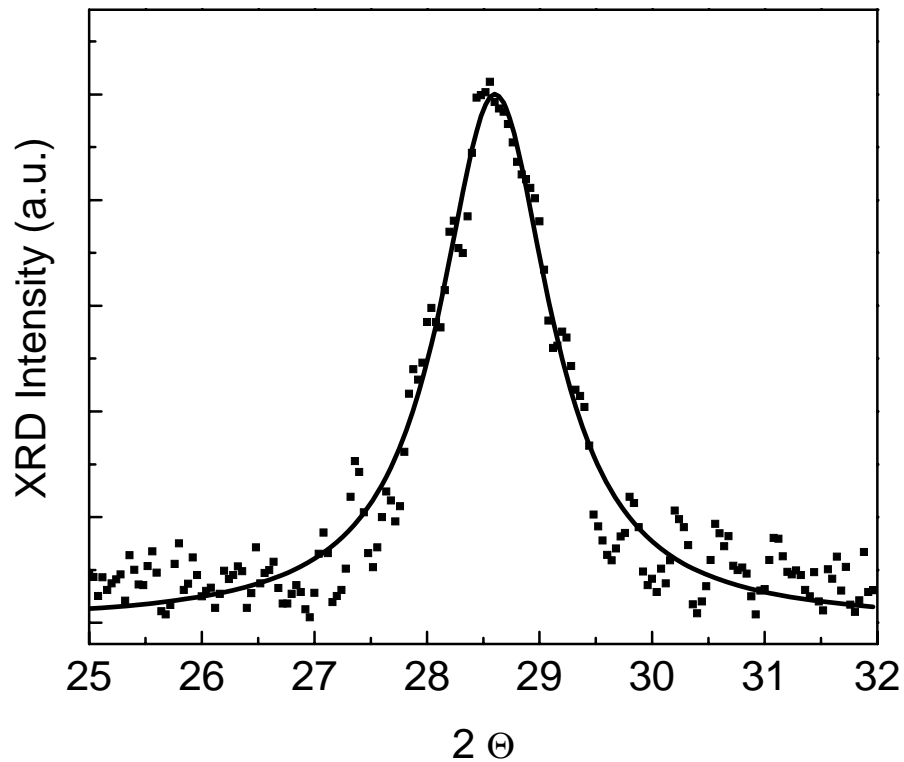


Fig. 4.4. Si (111) XRD peak at  $28.6^\circ$ . Solid line is a fit to data using a pseudo-Voigt function

The measured lattice constant for the nanocrystals are always smaller than the lattice constant of  $5.43 \text{ \AA}$  obtained from the reference sample of polycrystalline Si, for all doses of implantation and temperatures of annealing. This implies that a compressive stress is present on the nanocrystals with the mean lattice compression of  $\Delta a/a=0.04\%-0.11\%$ . This result can be explained with the lattice mismatch between the nanocrystals and the host matrix. A reasonable explanation for this stress requires a careful examination of the phase transformations of both the nanocrystals and the host matrix during the ion implantation and annealing process. While the nanocrystals formed at lower annealing temperatures ( $800\text{-}900^\circ\text{C}$ ) are mostly amorphous they crystallize during annealing at around  $1100^\circ\text{C}$  [15]. For the

surrounding matrix, although no phase formation other than  $\alpha$ -Al<sub>2</sub>O<sub>3</sub> were observed in this work, the creation of  $\Theta$ -Al<sub>2</sub>O<sub>3</sub> were previously reported after annealing of amorphized Al<sub>2</sub>O<sub>3</sub> matrix by ion implantation with the dose of  $5 \times 10^{16}$  Si/cm<sup>2</sup> [13].  $\Theta$ -Al<sub>2</sub>O<sub>3</sub> has a monoclinic structure with lattice constants of  $a=11.79\text{\AA}$ ,  $b=2.91\text{\AA}$  and  $c=5.62\text{\AA}$ . The minimum lattice mismatch is about 3.4% which can be responsible from the compressive stress. On the other hand,  $\alpha$ -Al<sub>2</sub>O<sub>3</sub> is the most stable phase among the Al<sub>2</sub>O<sub>3</sub> phases which forms after 1000-1100 °C annealing.  $\alpha$ -Al<sub>2</sub>O<sub>3</sub> has a hexagonal structure with the lattice constants of  $4.758\text{\AA}$  and  $12.991\text{\AA}$ . Therefore, in the present case, minimum lattice mismatch can be calculated as 14% between the nanocrystals and the host matrix. This mismatch should generate large amounts of mechanical stress on Si nanocrystals.

#### 4.3.2 Ge Nanocrystals Formed into Al<sub>2</sub>O<sub>3</sub> by Ion Implantation

C-plane oriented  $\alpha$ -Al<sub>2</sub>O<sub>3</sub> substrates were implanted using 100-keV <sup>74</sup>Ge ions at doses of  $5 \times 10^{16}$  and  $1 \times 10^{17}$  Ge ions/cm<sup>2</sup>. The samples were subsequently annealed at temperatures ranging between 500 and 800 °C in vacuum for 1 h to induce Ge nanocrystal formation.

In Fig. 4.5, while the broad band around 24° is due to amorphous SiO<sub>2</sub> or Al<sub>2</sub>O<sub>3</sub>, the sharp peaks located at 37.5, 41.8 and 53.2° are due to the crystalline substrate. The XRD spectra of implanted samples with doses of  $5 \times 10^{16}$  Ge ions/cm<sup>2</sup> and  $1 \times 10^{17}$  Ge ions/cm<sup>2</sup> and annealed at temperatures of 700 and 800 °C are given in Fig. 4.5. Sharp peaks at around 20.7° and 37.8° are due to the crystalline bulk substrate. Samples annealed at lower temperatures (<800 °C) exhibit  $\alpha$ -Al<sub>2</sub>O<sub>3</sub> peaks only. However, a broad peak (marked with #), assigned to Ge nanocrystals with (111) direction, appears at around 27.5° for samples with both implantation doses and same annealing temperature of 800 °C [16]. The broad feature of the peak is due to the decrease in the coherence length (indicating the existence of nanocrystals). The sizes of the nanocrystals were estimated as ~14 nm from XRD peaks using Scherer's formula. According to TEM measurements, we propose a bimodal

distribution for Ge nanocrystals. While the mean sizes of the nanocrystals are around 15 nm at the highly implanted region, near the projected range of implantation, it is found as 4 nm underneath this region. Therefore one can say that the XRD peak seen at  $27.5^\circ$  resulted from the large nanocrystals formed in highly implanted region and the calculated mean size of the nanocrystals using Scherrer's formula is very close to the value found from HRTEM [9, 17]. A micrograph of the sample implanted with  $1 \times 10^{17}$  Ge/cm<sup>2</sup> and subsequently annealed at 800 °C is given in Fig. 4.6.

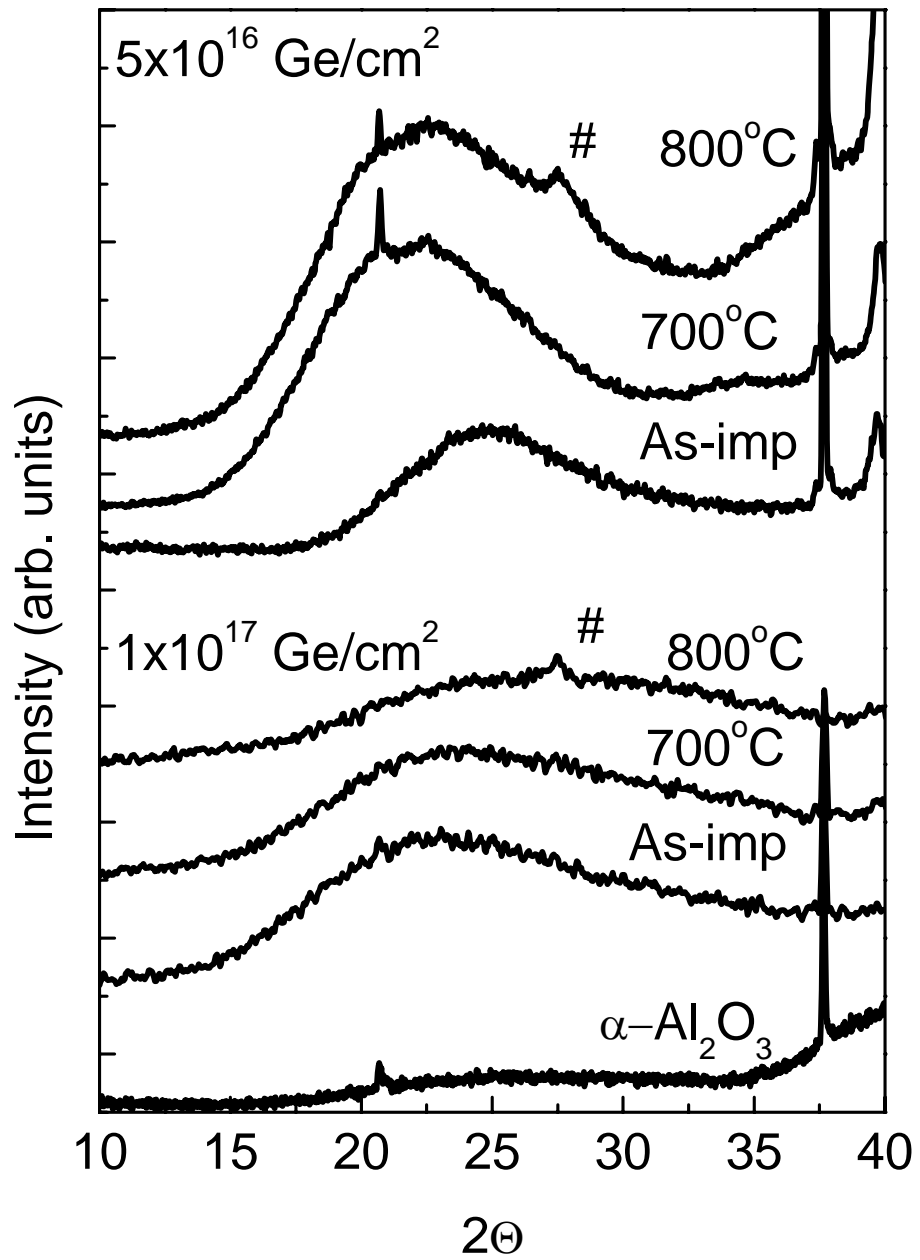


Fig. 4.5. XRD spectra of the samples implanted with doses of a)  $5 \times 10^{16}$  Ge ions/cm<sup>2</sup> and b)  $1 \times 10^{17}$  Ge ions/cm<sup>2</sup> and annealed at temperatures of 700 and 800 °C. Ge (111) signal is marked with (#)

On the other hand, the difference between XRD signal observed at  $27.5^\circ$  and the expected value of  $27.3^\circ$  for bulk Ge (111) indicates that nanocrystals are under compressive stress.

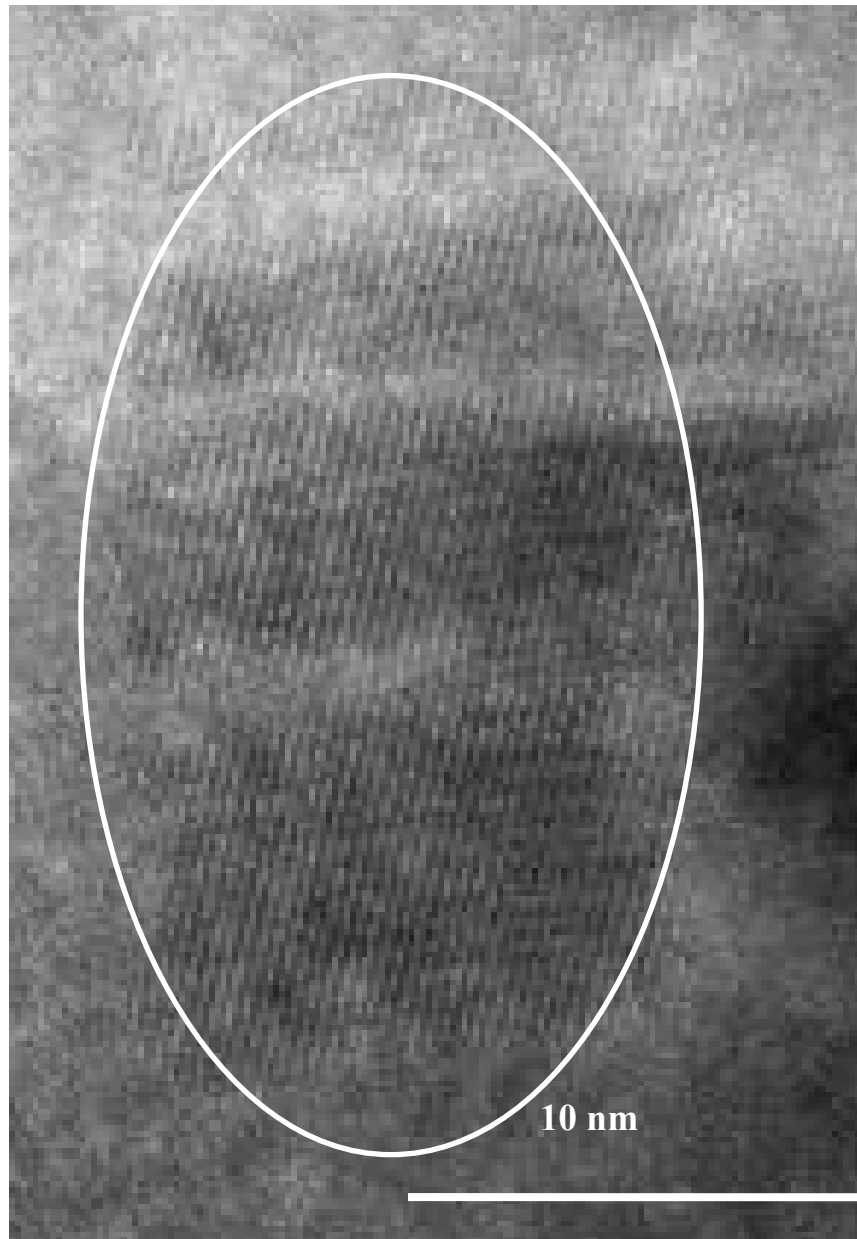


Fig. 4.6. HRTEM micrograph of the sample implanted with  $1 \times 10^{17}$  Ge/cm<sup>2</sup> and subsequently annealed at 800 °C

### 4.3.2 Ge Nanocrystals Formed into SiO<sub>2</sub> by Laser Ablation

Repetitive laser shots (3.5 ns) with a power of  $1.1 \times 10^{10}$  W and wavelength of 1.06  $\mu\text{m}$  were introduced to Ge target to deposit 22 nm thick thermally grown SiO<sub>2</sub> on Si substrate located at 6 cm from the target. Samples were annealed at 750 °C for 30 min to induce the nanocrystal formation [18]. XRD spectra of samples produced using 1058 and 300 laser shots are given in Fig. 4.7. It should be noted that the sample produced with higher numbers of shots is thicker and the vacuum pressure is lower during its deposition. As it is seen Fig. 4.7, Bragg peak for Ge (111) sharpens with the numbers of laser shots. Size calculation using Scherrer's formula was performed for Ge nanocrystals with orientations of (111), (220) and (311). The calculated values are given in Table 4.1.

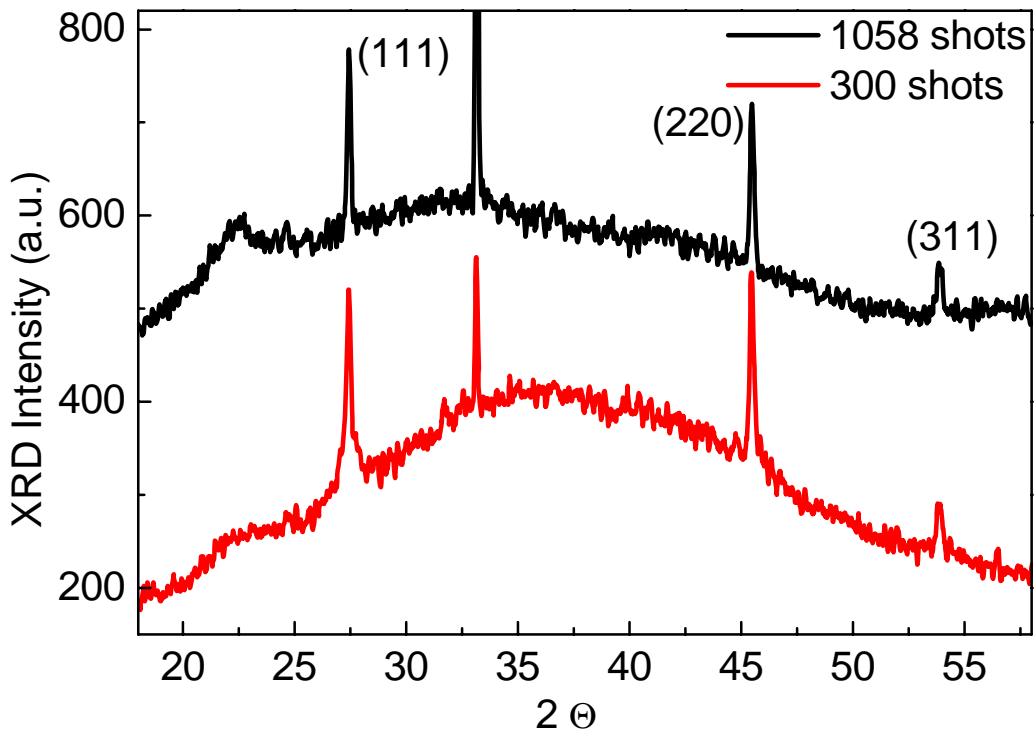


Fig. 4.7. XRD spectra of the samples produced by laser ablation

Table 4.1 The calculated nanocrystal sizes at various crystals directions for samples formed by laser ablation

# of laser Shots	Nanocrystals sizes in directions of			
	(111)	(220)	(311)	average
<b>1058</b>	<b>122.8</b>	<b>64.4</b>	<b>47.9</b>	<b>78.4</b>
<b>300</b>	<b>33.7</b>	<b>44.6</b>	<b>23.4</b>	<b>33.9</b>

As it is seen from Table 1, larger nanocrystals formed in the sample produced with higher numbers of shots. Moreover, nanocrystals size calculated using Scherrer's formula varies with crystal direction. This may be an indication of the selective growth of a crystalline direction. For examples, (220) direction can be more favorable near to the interface while (111) is in the bulk SiO<sub>x</sub>.

#### 4.4 Conclusions

The formation of Si and Ge nanocrystals in Al<sub>2</sub>O<sub>3</sub> matrix by ion implantation and subsequent annealing were studied with X-ray diffraction. The nanocrystal sizes were obtained from the width of Si and Ge (111) XRD pattern by applying Scherrer's formula. From the blue shift in XRD lines of Si (111) and Ge (111), Si and Ge nanocrystals were found to be under compressive stress. Although the high signal to noise ratio of XRD signals hinder a possible stress calculation it is estimated from Raman signals in chapter 3 that Si nanocrystals are more stressed than Ge ones.

Formation of Ge nanocrystals in Al<sub>2</sub>O<sub>3</sub> matrix by ion implantation at annealing temperatures as low as 500 °C was demonstrated by using Raman spectroscopy in previous chapter. However, XRD signals from Ge nanocrystals were obtained only for the temperature of 800 °C. It was calculated using Scherrer's formula that Ge nanocrystals with mean sizes of 14 nm were formed in regions near the projected range of implanted ions. This value is very close to the value obtained from HRTEM, 15 nm. TEM micrographs show a bimodal distribution of sizes for Ge nanocrystals which may mislead the size evaluation in XRD, and it gives smaller values.

## 4.5 References

1. M. v. Laue, *Ann. Physic*, 41, 971, 1913.
2. W. L. Bragg, *Proc. Cambridge Phil. Soc.*, 17, 43, 1913.
3. H. R. Klug, L. E. Alexander, *X-Ray Diffraction Procedures for Polycrystalline and Amorphous Materials*, John Wiley & Sons, Inc. New York, 1974.
4. P. Scherrer, *Gottinger Nachrichten*, 2, 98, 1918.
5. A. Weibel, R. Bouchet, F. Boule'h, and P. Knauth, *Chem. Mater.*, 17, 2378, 2005.
6. M. Morales, Y. Leconte, R. Rizk, and D. Chateigner, *J. Appl. Phys.* 97, 034307, 2004.
7. D. Comedi, O. H. Zalloum, E. A. Irving, J. Wojcik, T. Roschuk, M. J. Flynn, and P. Mascher, *J. Appl. Phys.* 99, 023518, 2006.
8. S. Yerci, I. Dogan, M. Genisel, S. Tokay, U. Serincan, A. Aydinli, and R. Turan, *J. Appl. Phys.* 100, 074301, 2006.
9. S. Yerci, M. Kulakci, U. Serincan, M. Shandalov, Y. Golan, and R. Turan, *J. Nanosci. and Nanotech.*, (in press)
10. B. E. Warren, *X-Ray Diffraction*, Addison-Wesley, USA, 1969.
11. W. A. Rachinger, *J. Sci. Instrum.* 25, 254, 1948.
12. S. Yanagiya, M. Ishida, *J. Electronic Materials*, 28, 5, 498 (1999).
13. C. J. Park, Y. H. Kwon, Y. H. Lee, T. W. Kang, H. Y. Cho, S. Kim, S. H. Choi, R. G. Elliman, *Appl. Phys. Lett.* 84, 14, 2667 (2004).
14. D. I. Tetelbaum, A. N. Mikhaylov, O. N. Gorshkov, A. P. Kasatkin, A. I. Belov, D. M. Gaponova, and S. V. Morozov, *Vacuum* 78, 519 (2005).
15. G. Viera, S. Huet, and L. Boufendi, *J. Appl. Phys.* 90, 8, 4175 (2001).
16. Y. Zhu and P. P. Ong, *J. Phys.: Condens. Matter*, 13, 4075, 2001.
17. Q. Xu, I. D. Sharp, C. Y. Liao, D. O. Yi, J. W. Ager III, J. W. Beeman, K. M. Yu, D. C. Chrzan, E. E. Haller, *Mater. Res. Soc. Symp. Proc.* 880E, BB5.22.1, 2004.
18. M. Rosinski, J. Badziak, A. Czarnecka, P. Gasior, P. Parys, M. Pisarek, R. Turan, J. Wolowski, S. Yerci, *Mater. Sci. in Semicond. Proc.* 9, 655, 2006.

## CHAPTER 5

### CHARACTERIZATION OF NANOSTRUCTURES USING X-RAY PHOTOELECTRON SPECTROSCOPY

#### 5.1 Introduction

XPS was developed in the mid 1960s by K. Siegbahn and coworkers. He was awarded the Nobel Prize for Physics in 1981 for this invention [1]. The method was primarily named as electron spectroscopy for chemical analysis (ESCA) but later on it was considered too general with the developments of other electron spectroscopy methods, and XPS became widely used. XPS is a surface sensitive method and requires ultra high vacuum (UHV) environment. X-Ray is used to eject the electrons of an atom from its core shell and emitted electrons are analyzed according to their kinetic energies. The method is currently most widely used surface-analysis technique, and it supplies information about the atomic composition of the surface and chemical environments (i.e. binding states, oxidation states) of the elements, except Hydrogen and Helium [2].

Soft X-ray photons are generally directed to the surface of the material. Although, X-ray can penetrate the depth of the sample in micrometer order (1-10  $\mu\text{m}$ ) the ejected electrons that can reach to the analyzer are emitted from the uppermost tens of Angstroms ( $\text{\AA}$ ) [2]. When the incident photon interacts with an electron with a binding energy of  $E_B$  in a core shell, the photoelectric effect occurs, if the energy of the photons is greater than the binding energy (Fig. 5.1). The energy of the photon

is partly used to remove the electron from the core shell, and the rest is transferred to electron as kinetic energy ( $E_{kin}$ ). Since the Fermi level, by definition corresponds to zero binding energy, some more energy (work function,  $\Phi$ ) must be spent to extract to electron to the vacuum level. The kinetic energy of the emitted electron can be written as [3]

$$E_{kin} = h\nu - E_B - \Phi \quad (5.1)$$

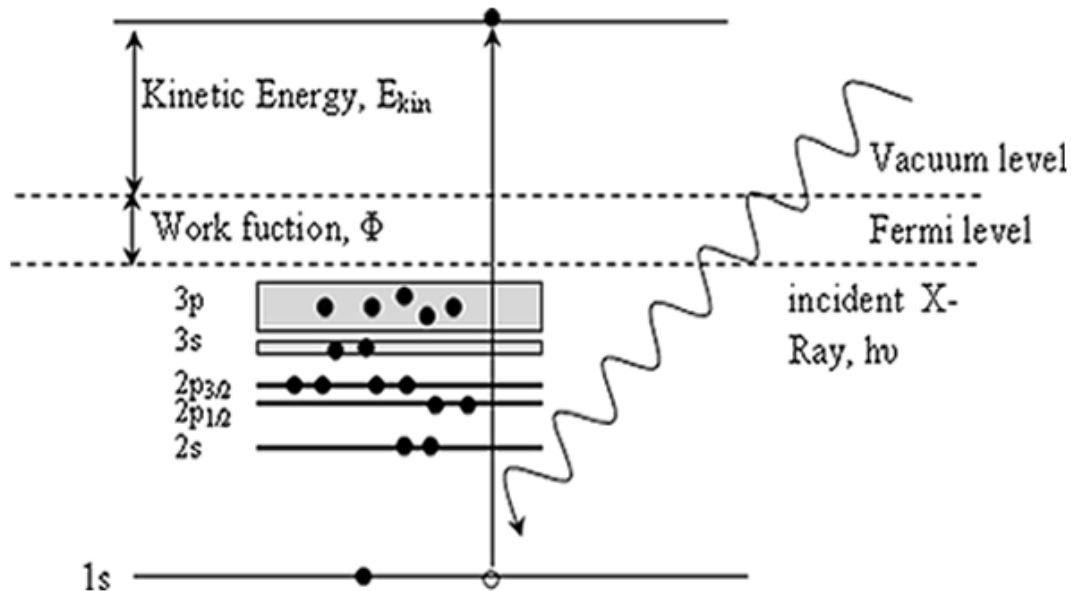


Fig. 5.1. A representative energy diagram of the photoemission process in XPS

Both the determination of atomic percentage and chemical environment require a successive quantification study (i.e. background subtraction and peak fitting). Shirley [4] and Tougaard [5] developed two methods that are widely used for

background subtraction (Fig. 5.2). While the electron energy linewidth in the core shell is defined with a Lorentzian curve that of generated by X-ray is defined with a Gaussian curve. Hence the measured peaks should be deconvoluted in terms of a combination of both algorithm which is called as Voigt. In Fig 5.3, O 1s peak was deconvoluted by using Lorentzian, Gaussian and a combination of both approach are given. In the studies given in this thesis were performed using a software, XPSPEAK95 [6].

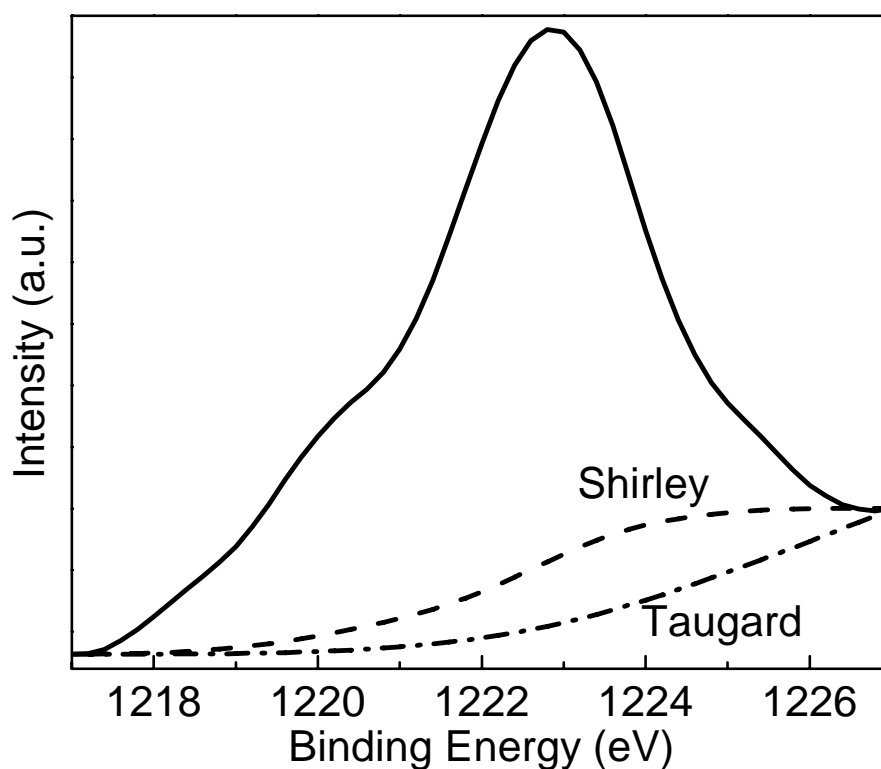


Fig. 5.2. Background correction for Ge 2p peak by using Tougaard and Shirley method

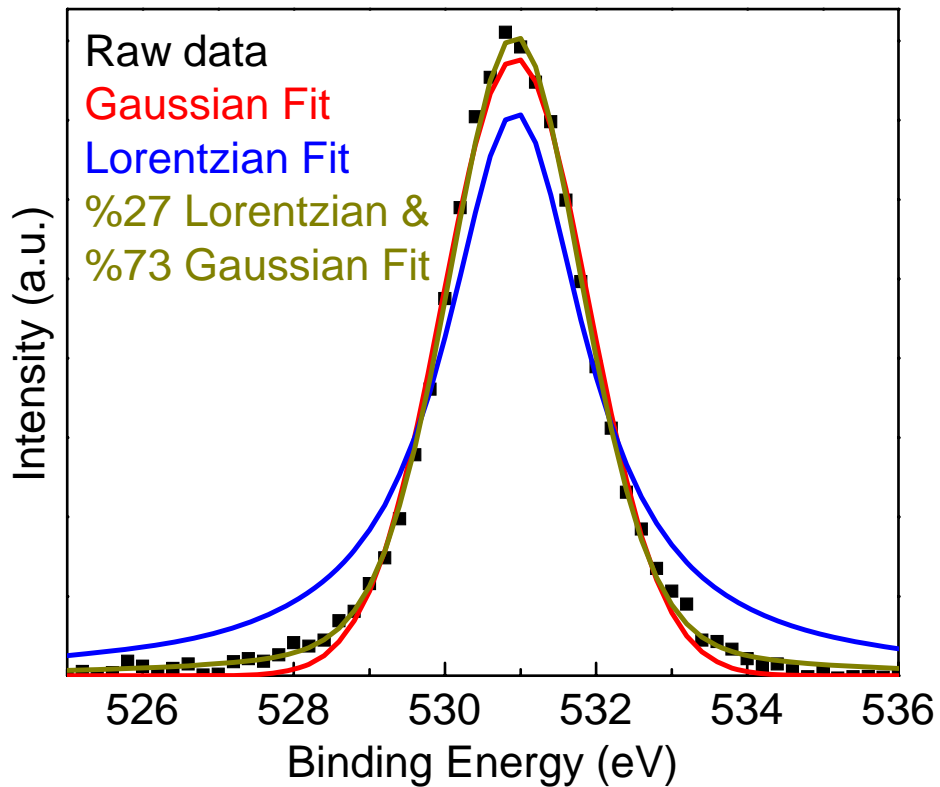


Fig. 5.3. Deconvolution of O 1s peak with a Gaussian, a Lorentzian and a combined (Gaussian + Lorentzian) fit

There are some other electron emissions when X-Ray is introduced to a sample. These emissions can be misinterpreted such as Auger lines, X-ray satellites, X-ray ghosts, shake-up lines, multiplet splitting, plasmon lines, and valance band lines. Auger lines are generated during the photoemission process where empty valence band is filled with an electron from an upper band and another electron in the upper shell gain a kinetic energy to reach the detector. Moreover, satellites resulted from a photoemission occurs not due to  $K_{\alpha 1,2}$  line of incident X-ray but other lines such as  $K_{\alpha 3}$ ,  $K_{\alpha 4}$ , etc. Excitation with Mg impurity on Al anode or vice versa can lead to X-

ray ghosts in the spectrum become visible. Extraction of an electron located in an excited state rather than ground state causes the shake-up lines. On the other hand, static charging on insulators can cause a shift in the spectrum which may mislead the researchers [7].

In XPS investigations, relative concentrations of the elements are commonly calculated. For this calculation, the integrated area of the peak (photoelectrons per second),  $I$ , and atomic sensitivity factor (ASF),  $S$ , should be known. If these are known, one can calculate the relative concentrations,  $c$ , as follows [7]

$$\frac{c_1}{c_2} = \frac{I_1/S_1}{I_2/S_2} \quad (5.2)$$

Integrated area of the peaks can be found by applying successive fitting procedure. ASF is an instrument dependent parameter and can be expressed as

$$S = \Theta y \lambda A T f \sigma \quad (5.3)$$

In this formula;

$f$  is the X-ray flux,

$\sigma$  is the photoelectric cross section for the atomic orbital of interest,

$\Theta$  is the angular efficiency factor for the instrumental arrangement based on the angle between the photon path and detected electron,

$y$  is the efficiency in the photoelectric process for formation of photoelectrons of the normal photoelectron efficiency,

$\lambda$  is the mean free path of the photoelectrons in the sample,

$A$  is the area of the sample from which photoelectrons are detected,

$T$  is the detection efficiency for the electron emitted from the sample.

ASF values, which are given in various reference books [7, 8], can be applied only in the measured instrument and therefore, it should be calibrated for elements in

various setups. In this work, ASF values of the elements Si, O and Al were calibrated only.

In principle, a quantitative calculation is possible using XPS. By assuming a homogenous sample in the analysis, the concentration of a specific spectral peak can be found as [7]

$$c = \frac{I}{f\sigma\Theta y\lambda AT} \quad (5.4)$$

However, calculation of measurement of exact ASF value is very difficult. Therefore relative concentrations of the elements are frequently calculated.

Decrease in the dimensions of the devices enhances the importance of the interface due to the increase in the ratio of the interface atoms to the bulk atoms. XPS, as a most widely used method for surface analysis, is very important to analyze the interface states of the nanostructures. XPS is widely employed in nanostructure analysis not only to show the chemical states of the interface but also to investigate the depth distribution of elements and their chemical states and to characterize physical-chemical properties of these structures.

Depth profiling by successive sputtering is widely employed in XPS measurements. Although sputtering used to remove the material from the surface creates some artifacts on the surface such as atomic mixing, knock on implantation, bond breaking and preferential sputtering, reliable depth profiling can be obtained with this technique. Use of low energy ions and ion species with higher masses (i.e. Xe, Kr) can minimize some of these artifacts [9]. XPS can also be used in the analysis of very thin films such as ultra thin oxides where the ratio of  $\text{Si}^{4+}$  (photoelectron from Si in  $\text{SiO}_2$ ) to  $\text{Si}^0$  (photoelectron from Si in bulk Si) states can be used [10, 11]. Angle Resolved XPS improves even further the method in surface applications [12].

Recently, Yang et. al. have published an interesting study on XPS analysis of nanocrystals [13]. Assuming that a nanocrystal has a spherical core with a radius  $r$

and surrounded by a spherical shell with a thickness  $d$ , the photoelectron intensity  $I$  of the core can be expressed as [14],

$$I(\lambda, d, r) = \frac{\kappa(r/\lambda)d + \lambda}{d + \lambda} e^{-d/\lambda} \pi \lambda^3 \left\{ (r/\lambda)^2 + [(2r/\lambda + 1)e^{-2r/\lambda} - 1]/2 \right\}, \quad (5.5)$$

with

$$\kappa(\rho) = \frac{\beta_1 \rho^2 + \beta_2 \rho + 1}{\beta_1 \rho^2 + \beta_3 \rho + 1}, \quad (5.6)$$

where  $\rho=r/\lambda$ ,  $\beta_1$ ,  $\beta_2$  and  $\beta_3$  are fitting constants,  $\lambda$  is the effective attenuation length in the core shell nanocrystal and is  $\sim 3.5$  nm for  $\text{SiO}_2$  and  $\sim 3.0$  nm for Si.

The relative  $\text{SiO}_x$  concentration of the oxidized shell can be computed from Eqn. 5.5, as

$$C_{\text{Si-O}} = \frac{I_{\text{Shell}}}{I_{\text{shell}} + \mu I_{\text{Core}}}, \quad (5.7)$$

where  $I_{\text{Core}}=I(\lambda_{\text{Si}}, d, r)$  and  $I_{\text{Shell}}=I(\lambda_{\text{Si-O}}, d=0, r+d)-I(\lambda_{\text{Si-O}}, d, r)$  are the core and shell intensities, respectively.  $\mu$  is the ratio of the densities of Si ( $\sim 4.96 \times 10^{22} \text{ cm}^{-3}$ ) and  $\text{SiO}_2$  ( $\sim 2.27 \times 10^{22} \text{ cm}^{-3}$ ).

Using the conservation of the number of Si atoms during the oxidation, the following relation can be obtained between the shell thickness  $d$  and core radius  $r$ .

$$d_1^3 + 3r_1 d_1 - \mu(1 - r_1^3) = 0, \quad (5.8)$$

where  $d_1=d/r_0$  and  $r_1=r/r_0$  are the  $d$  and  $r$  normalized with respect to the initial core radius,  $r_0=2.5$  nm. This equation can be solved for  $d$  and  $r$  by using equation 5.5.

In another study, Chen et. al. has reported interesting results on the investigation of Si nanocrystals using XPS. They measured a decrease in the binding energy of the core electrons of nanocrystalline Si with respect to crystalline Si [15]. Similar results were also reported and shown to be in agreement with theoretical expectations [16-18].

## 5.2 Instrumentation

XPS requires UHV condition mainly due to two reasons; to maintain the surface from the contamination and to increase the mean free path of emitted electrons. XPS is a highly surface sensitive method and susceptible to surface contamination. According to gas kinetic theory, base pressure should be  $10^{-8}$  mbar or less to keep the surface clean enough for a surface analytical measurement without having a contamination from the gas phase interface [2]. Moreover, UHV is necessary to enlarge the mean free path of the electrons which is defined as the average distance traveled by the electrons before a collision takes place.

XPS setups primarily are composed of X-ray source, electron analyzer and electron detector, however, ion gun for depth profiling is commonly included as well. A representative XPS setup is given in Fig. 5.4.

*X-ray sources:* Chemical analysis of XPS spectrum needs an energy resolution less than 1 eV. Furthermore, the linewidth of an electron in a core level is very small. Therefore, the linewidth of the X-ray is principle consideration for choosing a material as an X-ray source in XPS measurement. On the other hand, the candidate material should allow an easy production of X-ray with electron collisions, therefore, should be a conductor to enable the rapid removal of the heat transpires during the electron collisions. It should be an UHV compatible material as well. Mg and Al are two materials which are most suitable for this operation.  $K\alpha$  lines of both materials are universally used with their energies of 1253.6 eV for Mg and 1486.6 eV for Al. Principle  $K\alpha$  lines of both materials are unresolved doublet and labeled as  $K\alpha_{1,2}$ . In addition to these lines, there exists a series of subsequent lines, called as satellite lines and appear in the spectrum 8-12 eV for  $K\alpha_{3,4}$  at the lower binding energy side. These satellite lines, separation of  $K\alpha_{1,2}$  doublet and elimination of the Bremsstrahlung background can be achieved by monochromatization.

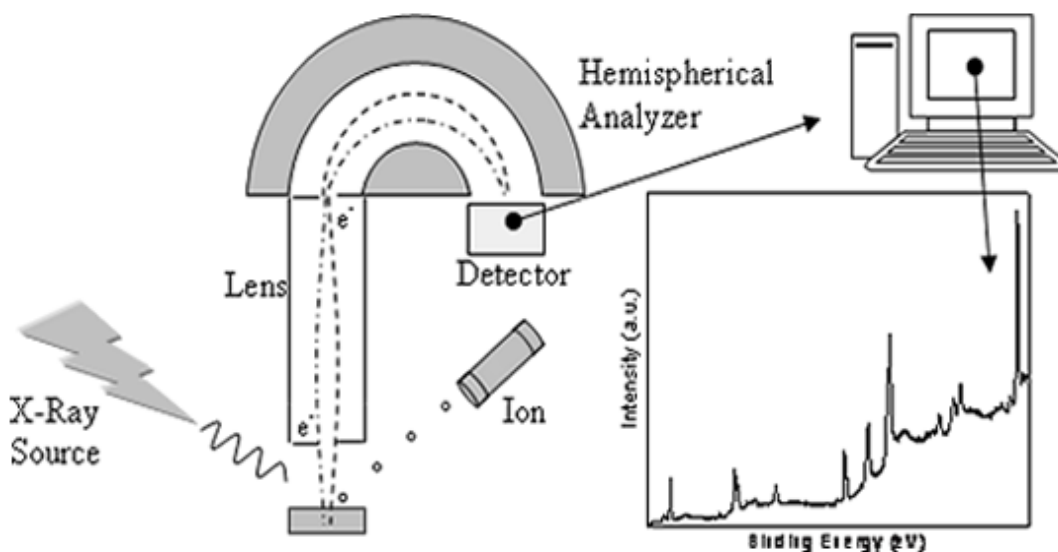


Fig. 5.4. Representative diagram for XPS measurement setup

*Electron Analyzer:* Deflection-type analyzers, aiming to separate the electrons such that only electrons with a desired energy move along the specific trajectory through the detector, are used in XPS measurement. There are various possible geometries for analyzers such as cylindrical mirror analyzer,  $127^\circ$ -angle analyzer and concentric hemispherical analyzer. Among these CHA, employed universally, have two concentric metal hemispheres. Different voltages are placed on each hemisphere such that there is an electric field between the two hemispheres. Electrons are injected into the gap between the hemispheres. If the electrons are traveling very fast, they will impinge on the outer hemisphere. If they are traveling very slowly, they will be attracted to the inner hemisphere. Hence only electrons in a narrow energy region (called the pass energy) succeed in getting all the way round the hemispheres to the detector.

*Ion gun:* Energetic ions from the ion gun launch to the surface of the sample for XPS analysis. Several monolayers are removed by the collisions for either etching the surface contamination or depth profiling. Inert gas ions (widely Ar) are created by collisions with electrons and conducted for sputtering. The positive ions are accelerated to between 0.5-10 keV and focus on the sample to create a successive etching for depth analysis.

In this thesis, XPS measurements were done with a Specs Lab XPS system, situated in the Central Laboratory at METU, equipped with a hemispherical electron analyzer operated with a focusing lens at a spot size of 750  $\mu\text{m}$  and at a take-off angle of 90 °C. Mg  $K_{\alpha}$  line with a power of 200 W was used as the excitation source. 3500 eV energetic  $\text{Ar}^+$  ions were accelerated onto the sample with an angle of 45 ° for sputtering during the depth profiling. An area of 3x3 mm was etched out with  $\text{Ar}^+$  sputtering and the ejected electrons were collected from the center of the sputtered area to avoid the edge effect. Data analysis techniques (background correction, peak fit and linear least square methods) were applied to improve the data evaluation using XPSPEAK95 software [6]. Moreover, SIMS depth profile was measured with Cameca 4-f instrument. A  $\text{Cs}^+$  primary beam with an impact energy of 3 keV was used. The  $^{147}\text{CsN}^+$ ,  $^{161}\text{CsSi}^+$ ,  $^{149}\text{CsO}^+$  and  $^{160}\text{CsAl}^+$  secondary ion species were monitored in order to reduce the matrix effects. Samples were deposited with gold to decrease static charging generated during the sputtering with positive charged  $\text{Cs}^+$  ions. Depths of the craters produced during the sputtering process were measured using a surface profilometer Tendor.

### 5.3 Probing Nanostructures with XPS

#### 5.3.1 Si Nanocrystals Formed into Al<sub>2</sub>O<sub>3</sub> by Ion Implantation

C-plane oriented  $\alpha$ -Al<sub>2</sub>O<sub>3</sub> substrates were implanted with 100-keV <sup>28</sup>Si<sup>+</sup> ions at nominal doses of  $2 \times 10^{17}$ ,  $1 \times 10^{17}$  and  $2 \times 10^{17}$  Si/cm<sup>2</sup>, and annealed at 1000°C in N<sub>2</sub> ambient for 2 h to induce Si nanocrystal formation. These nominal dose values were found from the integration of the current supplied to the sample from the ground and may not reflect the exact values. A Si substrate was placed next to the sapphire sample during the implantation process to decrease the charging effect for samples A31 and A 69 which have the same nominal doses with A44 and A94. The projected range (Rp) of the Si ions was calculated as 81 nm using TRIM software. However, Fig. 5.5 shows that the projected range increases with the implantation dose. The projected ranges for various samples were found by measuring the depth of the craters produced during the SIMS measurement using a surface profilometer. The same method was applied to rescale the x axis from sputtering time to the depth of the samples.

Exact concentrations of the samples cannot be calculated due to the lack of a standard sample. The sample with the lowest concentration was assumed to have a dose of  $2 \times 10^{16}$  Si/cm<sup>2</sup>. The respective projected ranges and the doses obtained from the counter of implanter and SIMS measurements of the samples are given in Table 5.1.

As it can be understood from Table 5.1, the measured projection ranges are significantly higher than the predicted ones using TRIM calculations. Similar phenomenon was observed using TEM and EDS measurements for the Ge ions implanted into the Al<sub>2</sub>O<sub>3</sub>. One can say that the projected range increases with the dose. Therefore, the difference between calculated and experimental values can be attributed to the modification of the sapphire matrix and the formation of Si rich layer during the implantation. A more precise calculation by taking structural

variations during the implantation into account is needed to remove these discrepancies.

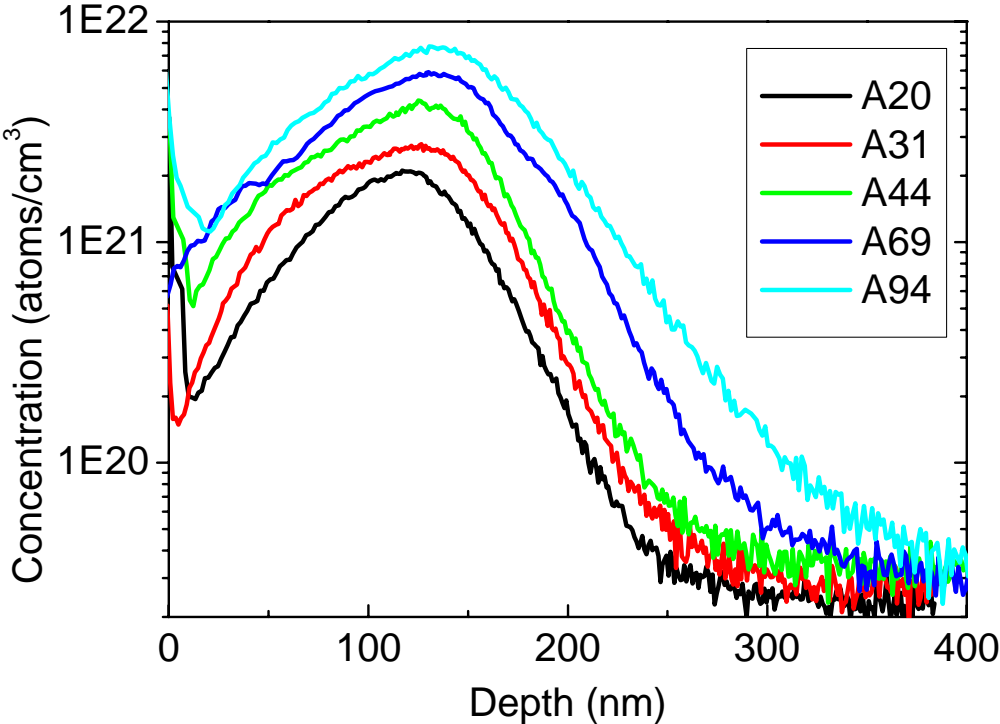


Fig. 5.5. SIMS depth profile of the samples prepared by ion implantation with different doses

Table 5.1. The doses and the respective projected ranges of the samples produced by ion implantation into Al<sub>2</sub>O<sub>3</sub>

Sample Name	Nominal Dose (Si/cm <sup>2</sup> )	SIMS Dose (Si/cm <sup>2</sup> )	Projected Range (nm)
A20	2x10 <sup>16</sup>	2 ±0.4x10 <sup>16</sup>	121.0
A31	1x10 <sup>17</sup>	3.1±0.6 x10 <sup>16</sup>	126.6
A44	1x10 <sup>17</sup>	4.4± 0.9x10 <sup>16</sup>	125.1
A69	2x10 <sup>17</sup>	6.9± x1.310 <sup>16</sup>	130.3
A94	2x10 <sup>17</sup>	9.4 ±x1.910 <sup>16</sup>	130.6

SIMS analysis of ions of bulk Silicon such as Si<sub>2</sub><sup>+</sup>, Si<sub>3</sub><sup>+</sup>, Si<sub>4</sub><sup>+</sup>, and Silicon Oxides like SiO<sub>3</sub><sup>+</sup>, SiO<sub>2</sub><sup>+</sup>, SiO<sup>+</sup> were also studied in annealed samples to have an indication about the nanocrystals formation and the environment of the nanocrystals, respectively [19]. However, the signals were too weak to make a reasonable analysis.

Another depth profile measurement for the samples implanted with a dose of 2x10<sup>17</sup> Si/cm<sup>2</sup> and annealed at 1000 °C was employed using XPS. Si 2p, O 1s, Al 2p and C 1s signals were detected after each Ar sputtering. C 1s signal was related with surface contamination and completely disappeared after four etching steps. Lack of C 1s signal during the depth profile measurements hinder the possibility of static charge correction which is usually obtained from the shifts in the position of this peak from its expected position (~285 eV).

XPS depth profiles of the sample implanted with  $2 \times 10^{17}$  Si/cm<sup>2</sup> for O 1s signal is given in Fig. 5.6. When it is compared with the depth profile of Si 2p signal shown in Fig. 5.7 one can see that O concentration decreases with increasing Si concentration. Formation of a Si rich layer is also expected. Si 2p signal observed in first five sputter is mainly due to a combination with noise and error occurred during the background elimination.

Fig 5.8 and 5.9 show the depth distributions of O 1 s and Si 2p signals, respectively. Contrary to as implanted sample, Si 2p signal was observed just underneath the surface. It may be due to the diffusion of Si atoms towards the surface. A comparison between the Si 2p signals of both samples indicate that the Si 2p signals of the oxidations states decreases in annealed sample.

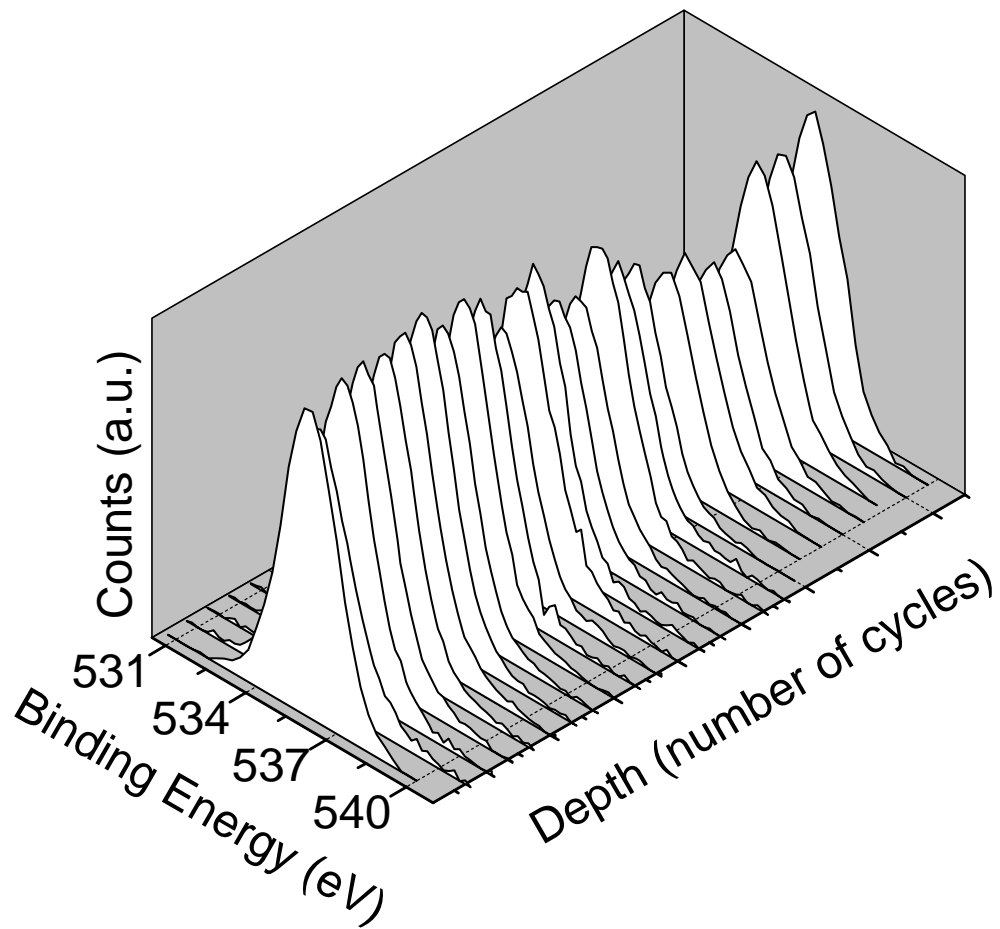


Fig. 5.6. XPS depth profile of the O 1s signals of sapphire samples implanted with a dose of  $2 \times 10^{17}$  Si/cm<sup>2</sup>

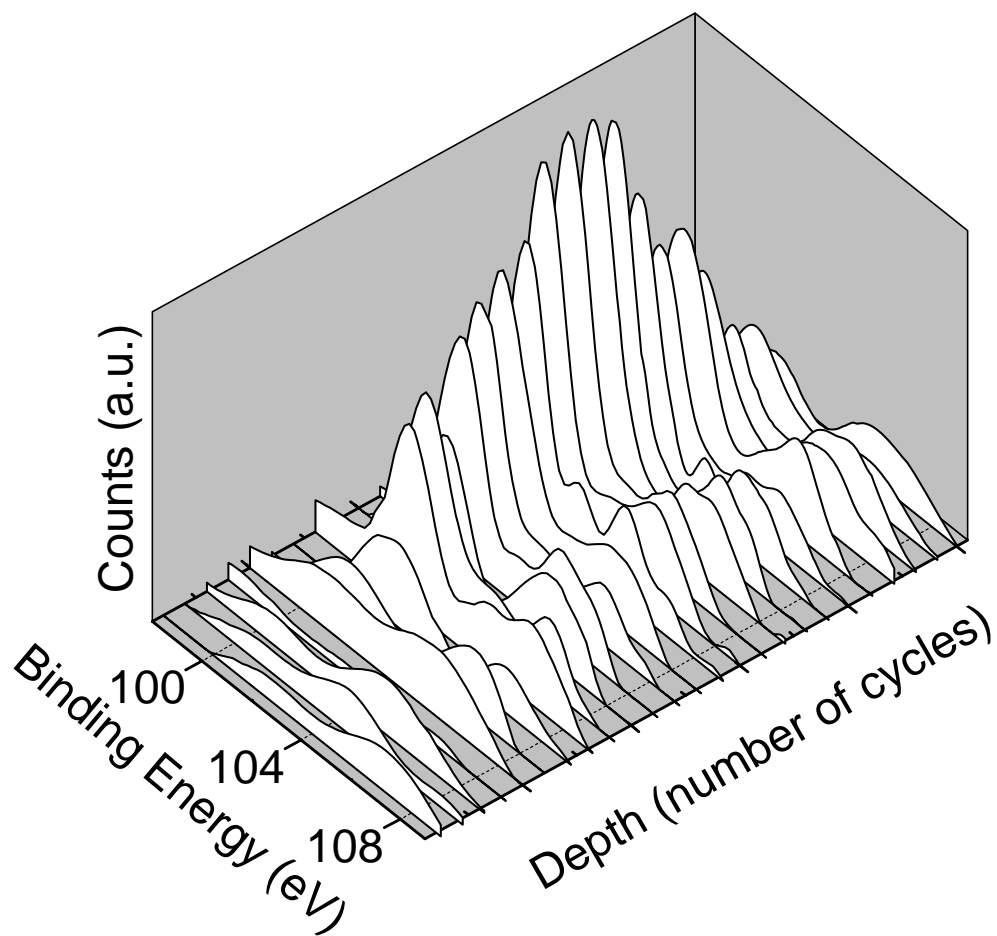


Fig. 5.7. XPS depth profile of the Si 2p signals of sapphire samples implanted with a dose of  $2 \times 10^{17}$  Si/cm<sup>2</sup>

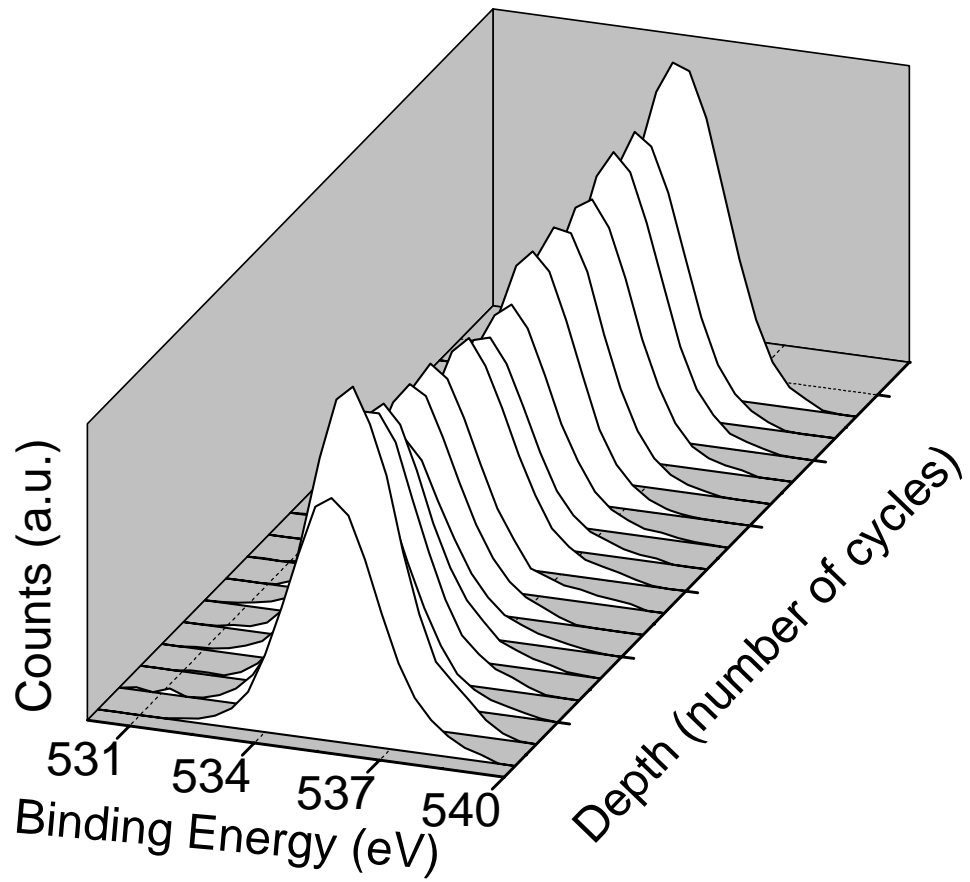


Fig. 5.8. XPS depth profile of the O 1s signals of sapphire samples implanted with a dose of  $2 \times 10^{17}$  Si/cm<sup>2</sup> and annealed at 1000 °C for 1 h under N<sub>2</sub> environment

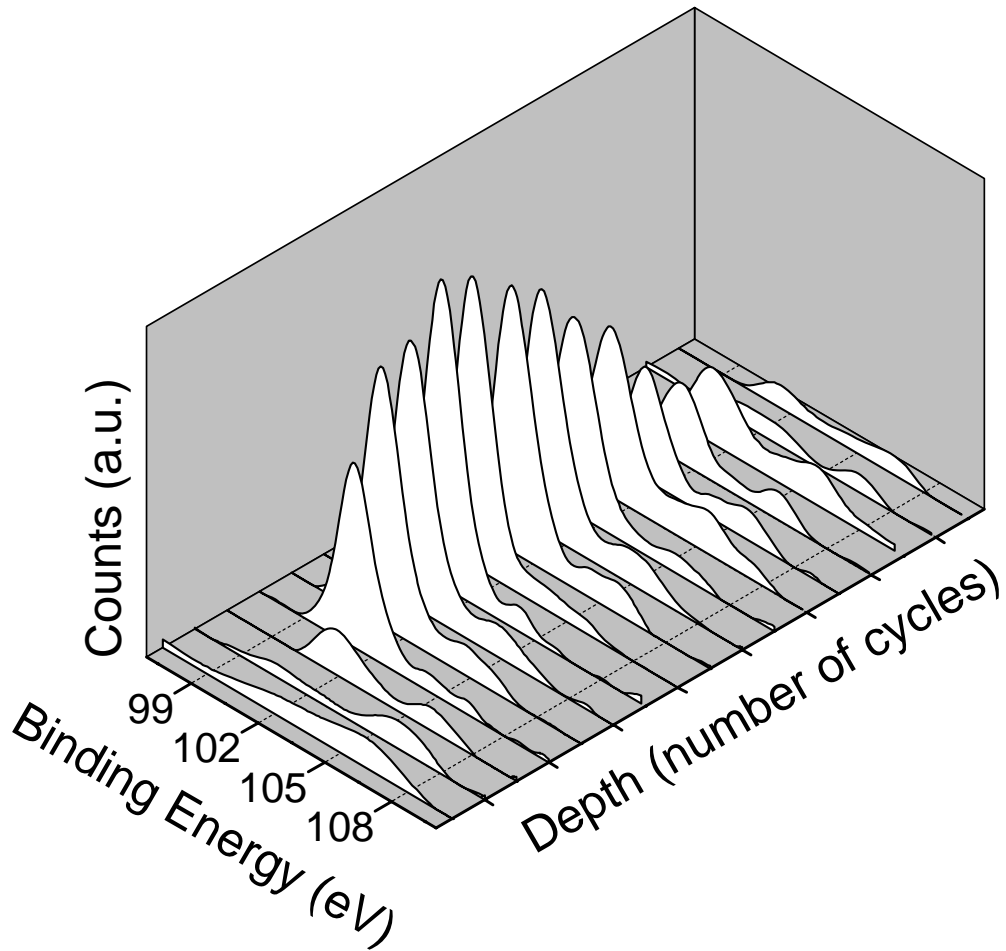


Fig. 5.9. XPS depth profile of the Si 2p signals of sapphire samples implanted with a dose of  $2 \times 10^{17}$  Si/cm<sup>2</sup> and annealed at 1000 °C for 1 h under N<sub>2</sub> environment

Fig. 5.10 shows the Si 2p XPS signals measured from the sample implanted with a dose of  $2 \times 10^{17}$  Si ions/cm<sup>2</sup>. Similar data obtained from the annealed sample are shown in Figure 1 b. Both peaks were recorded after etching the samples up to the observation of the highest Si 2p signal which is approximately located at the projected range of the implanted ions. Phase separation with annealing is clearly seen from Fig. 1. The numbers 0, 1, 2, 3, and 4 denote the oxidation states of Si<sup>n+</sup> corresponding to the chemical structures of Si, Si<sub>2</sub>O, SiO, Si<sub>2</sub>O<sub>3</sub> and SiO<sub>2</sub>,

respectively. It is evident from the comparison between Fig. 1.a and Fig. 1.b that the concentration of  $\text{Si}^0$  state increases with annealing while that of  $\text{Si}^{4+}$  state drops below the detection limits of the XPS system. This result indicates that  $\text{Si-O}_4$  bonds are not stable in  $\text{Al}_2\text{O}_3$  and dissipate to form Si nanocrystals. However, for the case of Si nanocrystals embedded in  $\text{SiO}_2$  matrix, the concentration of the both  $\text{Si}^0$  and  $\text{Si}^{4+}$  states increase due to the nucleation of the nanocrystals and recovery of the  $\text{SiO}_2$  matrix [12]. Relative concentration of  $\text{SiO}_x$  with respect to Si was calculated as 7.9% using Eqn. 5.7 which is used to find the ratio of the  $\text{SiO}_x$  shell around the nanocrystals to the core of the nanocrystals.

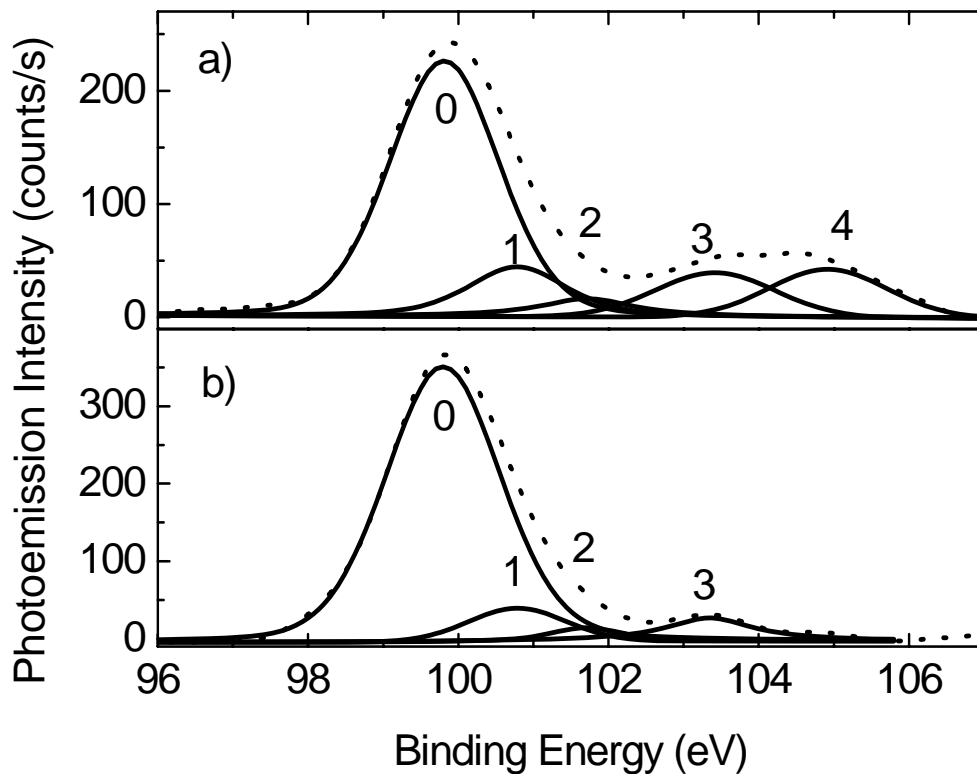


Fig. 5.10. Si 2p XPS signals for various  $\text{Si}^{n+}$  states of sample a) implanted with a dose of  $2 \times 10^{17}$  Si ions/ $\text{cm}^2$  and b) subsequently annealed at 1000 °C under  $\text{N}_2$  ambient

#### **5.4 Conclusions**

Formation of Si nanocrystals in  $\text{Al}_2\text{O}_3$  and their chemical states were studied using XPS. The increase in the  $\text{Si}^0$  XPS signal was used as an indication to the precipitation of the Si atoms, and thus formation of the nanocrystals. The volume fractions of the shell and the core of the nanocrystals was found as 7.9 % using the ratio of XPS signals due to  $\text{SiO}_x$  structure to the Si structure. Diffusion of Si atoms in  $\text{Al}_2\text{O}_3$  matrix towards the surface was proposed from the depth profile measurements.

## 5.5 References

1. C. Nordling, E. Sokolowski, and K. Siegbahn, *Phys.Rev.* 105:1676-7,1957.  
Karl Siegbahn's Nobel Lecture:  
<http://nobelprize.org/physics/laureates/1924/siegbahn-lecture.pdf> (30/01/2007).
2. *Surface and Interface analysis*, edited by H. Bubert and H. Janett (Wiley-VCH Verlag GmbH, 2002).
3. S. Hufner, *Photoelectron Spectroscopy Principles and Applications* (Springer-Verlag, Berlin 2003).
4. Shirley D. A., *Phys. Rev.*, 55, 4709, 1972.
5. Tougaard S., *Surf. Interface Anal.*, 11 453, 1988.
6. R. W. M. Kwok, ([www.phy.cuhk.edu.hk/~surface/XPSPEAK/](http://www.phy.cuhk.edu.hk/~surface/XPSPEAK/)) (30/01/2007).
7. C. D. Wagner, W. M. Riggs, L. E. Davis, J. F. Moulder, and G. E. Mulenberg, *Handbook of X-Ray Photoelectron Spectroscopy* (Pelkin-Elmer Corporation, Minnesota 1978).
8. D. Briggs and M.P. Seah (Ed.), *Practical Surface Analysis. Volume 1. Auger and X-ray Photoelectron Spectroscopy* (John Wiley and Sons, Chichester, UK 1990).
9. S. Oswald and R. Reiche, *Appl. Phys. Sci.*, 179, 307, 2001.
10. Z. H. Lu, J. P. McCaffrey, B. Brar, G. D. Wilk, R. M. Wallace, I. C. Feldman, and S. P. Tay, *Appl. Phys. Lett.* 71, 2764, 1997.
11. S. Oswald, R. Reiche, M. Zier, S. Baunack, and K. Wetzig, *Appl. Sur. Sci.*, 252, 3, 2005.
12. Y. Lui, T. P. Chen, Y. Q. Fu, M. S. Tse, J. H. Hsieh, P. F. Ho, and YY. C. Liu, *J. Phys. D: Appl. Phys.* 36 L97, 2003.
13. D. Q. Yang, J. N. Gillet, M. Meunier, and E. Sacher, *J. Appl. Phys.* 97, 024303, 2005.
14. J. N. Gillet and M Meunier, *J. Phys. Chem. B*, 109, 8733, 2005.
15. T. P. Chen, Y. Lui, C. Q. Sun, M. S. Tse, J. H. Hsieh, Y. Q. Fu, Y. C. Lin, and S. Fund, *J. Phys. Chem. B*, 108, 16609, 2004.

16. A. Dane, U. K. Demirok, A. Aydinli, and S. Suzer, *J. Phys. Chem. B*, 110, 1137, 2006.
17. T. Ohgi and D. Fujita, *Phys. Rev. B*, 66, 115410, 2002.
18. Q. C. Sun, B. K. Tay, Y. Q. Fu, S. Li, T. P. Chen, H. L. Bai, and E. Y. Jiang, *J. Phys. Chem. B*, 107, 411, 2003.
19. M. Perego, S. Ferrari, M. Fanciulla, G. B. Assayag, C. Bonafas, M. Carrada, and A. Claverie, *Appl. Sur. Sci.*, 231-232, 813, 2004.

## CHAPTER 6

### CONCLUSIONS AND FUTURE STUDIES

In this thesis, application of various diagnostic techniques to characterization of semiconductor nanocrystals has been investigated. Most popular and powerful analytical techniques, FTIR, Raman Spectroscopy, XRD, XPS and SIMS have been employed for this detailed investigation. It is believed that new achievements have been obtained in the field of nanocrystal research as well as nanometrology. These achievements are summarized below.

FTIR spectroscopy was employed to study the matrix changes during the formation of Si and Ge nanocrystals. Recovery of the SiO<sub>2</sub> matrix with the annealing was observed. Moreover, another peak, deconvoluted from the asymmetric stretching bond of Si-O-Si, shifts to lower wavenumber while its intensity decreases. This peak was used as an evidence for the Si nanocrystals formation.

Raman spectroscopy is a relatively easy and non-destructive technique and very powerful in the characterization of nanocrystals. It provided information about the size and the amorphous to crystalline ratio in a mixed system. The temperature and the stress on the nanocrystals can also be studied with Raman spectroscopy. In this study, huge compressive stress was estimated in the samples implanted Si and annealed at high temperatures. Moreover, the amorphous to crystalline ratio of Si

nanocrystals was calculated as a function of temperature. Bimodal size distribution of the Ge nanocrystals formed in  $\text{Al}_2\text{O}_3$  was proposed from the Raman spectra.

XRD was used to show the formation of nanocrystals and to calculate the average nanocrystals sizes. Although the calculation of nanocrystal size using Scherrer's formula is relatively easy it needs a careful analysis. The size of the Si and Ge nanocrystals formed into  $\text{Al}_2\text{O}_3$  and  $\text{SiO}_2$  were calculated using Scherrer's formula. A good agreement with HRTEM results was obtained for Ge nanocrystals in  $\text{Al}_2\text{O}_3$  samples

Formation of Si nanocrystals was studied using XPS by monitoring the Si 2p signals as a function of temperature. It was shown that while concentration of Si-O bonds decreases that of Si-Si bonds increases. XPS was used to find the fraction of the  $\text{SiO}_x$  shell around the nanocrystals to the core of them. It is found that the fraction decreases with the nanocrystals size.

Some of the topics given in this thesis can further be studied as follows. FTIR and XPS can be used as complementary techniques to increase the accuracy in the estimation of the volume fractions of  $\text{SiO}_x$ ,  $\text{SiO}_2$  and Si. Raman spectroscopy can also be used as a supplementary method to characterize the core properties. Electron Paramagnetic Resonance (EPR) analysis of the samples can be studied to find the volume of the unpaired electrons during the heat treatments. It can improve our understanding of origin of the photoluminescence from nanocrystals. XPS analysis of nanocrystals can be improved by employing specialized techniques such as angle resolved XPS. This approach is also useful to analyze the thin oxides which are important in MOS applications. All the methods and metrology techniques given in this work can be used in the extensive characterization of the relatively new structures such as Si and Ge nanocrystals formed in high-k dielectrics and nitrides.

## CURRICULUM VITAE

---

---

### SELÇUK YERÇİ

Nationality: Turkish Fizik Bolumu Z-29, ODTU,  
Date of Birth: 20/01/1981 06531 Ankara Turkey  
Marital Status: Single web : <http://www.metu.edu.tr/~syerci>  
e-mail: [syerci@metu.edu.tr](mailto:syerci@metu.edu.tr)  
phone: +90 312 2104314  
fax : +90 312 2105099

**EDUCATION:2004 -:** **Master of Science:** Department of Physics, Middle East Technical University (METU), Ankara, Turkey (Cum. GPA: 3.64)

**2000 -2004 : Bachelor of Science:** Department of Physics, METU, Ankara, Turkey (Cum. GPA: 3.33, “3/72” in ranking)

### EMPLOYMENT AND VISITING EXPERIENCES:

**2004 -** : Research and Teaching Assistant at the Department of Physics, METU, Ankara, Turkey

**2006 summer, Visiting Researcher:** under Prof. Dr. Jerzy Wolowski in Laser-Produced Plasma Department, Institute of Plasma Physics and Laser Microfusion, Warsaw, Poland.

**2005 summer, Visiting Researcher:** under Dr. Massimo Bersani in Physics and Chemistry of Surfaces and Interfaces Group at Center for Scientific and Technological Research, Trento, Italy.

**2002 summer, Intern:** Optics Laboratory in National Institute of Metrology, Gebze, Izmit, Turkey.

### ACADEMIC SKILLS:

**Experimental Techniques:** Fourier Transform Infrared, Raman, Optical Absorption and X-Ray Photoelectron Spectroscopy, Electro/Photo-luminescence, X-Ray Diffraction, Current-Voltage Measurement, Surface Profilometry, Scanning Electron Spectroscopy and e-beam lithography

**Computer Skills:** LabVIEW 7.1 with GPIB and DAQ, Origin Pro 7.5, Peak Fit 4.12, XPSPEAK95 4.1, SRIM 2006, Electronics Workbench 5.12 and C\C++ Programming Language (intermediate).

**Scientific Awards:** Dean’s High Honor List of Student, MRS Student Member

### EXTRACURRICULAR ACTIVITIES:

**2001- 2004** : METU Recycling Club, President.

**2002- 2004** : Outdoor Sports Club, Co-founder and Board Member of METU,

**2000- 2001** : AEGEE, Member.

**Hobbies** : Basketball, History, Documentation and Chess

### FOREIN LANGUAGES:

Fluent English and Beginner Italian

## **PUBLICATIONS:**

1. "Formation of Ge Nanocrystals in Al<sub>2</sub>O<sub>3</sub> Matrix", S. Yerci, M. Kulakci, U. Serincan, M. Shandalov, Y. Golan, R. Turan, to appear in J. Nanoscience and Nanotechnol.
2. "Formation of Silicon Nanocrystals in Sapphire Matrix by Ion Implantation and the Origin of Visible Photoluminescence", S. Yerci, I. Dogan, U. Serincan, S. Tokay, M. Genisel, A. Aydinli, R. Turan, J. Appl. Phys. 100 (2006) 074301.
3. "Implantation and Sputtering of Ge Ions into SiO<sub>2</sub> Substrates with the use of Ions Produced by Repetitive Laser Pulses" M. Rosiński, J. Badziak, A. Czarnecka, P. Gasior, P. Parys, M. Pisarek, R. Turan, J. Wołowski, S. Yerci, Materials Science in Semiconductor Processing, 9 (2006) 655-658.
4. "Evolution of SiO<sub>2</sub> Matrix during the Formation of Ge and Si Nanocrystals by Ion Implantation", U. Serincan, S. Yerci, M. Kulakci and R. Turan, Nucl. Instr. and Meth. in Phys. Res. B 239 (2005) 419–425.
5. "Structural and Optical Properties of Al<sub>2</sub>O<sub>3</sub> with Si and Ge Nanocrystals", S. Yerci, I. Yildiz, A. Seyhan, M. Kulakci, U. Serincan, M. Shandalov, Y. Golan, and R. Turan, Proc. of the MRS 2006 Fall Meeting Boston, Mater. Res. Soc. Symp. Proc., 958, L07-06, 2006.
6. "FTIR Study of SiO<sub>2</sub> Matrix Containing Si and Ge Nanocrystals Formed by Ion Implantation", S. Yerci, U. Serincan, M. Kulakci and R. Turan, Proc. of SEMINANO2005, pp. 223-226, 2005.